Terms and Conditions of Use of Digitised Theses from Trinity College Library Dublin

Copyright statement

All material supplied by Trinity College Library is protected by copyright (under the Copyright and Related Rights Act, 2000 as amended) and other relevant Intellectual Property Rights. By accessing and using a Digitised Thesis from Trinity College Library you acknowledge that all Intellectual Property Rights in any Works supplied are the sole and exclusive property of the copyright and/or other IPR holder. Specific copyright holders may not be explicitly identified. Use of materials from other sources within a thesis should not be construed as a claim over them.

A non-exclusive, non-transferable licence is hereby granted to those using or reproducing, in whole or in part, the material for valid purposes, providing the copyright owners are acknowledged using the normal conventions. Where specific permission to use material is required, this is identified and such permission must be sought from the copyright holder or agency cited.

Liability statement

By using a Digitised Thesis, I accept that Trinity College Dublin bears no legal responsibility for the accuracy, legality or comprehensiveness of materials contained within the thesis, and that Trinity College Dublin accepts no liability for indirect, consequential, or incidental, damages or losses arising from use of the thesis for whatever reason. Information located in a thesis may be subject to specific use constraints, details of which may not be explicitly described. It is the responsibility of potential and actual users to be aware of such constraints and to abide by them. By making use of material from a digitised thesis, you accept these copyright and disclaimer provisions. Where it is brought to the attention of Trinity College Library that there may be a breach of copyright or other restraint, it is the policy to withdraw or take down access to a thesis while the issue is being resolved.

Access Agreement

By using a Digitised Thesis from Trinity College Library you are bound by the following Terms & Conditions. Please read them carefully.

I have read and I understand the following statement: All material supplied via a Digitised Thesis from Trinity College Library is protected by copyright and other intellectual property rights, and duplication or sale of all or part of any of a thesis is not permitted, except that material may be duplicated by you for your research use or for educational purposes in electronic or print form providing the copyright owners are acknowledged using the normal conventions. You must obtain permission for any other use. Electronic or print copies may not be offered, whether for sale or otherwise to anyone. This copy has been supplied on the understanding that it is copyright material and that no quotation from the thesis may be published without proper acknowledgement.

Exchange Coupling in $CaMnO_3$ and $LaMnO_3$: an *ab initio* study

A thesis submitted to the University of Dublin
for the degree of Philosophiae Doctor
by

Marco Nicastro

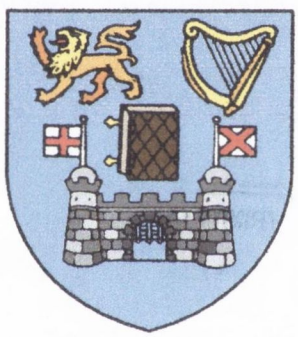

Department of Physics - Trinity College Dublin,
Dublin 2, Ireland

May 2002

Supervisor: Dr. C.H. Patterson

Declaration

This thesis is submitted to the University of Dublin by the undersigned for the degree of Doctor of Phylosophy.

This thesis has not been submitted as an exercise for a degree in any other university.

Except where otherwise stated, the work described herein has been entirely carried out by the author alone.

This thesis may be borrowed and/or copied upon request with the permission of the Library of the University of Dublin, Trinity College. The copyright belongs jointly to the University of Dublin and to Marco Nicastro.

In faith

Marco Nicastro

May 2002

Dublin

Acknowledgements

The acknowledgements section is maybe the greatest pleasure that one encounters when writing a PhD thesis. In my case I am really glad I have the opportunity to remember and thank all those who have been so important in this period of my life I've spent in Dublin.

Foremost I wish to express my deepest gratitude to Dr. Charles Patterson for having given me the opportunity to come and study in Trinity. He has been a caring supervisor, continuously helping me during this work, dedicating plenty of his time for precious suggestions and ideas, always ready to support and encourage me when I was in trouble or frustrated, and not only for problems related to my research. And thanks to his wife Walthea, too, for the warm hospitality of their house that I have enjoyed many times.

Many thanks to the members of my reserch group, whom I was very privileged to meet: Conor Hogan, for being so patient with me, especially in the beginning; Michael Kuzmin, from whose experience I learnt a lot; Svjetlana Galamić-Mulaomerović, for the help and encouragement she gave me at every stage of this work (thanks to Ernad and a kiss to Barbara as well); last but not least, Guang Zhengh and Nikolaos Konstantinidis.

I own a special acknowledgement to Geoff "System Manager" Bradley, who has done a wonderful job in keeping our computers running, always ready to rescue me when I had problems with my machine. Thanks also to Eamonn Cahill, who helped me in various circumstances involving the use of the SP2 supercomputer.

Thanks to all the people that have contributed to make G-30 (we still call it this, don't we?) a friendly and less boring working environment: Mark, Stefan, Joe, Stuart, Des, Paul, Judith, Brendan, Ferruccio, Sadikah, Sadhbh, Kate, Lola (y Victor tambien, I will miss your sangria parties!),

Adam, Gorka, Tim, Andrew, James, Finn, Gemma, Joanne (who kindly did some proof reading for me), Ian, Aran, Lorenzo, Wiebke. I hope I am not forgetting anyone!

A special mention for Simon Elliott (and Edwina) and Simon Cox (who also helped me to improve my Italian-English and corrected a part of this thesis).

Grazie mille to Stefano Sanvito, recently arrived in the department; I am grateful to him for the many suggestions he made to this work and for having passed to me some of his knowledge of good cigars. And thanks to Stefania.

Life in Dublin would not have been the same without the many friends I met; they have all been very important to me. First of all I'd like to thank Alfredo Iorio, the main person "responsible" for my coming to Trinity; he welcomed me on my arrival, guided me among the difficulties of Dublin, and has been a good friend and flatmate. Thanks also to Giuliana Adamo, Alan and Giovanna Bates.

I wish to thank the Roman Catholic chaplains of Trinity College: Paul Murphy, Aiden Larkin, Paddy Gleeson and, in a special way, Richard Sheehy, who has been a continuously caring presence and a reference point for me. Thanks to Alan McCormack and Catherine Meyer as well. A special mention is for the Folk Group, of which I had the honour to be a member: Sonia, Marie Therese, Susan, Con, Silvia, Bronagh and Michael (and their lovely twins), Helene, Shane and Gabriela, Jonh, Nick, Tara, Sharon, Kieran, Grainne... I can't name you all, but I remember everyone; I really had a good time with you during our rehersals and our retreats. And thanks to the many persons in the congregation at Sunday Mass, familiar faces and friends that made me feel at home.

Many thanks to Giulia Castellari and Elisa Aberghi, Peter Cassidy, Paul

Hare, Sophie Kerhuel, Antonella Di Trapani, John and Joan Bates, Michel and Paola Parziale, Pauline Fitzpatrick, Peter O'Brien.

I intentionally left at the end of this list of friends three persons because they deserve a special acknowledgement: Mariella Golia, Massimo De Luca and Gabriele Zenobi. They have been much more then just friends and I have been very lucky to meet them.

Of course I'd like to thank my family: Clorindo, Anna (Pupetta 1), Stefano, Maria Rosaria and Adolfo (and their new born baby Angela). Grazie a tutti voi per aver continuato ad essermi vicino e ad incoraggiarmi in questi anni. Thanks also to my wife's family: Antonio, Vita (Pupetta 2), Tania and Francesca.

Finally, I wish to ackowledge Trinity Trust, Enterprise Ireland and Dublin Corporation for funding my research activity.

This thesis is dedicated to my wife Annarita, who is the source of all my joy and happiness; she shared with me every moment of this experience in Ireland, even when she was far away.

Summary

This thesis is a study of the magnetic properties of a class of compounds known as manganites. They possess many peculiar properties which make them an interesting field of investigation for both experimentalists and theoreticians. The present work deals in particular with $CaMnO_3$ and $LaMnO_3$, end-point compounds of the series $La_xCa_{1-x}MnO_3$. The main issues addressed are the explanation of the magnetic interactions between manganese ions and the calculation of the exchange coupling constants J. The aim is to provide some of the missing information which is still needed for a complete understanding of the microscopic origin of colossal magnetoresistance in mixed-valence manganites.

A central role in this thesis is played by the existing relationship between crystal symmetry, spin and orbital ordering; it is shown that they must all be considered for an accurate description of the exchange coupling.

The study is carried out using *ab initio* methods, which allow a system to be studied starting with information only about its chemical composition and crystal structure. The Unrestricted Hartree-Fock approximation gives an adequate description of the ground state properties of $CaMnO_3$ and $LaMnO_3$; in particular, it correctly predicts their antiferromagnetic spin structure. In the case of $LaMnO_3$, it allows to study the relationship between spin, orbital ordering and crystal distortions. The Configuration Interaction approximation, which is one of the simplest methods to include the effect of electron-electron correlations in the Hamiltonian, explains the exchanghe coupling mechanism in terms of hopping of electrons between localised orbitals. The calculated exchange coupling constants are in good agreement with the ones estimated from experimental studies.

Sommario

Questa tesi è uno studio delle proprietà magnetiche di una classe di composti nota come manganati. Essi possiedono molte peculiari proprietà che li rendono un interessante terreno di investigazione sia per sperimentali che per teorici. Il presente lavoro tratta in particolare del $CaMnO_3$ e del $LaMnO_3$, composti progenitori della serie $La_xCa_{1-x}MnO_3$. Le questioni principali che vengono affrontate sono la spiegazione delle interazioni magnetiche tra ioni di manganese ed il calcolo delle costanti di accoppiamento J. Lo scopo è quello di fornire alcune delle informazioni ancora mancanti per una completa comprensione dell'origine microscopica della magnetoresistenza colossale nei manganati a valenza mista. Un ruolo centrale in questa tesi viene rivestito dalle inter-relazioni che esistono tra simmetria del cristallo, spin e ordinamento orbitale; viene mostrato che essi devono tutti essere presi in considerazione per una accurata descrizione della costante di accoppiamento.

Lo studio viene svolto usando metodi *ab initio*, i quali permettono lo studio di un sistema avendo come informazioni iniziali solo la sua composizione chimica e la sua struttura cristallina. L'approssimazione Hartree-Fock non ristretta fornisce un'adeguata descrizione delle proprietà dello stato fondamentale del $CaMnO_3$ e $LaMnO_3$; in particolare, essa predice correttamente la loro struttura di spin antiferromagnetica. Nel caso del $LaMnO_3$, permette di studiare la relazione tra spin, ordinamento orbitale e distorsioni del cristallo. L'approssimazione Configuration Interaction, che è uno dei metodi più semplici per includere gli effetti della correlazione elettrone-elettrone nell'Hamiltoniana, fornisce una spiegazione dell'accoppiamento magnetico in termini di eccitazioni di elettroni tra orbitali localizzati. Le costanti di accoppiamento così calcolate sono in buon accordo con quelle stimate da studi sperimentali.

... L'attesa e' lunga,
il mio sogno di te non e' finito.

E. Montale

Ad Annarita

Contents

Introduction

Quod super est, agere incipiam quo foedere fiat
naturae, lapis hic ut ferrum ducere possit,
quem Magneta vocant patrio de nomine Grai,
Magnetum quia sit patriis in finibus ortus.

Lucretius, *De Rerum Natura*

The discovery of the magnetic properties of matter can be dated far back in time. A few centuries before the birth of Christ travellers returning from the region of Magnesia, north of Greece, told strange stories about a magic stone that could attract iron, stories in which reality was often mixed with legend. Is this prodigious phenomenon to be ascribed to a god? Does the stone have a soul? These were the kind of questions that Greek and later Latin philosophers tried to give answer.

Since then, much progress has been made. Classic electromagnetism, brilliantly summarised in Maxwell's equations, laid the basis of the modern theory of magnetism; a complete understanding, though, has only been possible with the advent of quantum mechanics and relativity, and in particular with the discovery of the electron spin.

The manganites (general formula $T_{1-x}D_xMnO_3$, where T and D are a trivalent and a divalent cation respectively) have been known since the 1950s. At the end of the 1980s they gained greater attention from material scientists due to their enormous potential for technological applications. These mate-

rials, for particular values of x for the dopant D, show the peculiar property of a huge drop of the resistance in a magnetic field, which is termed colossal magnetoresistance and is accompanied by a paramagnetic-to-ferromagnetic transition. This characteristic makes them ideal systems for the development of a new class of magnetic devices.

The "rediscovery" of manganites gave impulse to intense studies in the last two decades. From an experimental point of view the field is well established in terms of both sample preparation and characterisation. The theory, on the other hand, is still looking for a complete explanation of the physical effects which are behind the special properties of manganites. Magnetoresistance cannot be simply explained by theories such as, for example, double exchange; its microscopic origin must be searched in the strong electron-phonon coupling, that results in effects like the Jahn-Teller distortion and the orbital ordering.

The present study takes its motivations from the need to provide some answers to the many questions which are still unsolved. One of them is the problem of exchange interactions in manganites, i.e. of the interactions that take place between the magnetic Mn ions. The aim of this thesis is to investigate the exchange coupling mechanism in $CaMnO_3$ and $LaMnO_3$, parents of the series $La_{1-x}Ca_xMnO_3$ (corresponding to $x = 1$ and $x = 0$ respectively); this is a first, necessary step toward a better comprehension of what happens at intermediate values of x, where the colossal magnetoresistance is observed. The methods used for the investigation are *ab initio* methods, which allow, in principle, to study a system without any other a priori information than its chemical composition and crystal structure. Exchange constants are calculated from total energy differences between various spin ordered structures.

The work done can essentially be divided into two parts:

1) Unrestricted Hartree-Fock study of $CaMnO_3$ and $LaMnO_3$;

2) Configuration Interaction study of clusters representing $CaMnO_3$ and $LaMnO_3$.

The Configuration Interaction method is essential for an adequate description of the exchange interactions because it provides a way of including electron correlations in the Hamiltonian. Nevertheless, in the case of $LaMnO_3$, Unrestricted Hartree-Fock calculations carried out on an idealised cubic structure give informations about the relationship between magnetic properties and orbital ordering. Exchange constants calculated in the Configuration Interaction approximation are in good agreement with the values estimated from experiments and with other theoretical studies.

The thesis is organised as follows. Chapter 1 is an introduction to the physics of manganites. After a brief review of the early experiments and theories, it outlines their general properties, with particular attention to $CaMnO_3$ and $LaMnO_3$. It also introduces the exchange coupling mechanism, and presents some of the theoretical approaches used to investigate it.

Chapter 2 contains a description of the main *ab initio* methods used in solid state physics. This include the Unrestricted Hartree-Fock (UHF) approximation, the Density Functional Theory (DFT) and Configuration Interaction (CI). Commercial packages are available in which one or more of the above methods is implemented. The Chapter includes an account of the main feature of the two packages used in the present work: CRYSTAL 98 (for UHF) and GAMESS-UK (for CI).

Chapters 3 and 4 report the results of the calculations carried out on $CaMnO_3$ and $LaMnO_3$ in the UHF and CI approximations respectively. In

Chapter 3 the role of the Jahn-Teller distortions and of orbital ordering in $LaMnO_3$ is investigated with calculations carried out on crystallographic cells of various symmetries. In Chapter 4, calculated exchange couplings are discussed in terms of the correlation energies and the relative weight of the configurations in the total wave function. Results depend on the values of an array of point charges surrounding the cluster, which is essential to reproduce the correct Madelung potential.

A last chapter contains some conclusions and an outlook for possible future work.

Finally, the Appendix gives some details about the basis sets used to describe the atomic orbitals and about the k-point grid employed in the reciprocal space integration.

The main results of this work have been published in:

M. Nicastro and C.H. Patterson, *Phys. Rev. B*, **65**, 205111 (2002).

Chapter 1

Characteristics of manganites

This chapter provides an introduction to the physical properties of manganites and a review of the main achievements, both in theory and experiment, that occurred after the discovery of their striking properties by Jonker and van Santen in the early 1950s [1, 2]. Many excellent reviews exist on the subject, treating it from different points of view [3, 4, 5, 6, 7], so what is presented here is only intended as an introduction allowing the comprehension of what will be discussed in the following chapters.

Firstly the main properties will be presented, by analysing the rich phase diagram of these compounds; then a brief history of their discovery and of the early theories proposed will be presented. $CaMnO_3$ and $LaMnO_3$, which constitute the main subject of the present work, will be presented in more detail. A final section is dedicated to the exchange coupling mechanism.

1.1 General properties

The term manganites refers to manganese compounds with the composition $T_{1-x}D_xMnO_3$, where T is a trivalent cation (e.g. La, Pr, Nd) and D a divalent cation (e.g. Ca, Ba, Sr, Pb). They crystallise as cubic perovskites

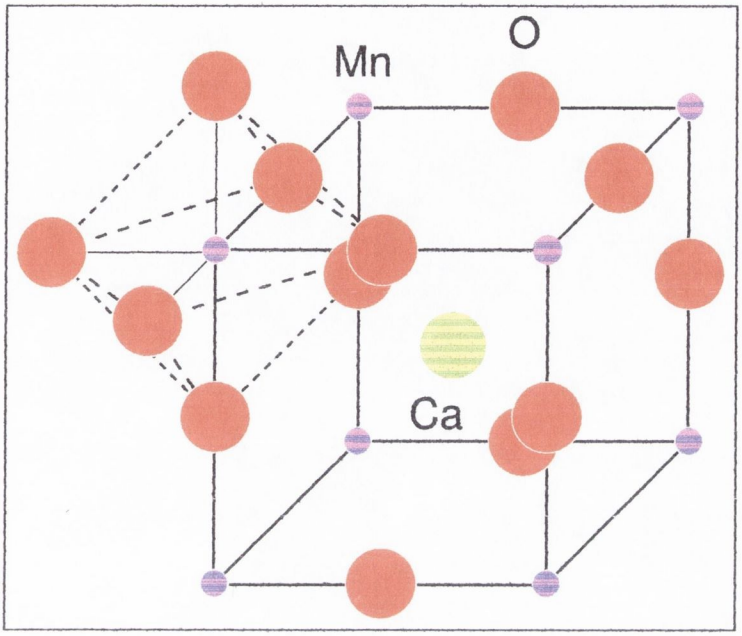

Figure 1.1: Ideal cubic perovskite structure of $CaMnO_3$.

[8], even if variations and distortions of such a structure are often present[1]. In what follows most of the attention will be on the series of manganites $La_{1-x}Ca_xMnO_3$.

The ideal cubic perovskite structure of composition ABO_3 is shown in Fig. 1.1 for $CaMnO_3$; each Mn ion is surrounded by six oxygen ions to form a regular octahedron. The stability of the perovskite structure is related to the so called Goldsmith tolerance factor f [9], a formula that relates the A and B cation radii, r_A and r_B, and the oxygen radius r_O:

$$f = \frac{r_A + r_O}{\sqrt{2}\,(r_B + r_O)} \quad . \tag{1.1}$$

The ideal radii of A and B can be calculated from eq. (1.1). The former

[1]The prototype perovskite compound, $CaTiO_3$, was discovered by Gustave Rose in 1839 from samples found in the Ural mountains; he named it after the Russian mineralogist Count Lev Aleksevic Perovskii (1792-1856).

must be the same as the oxygen radius

$$r_{\mathrm{A}} = r_{\mathrm{O}} = 1.4\mathring{A} \quad , \tag{1.2}$$

while the latter is given by

$$r_{\mathrm{B}} = r_{\mathrm{O}}\left(\sqrt{2} - 1\right) = 0.58\mathring{A} \quad . \tag{1.3}$$

This gives an f of unity for ideally sized ions; in practice it is found that the perovskite structure is stable for $0.85 < f < 1.02$.

The resurgence of the interest in manganites in the last few years is motivated by their possible use in technological applications. The reason is that, for some particular percentage x of doping, they show the phenomenon of the so-called **colossal magnetoresistance** (CMR). The magnetoresistance is a drop in resistance that accompanies the paramagnetic to ferromagnetic transition; it depends on the applied magnetic field H and can be defined, at a particular temperature, as [10]

$$\mathcal{R}(H) = \frac{\rho(0) - \rho(H)}{\rho(H)} \quad . \tag{1.4}$$

Jin *et al.* [11] first used the term "colossal" to describe the large magnetoresistance effect they observed in epitaxially grown La-Ca-Mn-O thin films. The change in resistivity, at 77 K in a field of 6 Tesla, was $\mathcal{R}(H) = 127,000\%$, was negative and was isotropic with respect to the field orientation; near room temperature the values were about 1300 % at 260 K and 400 % at 280 K. Such values were much larger than those previously observed in the so-called giant magnetoresistance (GMR) materials.

This opened a completely new opportunity for magnetic devices like magnetic field sensors, magnetoresistive read-heads, magnetoresistive microphones and so on. Magnetic systems of great potential are those with a

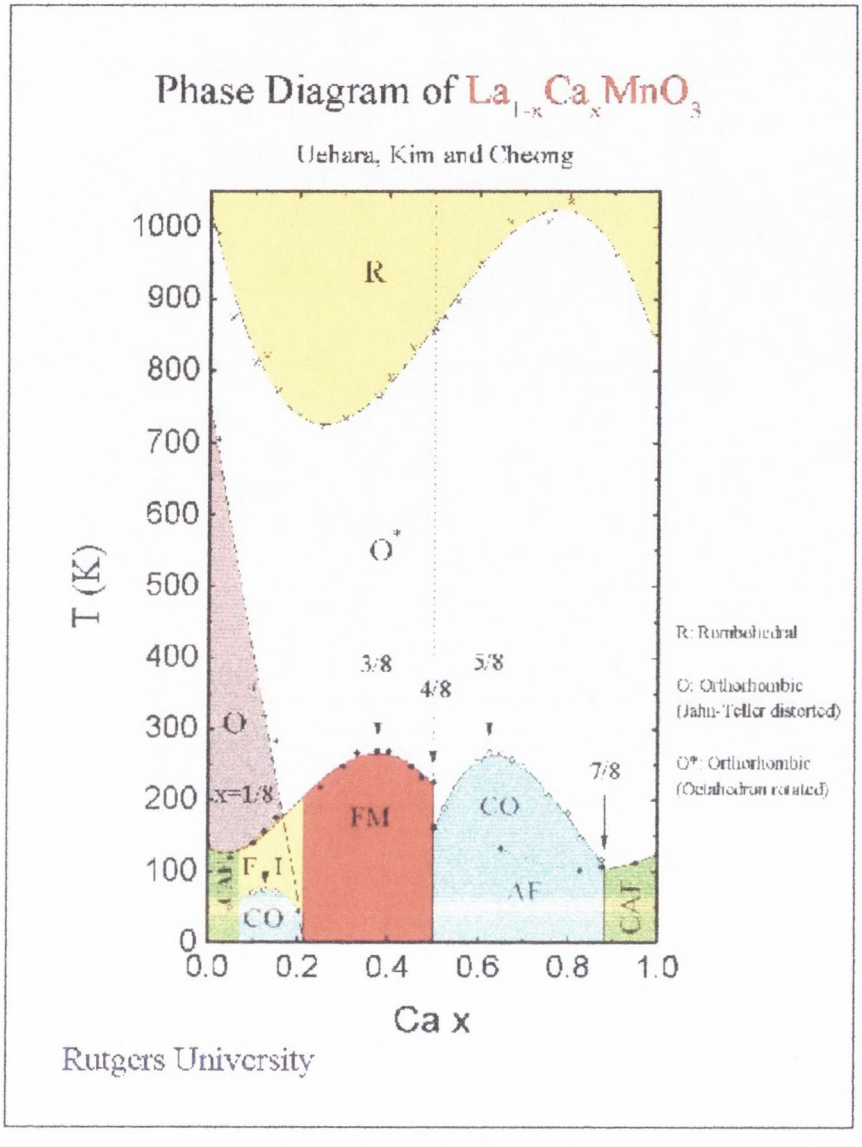

Figure 1.2: Experimental phase diagram of $La_{1-x}Ca_xMnO_3$ (from Ref. [13])

limited ability to transport electricity in zero field, resulting from two competing ground states. In this sense manganites appear as the ideal system for magnetic devices. CMR is associated with a ferromagnetic to paramagnetic phase transition, which takes place at a Curie temperature T_C around room temperature (metal-insulator transitions).

Soon after the rediscovery of manganites, theoreticians pointed out that a simple picture based on previously proposed theories could not explain the peculiar behaviour of manganites [12] and the richness of the phase diagram shown in Fig. 1.2 for $La_xCa_{1-x}MnO_3$. Here x, the Ca fraction, also indicates the percentage of Mn^{4+} ions present. The end point compounds are $LaMnO_3$ and $CaMnO_3$, corresponding to x=0 (all Mn ions are 3+, no Mn^{4+} ions are present) and x=1 (100% of Mn^{4+} ions) respectively. The part of the phase diagram of greatest interest is between $x = 0.2$ and $x = 0.5$ (in fraction x of Ca), because this is the interval where the compound is a ferromagnetic metal and shows CMR.

The particular properties of manganites derive from the close interplay of different kinds of behaviour, and in particular from the fact that they show spin, charge and orbital ordering.

Some of the possible spin orderings are shown in Fig. 1.3. The top-left one is the ferromagnetic structure (FM), the rest are antiferromagnetic (AF). In the A-type (also known as layered AF), planes of opposite spin arrangements alternate along one direction; each spin has four parallel and two anti-parallel nearest neighbours. In the C-type (or chain), spins are antiferromagnetically coupled in planes and ferromagnetically between planes; each spin has two parallel and four anti-parallel neighbours. The same neighbour coupling can also be arranged in a different way, to form the so-called E-type AF structure. Finally, the G-type (or rock salt) contains each spin surrounded by six of opposite orientation. Composite structures are also possible. Fig. 1.3 shows the CE type AF, which presents alternated C and E "units".

The main role in determining the very peculiar properties of manganites is played by the $3d$ electrons of the Mn ions. In a crystal field, the five d levels are no longer degenerate, as they are in a free atom. In a cubic environment

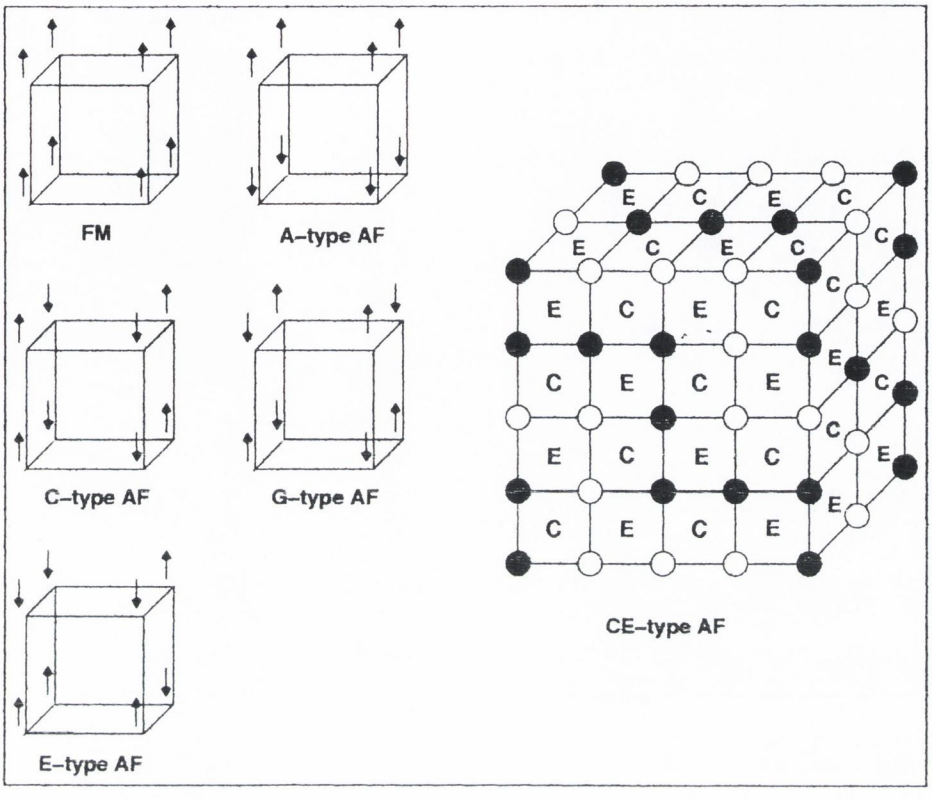

Figure 1.3: Some magnetic spin structures. In the CE structure up and down spins are represented with solid and open circles for more clarity.

such as the perovskite structure, where each Mn ion is esacoordinated with oxygen ions, they split into two sets: three form a degenerate t_{2g} set at lower energy and two an e_g set at higher energy. To understand how this happens, it is necessary to refer to the shape of the d wave functions (Fig. 1.4). The t_{2g} wave functions are d_{xy}, d_{xz} and d_{yz} and their electron density is directed in between the negatively charged ligands (oxygen ions). The e_g wave functions, on the other hand, are $d_{x^2-y^2}$ and $d_{3z^2-r^2}$ and have an electron density pointing directly toward the surrounding ligands. The latter experience a stronger Coulomb repulsion and their energy is raised. The t_{2g} - e_g splitting due to the crystal field is indicated by Δ_{CF}. When further reduction of the

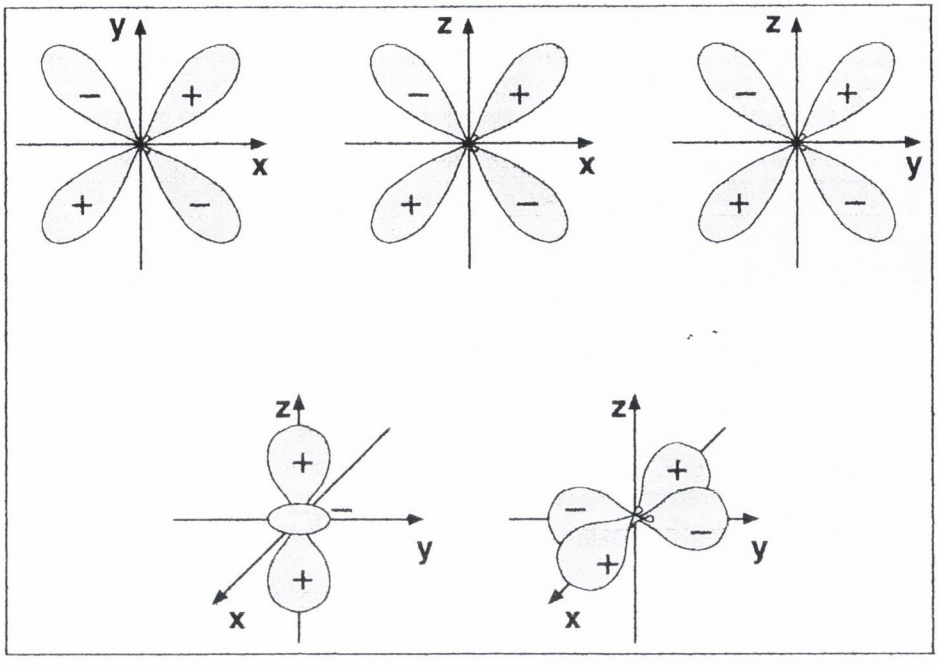

Figure 1.4: Shape of the d wave functions. Top: t_{2g} orbitals d_{xy}, d_{xz}, d_{yz}. Bottom: e_g orbitals $d_{3z^2-r^2}$ and $d_{x^2-y^2}$.

symmetry occurs, more splitting takes place, as shown schematically in Fig. 1.5.

Charge ordering is the name given to an ordered pattern of Mn^{3+} and Mn^{4+} ions. In fact in $La_xCa_{1-x}MnO_3$ the e_g charge distribution is not uniform: a fraction $1-x$ of Mn ions (Mn^{3+}) has an e_g electron and a fraction x (Mn^{4+}) has no e_g electron. At particular temperatures and concentrations a periodic pattern of filled and empty e_g sites is formed, and this is called charge ordering. Its first, clear evidence was found in $La_xCa_{1-x}MnO_3$ by Chen and Cheong [14] in 1996; their electron-diffraction images clearly showed superlattice peaks consistent with alternation of Mn^{3+} and Mn^{4+} charges.

Similarly, **orbital ordering** for Mn^{3+} ions arises if a periodic pattern of orbital occupancies appears. The filling of d levels follows Hund's rule: in order to minimise Coulomb repulsion, electrons are accommodated in such

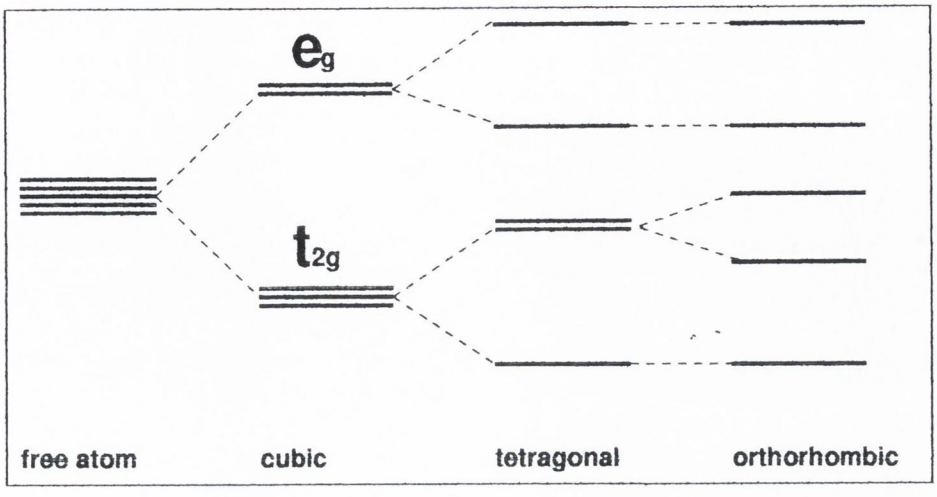

Figure 1.5: Sketch of the splitting occurring in the five degenerate d levels when a free atom is placed in a crystal field. The t_{2g} - e_g splitting in a cubic (octahedral) environment and further splitting following a reduction of symmetry to tetragonal or to orthorhombic are shown.

a way to form a state with maximum possible spin. This means that in Mn^{4+} (d^3) ions the three d electrons will occupy the lowest energy t_{2g} states with a total spin of 3/2, while the four d electrons in Mn^{3+} (d^4) ions will occupy the three t_{2g} plus one of the e_g states to give a total spin of 2. The Hund's rule coupling energy J_H is normally about 2-3 eV in manganites and is larger, for example, than the inter-site hopping interaction of an e_g electron between neighbouring sites. In general the occupied e_g orbital will be a linear combination of the two types of orbitals described above. In Fig. 1.7 it is possible to see how occupied e_g orbitals on Mn^{3+} ions form a regular pattern of alternating orientations in the plane.

The microscopic origin of orbital ordering is in the Jahn-Teller (JT) effect [15, 16] that characterises d^4 ions in an octahedral environment; it is a consequence of a very general and powerful theorem in quantum mechanics known as the Jahn-Teller theorem, which was published in 1937 [15] and states:

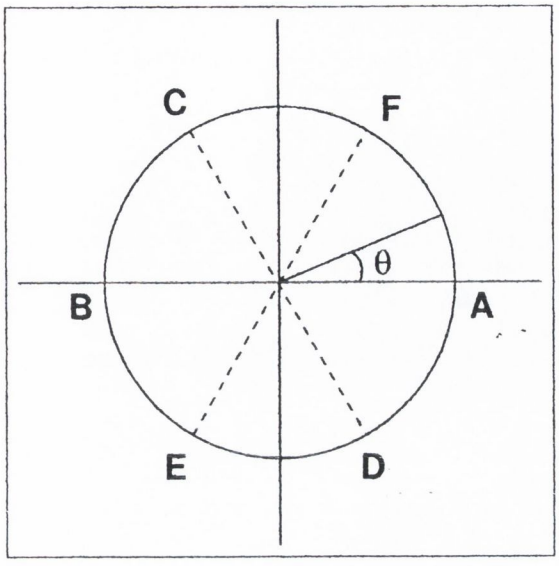

Figure 1.6: The θ-plane for the visualisation of all possible e_g states. A few points are shown as examples: A ($\theta = 0$) is $d_{3z^2-r^2}$; B ($\theta = \pi$) is $d_{x^2-y^2}$; C ($\theta = \frac{2}{3}\pi$) is $d_{3x^2-r^2}$; D ($\theta = -\frac{1}{3}\pi$) is $d_{z^2-y^2}$; E ($\theta = -\frac{2}{3}\pi$) is $d_{3y^2-r^2}$; F ($\theta = \frac{1}{3}\pi$) is $d_{z^2-x^2}$. From ref. [17].

> *Any non-linear molecular system in a degenerate electronic state will be unstable and will undergo a distortion to form a system of lower symmetry and lower energy thereby removing the degeneracy.*

The degenerate electronic state in this case is the set of linear combinations of the two e_g orbitals; as a consequence, the crystal will distort, the symmetry will lower and one of the two e_g orbitals will be favoured, with a consequent removal of the degeneracy. For example a local elongation along the z axis stabilises the $d_{3z^2-r^2}$ orbital, whereas a local contraction along the same axis favours $d_{x^2-y^2}$ stabilisation. As the problem is one of double orbital degeneracy, it is convenient to describe the orbital structure in the same way as with a spin 1/2 system, i.e. with a pseudospin operator. The basis chosen is formed by the two eigenstates: $|d_{3z^2-r^2}>$, corresponding to the eigenvalue

1/2, and $|d_{x^2-y^2}>$, corresponding to the eigenvalue -1/2. Then a general linear combination of such states can be written as

$$|\text{occ}>= \cos\frac{\theta}{2}|d_{3z^2-r^2}> + \sin\frac{\theta}{2}|d_{x^2-y^2}> \quad . \tag{1.5}$$

From this formula $d_{3z^2-r^2}$ and $d_{x^2-y^2}$ are obtained for $\theta = 0$ and $\theta = \pi$. Nevertheless, directions x, y and z are equivalent and, in a sense, arbitrary. So not only an orbital $d_{3z^2-r^2}$ extended along z can be formed, but also a $d_{3x^2-r^2}$ along x or a $d_{3y^2-r^2}$ along y. They correspond to some particular rotation of axes in space. A useful tool that helps visualise such a rotation is the θ-plane [17], where points represent particular orientations of orbitals in space. In Fig. 1.6 [17] some example of points in the θ-plane are shown.

A schematic picture of spin, charge and orbital ordering is shown in Fig. 1.7 for $La_{1/2}Ca_{1/2}MnO_3$.

1.2 Early experiments and theories

The history of the study of manganites is more than 50 years old. It began in 1950 with the first experimental work by Jonker and van Santen [1, 2] who studied samples of $La_{1-x}A'_xMnO_3$, where A' was one of the divalent cations Ca^{2+}, Sr^{2+} and Ba^{2+}. They found a surprising correlation between the Curie temperature T_C, the conductivity σ and the saturation magnetization M_S. In particular in polycrystalline samples of $La_{1-x}Sr_xMnO_3$ they observed that, for $x = 0.3$, T_C, σ and M_S reached their maximum value (in particular the value $M_S = 90$ Gauss/g corresponds to full polarisation of all the $3d$ electrons present). The resistivity ρ behaved like a semiconductor ($d\rho/dT < 0$) above T_C, but below T_C it was significantly reduced and had metallic behaviour ($d\rho/dT > 0$).

More experimental work followed in the next few years, resulting in a

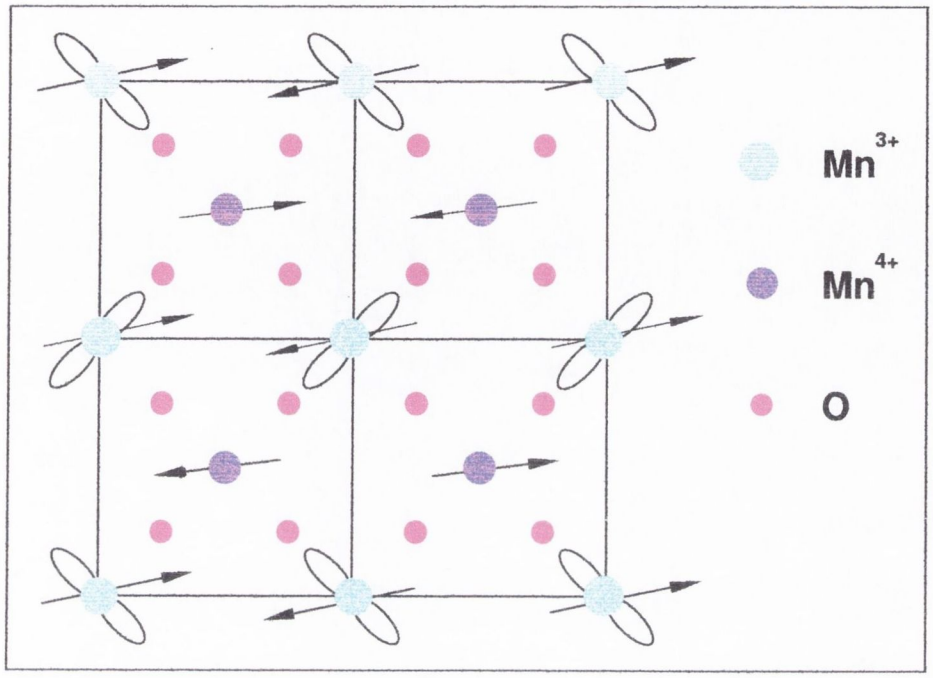

Figure 1.7: Schematic picture of spin, charge and orbital ordering in $La_{1/2}Ca_{1/2}MnO_3$.

huge effort exploring all the different aspects that could better characterise the manganites. In particular, low temperature properties were studied, such as specific heat, magnetisation, the Seebeck effect, the Hall effect, magnetoresistance, resistivity, I-V curves and so on [18, 19].

Volger [18] first described magnetoresistance and other transport properties in 1954. In his work, the magnetoresistance $\mathcal{R}(H)$, defined as in eq. (1.4), is plotted as a function of temperature; it is negative and has a peak near T_C. He also noted that a theory based on simple exchange interactions could not explain such transitions.

In 1955 Wollan and Koehler [20] produced an extensive neutron diffraction study of the magnetic properties of the series $La_xCa_{1-x}MnO_3$, which also included x-ray diffraction measurement of lattice distortions and ferro-

magnetic saturation data. They showed how nagnetic properties depended on the relative amount of trivalent and tetravalent manganese ion content and were able to identify the magnetic structure. The phase diagram that they produced [20] actually appears nowadays to be very accurate, despite the experimental limitations of the time. It closely matches more recent ones [21, 13] which is an amazing result if one considers the technology now available, resulting from years of experience in specmen fabrication, boosted by development in superconductivity.

In the following years the basic theoretical ideas were developed to explain such a behaviour. Anderson [22], in 1950, had already proposed a theory to explain antiferromagnetism in manganese oxide. He started from an idea by Kramers [23], who first pointed out the possibility to have an exchange coupling through the intermediate non magnetic ion. In antiferromagnetic compounds such as MnO, for example, magnetic ions are quite far apart (over 4 Å), so that their wave functions don't overlap, and are separated by non magnetic ions (oxygen); the exchange coupling between them, which is more then one tenth of ordinary exchange in metals, cannot come from the "ordinary" or "direct" exchange and was named superexchange. The basic assumption is that in the total wave function some weight has to be given to configurations in which an electron from the oxygen has hopped into an empty orbital of the magnetic ion; such an "excited state" would give some sort of paramagnetism to the oxygen and makes the exchange interaction possible.

Zener [24] suggested a mechanism, that he named double exchange, to explain the coexistence of ferromagnetism and metallic conductivity observed by Jonker and van Santen. They had already suggested that electrical conductivity in manganites should originate from the "migration" of Mn^{4+} ions,

i.e. an Mn^{4+} ion capturing an electron from a neighbouring Mn^{3+} ion. How this happened, though, was not trivial, since the ions are quite far apart and don't have an appreciable overlap; in addition to this they are separated by an O^{2-} ion which is closed shell. So Zener introduced the concept of simultaneous transfer of an electron from Mn^{3+} to oxygen and from oxygen to Mn^{4+} (double exchange). In a partially filled *d* shell the lowest energy state corresponds to the one in which all electron spins point in the same direction (this is known as Hund's rule); if the mobile electron retains this property and the spins of the *d* shells are parallel, then the two configurations $Mn^{3+}O^{2-}Mn^{4+}$ and $Mn^{4+}O^{2-}Mn^{3+}$ are degenerate. In other words double exchange requires both hopping electrons to have the same spin (the one of the O electron involved), i.e. charge carriers move most easily in a ferromagnetic environment. The coupling of degenerate levels will, of course, remove the degeneracy; Zener estimated the splitting of the degenerate levels to be proportional to the transition temperature T_C and, using classical arguments, he also predicted the electrical conductivity to be

$$\sigma \approx \frac{xe^2}{ah}\frac{T_C}{T}, \tag{1.6}$$

where a is the Mn-Mn distance and x is the Mn^{4+} fraction. The degeneracy of the two configurations, which is a consequence of the double Mn valence, makes double exchange intrinsically different from the ordinary superexchange introduced by Anderson [22] and based on an idea by Kramers [23]; this is very clear from the words of Zener himself:

> *"This indirect coupling through the oxygen ion by means of a double exchange should not be confused with the indirect coupling introduced by Kramers and now called superexchange. In our case, the system is inherently degenerate owing to the presence*

of Mn ions of two charges. The double exchange thereby introduced leads to a ferromagnetic alignment of spins. In Kramers' case only excited states are degenerate. The superexchange via these excited states leads to an antiferromagnetic alignment of spins" [24]

Zener's double exchange was later generalised by Anderson and Hasegawa [25] with a semiclassical model in which the spins of the ion cores are treated classically and the mobile electron quantum mechanically. The double exchange interaction was calculated in terms of a transfer integral, b, and the internal (Hund's rule) exchange integral, J_H. They found that Zener's level splitting is proportional to $\cos(\theta/2)$, where θ is the classical angle between the core spins. Their fundamental result is that the effective transfer integral becomes

$$t_{\text{eff}} = b\cos\left(\frac{\theta}{2}\right). \tag{1.7}$$

They showed that a quantum description of the spins could be achieved by replacing $\cos(\theta/2)$ with $(S_0 + 1/2)/(2S + 1)$, where S_0 is the total spin and S is the core spin. Anderson and Hasegawa also derived a form for the susceptibility as a function of temperature; they argued that it should follow a Curie-law behaviour at high temperature

$$\chi = \frac{C}{T} \tag{1.8}$$

with C constant, i.e $1/\chi$ should intercept the T axis at zero. This is actually in contrast with the experimental evidence, which shows a Curie-Weiss behaviour

$$\chi = \frac{C}{T - \theta_p}\ . \tag{1.9}$$

Eq. (1.9) describes quite well the susceptibility of ferromagnets in the paramagnetic region above T_C. A separate symbol, θ_p, is used for the paramagnetic

Curie temperature because experimentally it is always found to be greater than T_C.

DeGennes [26] discussed some effects of mobile electrons in an antiferromagnetic lattice at low doping, i.e. at low Mn^{4+} content. He showed that electrons (or holes) will necessarily produce some canting of the spin arrangement. He also introduced, for the first time, the concept of carriers that get "self-trapped" by distortions of the spin lattice, and that are now referred to as magnetic polarons.

A few years later, in 1972, a fully quantum mechanical treatment of the double exchange magnet was proposed by Kubo and Ohata [27]; they introduced the double exchange Hamiltonian

$$\mathcal{H} = -J_H \sum_{i,s,s'} (\mathbf{S}_i \cdot \sigma_{s,s'}) c_{is}^\dagger c_{is'} + \sum_{i,j,s} t_{ij} c_{is}^\dagger c_{js} \tag{1.10}$$

which is now an established starting point for theoretical studies. Here J_H is the intra-atomic (or Hund's rule) exchange energy, $\mathbf{S}_i$ is the spin due to the t_{2g} electrons and σ is the Pauli matrix; $c_{is}^\dagger$ and c_{is} are creation and annihilation operators for an e_g electron with spin s (up or down) at the Mn site i and finally t_{ij} is the transfer-matrix element.

As already mentioned, a simple picture based on double exchange is not able to offer a microscopic description of CMR in manganites. This point was made very clear by Millis, Littlewood and Shraiman [12] in 1995. In order to explain the experimental data on the resistivity of $La_{1-x}Sr_xMnO_3$ [10, 28], they proposed a theory that, in addition to double exchange, included the strong electron-phonon coupling arising from the Jahn teller splitting of the e_g levels. In the same way double exchange alone cannot explain the metal-insulator transition and all other particular behaviours they possess.

Manganites are examples of strongly correlated electron systems, i.e. systems where correlations between electrons are very important. Already back

in 1937 de Boer and Verwey [29] reported that some transition-metal oxides such as NiO, in spite of possessing a partially filled d band, were insulators. In the same year, Peierls [30] made the suggestion that the electron-electron correlation could be responsible for the insulating state. The strong Coulomb repulsion could prevent the electrons from moving through the lattice, because they would have to spend a long time in ions already occupied by other electrons. Great theoretical progress in understanding the physics of strong correlated electrons and the metal-insulator transition has been achieved by Mott in a series of papers [31, 32, 33, 34, 35]; so the insulating state is usually called a Mott (or Mott-Hubbard) insulator.

The simplest way to describe such transitions would be through some lattice fermion model, which should include the possibility of electron hopping as well as the Coulomb interaction. The most famous and celebrated among these models is the Hubbard model [36, 37, 38, 39, 40]. In a second-quantised form its Hamiltonian is given by

$$\mathcal{H} = -\sum_{i,j,s} t_{ij} c_{is}^{\dagger} c_{js} + U \sum_{i} n_{i\uparrow} n_{i\downarrow} \quad . \tag{1.11}$$

The first term describes the hopping of electrons from site i to site j; the second one accounts for the Coulomb repulsion (U) between electrons. n_{is} ($s = \uparrow, \downarrow$) is the number operator defined as $n_{is} \equiv c_{is}^{\dagger} c_{is}$. This model only considers electrons in a single band and doesn't take into account any complications like orbital degeneracy; nevertheless it is successful in the description of both the insulating and the metallic state of the system and of the basics of the exchange interaction. The limit of weak interaction ($U << t$) corresponds to the metallic state; the system is metallic even for half-filled bands (i.e. one electron per site, $n = 1$), independent of the distance between sites. Clearly, for large enough distance between sites (small t) and $n = 1$, electrons are localised on each site and the system should be an insulator

(Mott insulator). This corresponds to the second term in eq. (1.11), which contains the on-site Coulomb repulsion (U). The cost of creating a charge excitation, i.e. of moving one electron from its site to another one, will be U, because that's the repulsion energy the electron will experience in going onto an already occupied site. On the other hand the gain for this transfer will be $\sim t$, but if $U >> t$ (strong interaction) the material will remain an insulator with a gap $\sim U - t$. So the second term of the Hamiltonian (1.11), which is the main term in this case, leads to the formation of localised moments on each site; this state is characterised by spin degeneracy. The first term in eq. (1.11), the electron hopping term, lifts the spin degeneracy and, in second order perturbation theory in $t/U << 1$, leads to an antiferromagnetic exchange interaction between these localised magnetic moments [36, 41]. This is usually described by an effective exchange Hamiltonian

$$H_{\text{eff}} = J \sum_{i,j} S_i S_j \tag{1.12}$$

with

$$J = \frac{2t^2}{U} \quad . \tag{1.13}$$

In other words the virtual hopping of electrons leads to an antiferromagnetic Heisenberg exchange interaction. This is the superexchange interactions described above, and it is the main mechanism of exchange in magnetic insulators.

The Hubbard model is still too over-simplified and doesn't give a complete theoretical description of strongly correlated electron systems. Other effects have to be taken into account such as the orbital degeneracy, the electron-phonon coupling (which is also responsible for the JT effect). Currently, theoretical study of manganites is done using *ab initio* methods (as in the present work) or model Hamiltonian calculations that start with a

parametrised version of the problem. Electronic properties of transition-metal oxides are given by the interplay of many different interactions which are of more or less the same order of magnitude ($\propto$ 1 eV). They are summarised as follows [3]:

a) the Mott-Hubbard interaction U_{dd}: energy for the creation of the excitation

$$d^n \;\; d^n \Rightarrow d^{n-1} \;\; d^{n+1} \;\; ;$$

b) the charge-transfer interaction U_{pd}: energy cost for the transfer of an oxygen p electron to the neighbouring Mn ion, i.e. for the excitation

$$p^6 \;\; d^n \Rightarrow p^5 \;\; d^{n+1} \;\; ;$$

c) the transfer integral t, or equivalently the free particle bandwidth W:

$$W = 12t \;\; ;$$

d) the Hund's rule exchange interaction $U_{\rm ex}$: energy needed to flip a d electron spin:

$$U_{\rm ex} = 2J_{\rm H} \;\; ;$$

e) the crystal-field splitting $\Delta_{\rm cf}$;

e) the Jahn-Teller splitting of the e_g orbitals $\delta_{\rm JT}$.

1.3 End point compounds

Both end-point compounds of the series $La_xCa_{1-x}MnO_3$ are antiferromagnetic insulators, though with different spin structures and crystal symmetries. This section summarises their main properties derived from experiments and from theoretical studies.

1.3.1 $CaMnO_3$

$CaMnO_3$ is experimentally found to crystallise in the ideal cubic perovskite structure (Fig. 1.1) with a lattice constant $a = 3.73$ Å [20]. Some slight deviations from this structure have been observed; some samples present monoclinic [20] or orthorhombic structure [42, 43], but they differ very little from the ideal cubic one. The Néel temperature (T_N) is around 110-130 K [20, 21]. Below this temperature $CaMnO_3$ is an antiferromagnetic insulator of type G. In this compound manganese is a 4+ ion (d^3). The majority t_{2g} orbitals are fully occupied, the minority are all empty; there are no e_g electrons, so the cubic structure is stable.

An *ab initio* study carried out by Pickett and Singh [44] analysed the electronic structure and the transport properties in the series $La_xCa_{1-x}MnO_3$; their calculations were performed using the Local Spin Density Approximation (LSDA) to the Density Functional Theory (DFT - see next chapter). For $CaMnO_3$, using total energy calculations, they found that the G-type AF is, as expected, the ground state. From band structure and density of state analysis they derived information on transport properties. In particular, they predicted that the G-type is actually an insulator, with a calculated gap of 0.42 eV, while the (experimentally inaccessible) A-type and FM structures are metallic and half-metallic (metallic majority but insulating minority bands) respectively. The ground state magnetic moment, which they calculated to be 2.48 μ_B, is in agreement with the experimental one of 2.65 μ_B, obtained from fitting to neutron diffraction data [20]. The Hund's rule value, 3 μ_B, is indeed expected to be reduced by Mn d - O p hybridisation. Similar results were obtained by Satpathy and collaborators [45], using the same calculation method. This work also explored electron correlation effects, which are very important for the transition-metal binary oxides; the authors es-

timated the on-site Coulomb interaction U and the intra-atomic exchange parameter J_H, which have almost identical values ($U \approx 10$ eV and $J_H \approx 0.9$ eV) for both $CaMnO_3$ and $LaMnO_3$.

The ground state electronic structure of $CaMnO_3$ was also studied by Freyria-Fava *et al.* [46] using a different *ab initio* approach, the Unrestricted Hartree-Fock approximation (UHF - see next chapter). Again, the G-type AF is the most stable structure, and the compound is a large-gap (8.9 eV) insulator. It is actually a characteristic of the Hartree-Fock approximation to give considerably larger gaps compared to DFT. The calculated magnetic moment is 3.25 μ_B in this case.

1.3.2 $LaMnO_3$

$LaMnO_3$ is at the other end of the series $La_xCa_{1-x}MnO_3$. Because all Mn ions have a valence of 3+, the compound is characterised by strong J-T distortions and the symmetry is far away from the idealised cubic perovskite.

The crystallographic parameters (lattice vectors and atom positions) were experimentally determined by Elemans and co-workers [47] using neutron powder diffraction. The symmetry of the structure is the distorted, orthorhombic *Pnma* [8], space group No. 62 in the International Tables [48]; it is also known as the gadolinium orthoferrite ($GdFeO_3$) structure type [49, 50]. Such a structure contains more distortions than the pure Jahn-Teller ones since the oxygen octahedra are also tilted and rotated. Eleman's parameters are reported in Table 1.1. The *Pnma* structure can be derived from the cubic perovskite structure by the following operations, each resulting in a reduction of symmetry [44]:

i) Rotation of an oxygen around the z axis, traditionally referred as the b crystal direction; because all octahedra remain connected, adjacent

	Wyckoff site	x/a	y/b	z/c
La	$4c$	0.549	1/4	0.010
Mn	$4a$	0	0	0
O_I	$4c$	-0.014	1/4	-0.070
O_{II}	$8d$	0.309	0.039	0.224

Table 1.1: Structural fractional parameters of *Pnma* $LaMnO_3$ from Elemans *et al* [47]. $a = 5.742$Å, $b = 7.668$Å and $c = 5.532$Å at 4.2 K.

ones in the $x-y$ (or $a-c$) plane rotate in opposite directions, resulting in a $\sqrt{2} \times \sqrt{2}$ doubling of the cubic unit cell.

ii) Tilting of an octahedron along the Mn-O-Mn direction in the $a - c$ plane; as a consequence, different layers tilt in opposite direction, so that there is a further doubling of the cell along b.

The net result is an orthorhombic cell in which $b < c < a$ and corresponding approximately to a $\sqrt{2} \times 2 \times \sqrt{2}$ quadrupling of the cubic cell; its volume is the same as a cube with an edge length of 3.934 Å. As can be seen from Table 1.1, there are a total of seven internal structural parameters (the others correspond to high symmetry positions for those ions): two each for La and O_I, situated on the Wyckoff $4c$ sites [8, 51] with mirror symmetry and three for O_{II} on the general $8d$ site. Finally, Mn is situated on the $4a$ site with inversion symmetry. Mn-O bond lengths, which are 1.97 Å in the ideal cubic perovskite structure, become 1.96 Å (medium distance) along the b vertical direction, whereas a short and a long distance (1.91 and 2.18 Å respectively) alternate in the $a - c$ plane. Fig. 1.8 clearly shows distortions in the experimental *Pnma* structure of $LaMnO_3$. Apart from the J-T effect, distortions in $LaMnO_3$ have also been attributed to the large size of the La^{3+} cation [49, 52], which doesn't favour a stable cubic structure according to the Goldsmith tolerance factor (eq. (1.1)).

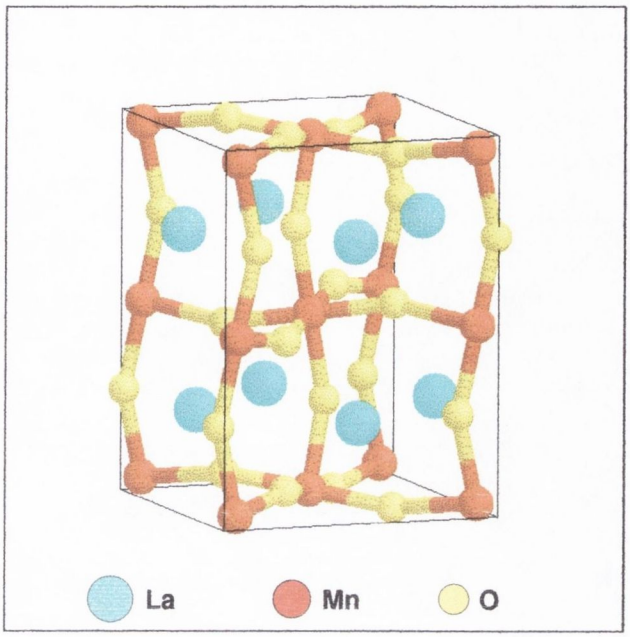

Figure 1.8: Experimental *Pnma* structure of $LaMnO_3$; the distortion from the ideal cubic perovskite structure is evident, as well as the tilt and rotation of the oxygens octahedron.

As a consequence of the J-T effect, the alternation of a short and a long Mn-O bond length in the $a-c$ plane results in orbital ordering, shown in Fig. 1.9. The occupied e_g orbital, in such a plane, is alternatively $d_{3x^2-r^2}$ and $d_{3y^2-r^2}$. Experimental evidence for orbital ordering in $LaMnO_3$ has been found by Murakami *et al.* [53] after observation that it led to intensity at Bragg peaks indexed $(h00)$ and $(0k0)$, with h and k odd, which would be nominally extinct.

$LaMnO_3$ is, like $CaMnO_3$, an antiferromagnetic insulator. Its magnetic structure is A-type AF, with ferromagnetically ordered $a-c$ planes stacked along b (often referred as the vertical direction) in an antiferromagnetic way. The transition temperature T_N is around 140-160 K [20, 21]. The compound also undergoes a structural phase transition at $\approx$ 750 K, where its symmetry

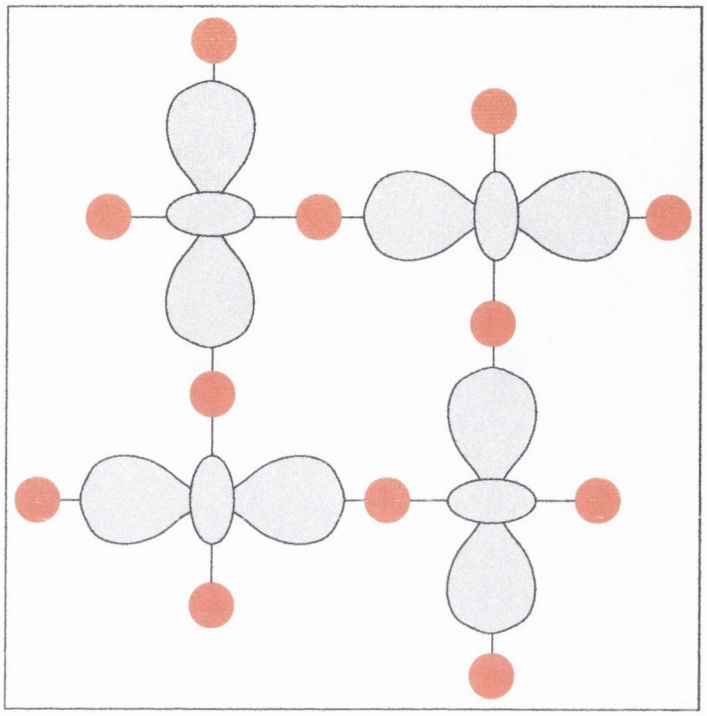

Figure 1.9: The Jahn-Teller effect and consequent orbital ordering in $LaMnO_3$. The alternation of a long and a short Mn-O bond length in the $a-c$ plane results in alternate occupation of $d_{3x^2-r^2}$ and $d_{3z^2-r^2}$ orbitals.

is described as cubic [54].

Results on transport and magnetic properties of $LaMnO_3$ were reported by Pickett and Singh [44] and Satpathy *et al.* [45] in their already cited papers; similar LSDA calculations can be found in ref. [55]. Calculations carried out on a cubic idealised structure with the same volume as the experimental one showed that the conductivity can be described as metallic and that the minimum total energy belongs to the FM spin arrangement; the magnetic moment was calculated to be 3.38 μ_B in the FM case and 2.89 μ_B in the AF case [44], again below the Hund's rule value of 4 μ_B. Use of the distorted experimental structure was necessary to open the gap (0.12 eV is the calculated one [44], compared to $\approx$ 0.2 eV from experiments [56, 57])

and to lower the observed A-type AF below the FM; the distortion also strengthens the magnetic moment, which becomes 3.38 μ_B [44], compared to an experimental value of 3.89 μ_B [20]. The authors of ref. [45] also showed that a calculation on the cubic structure in which only an in-plane J-T distortion was present already reproduced the correct ground state, and they concluded that such a distortion is the main one responsible for the magnetic and electronic properties of $LaMnO_3$.

Unrestricted Hartree-Fock calculations [58] confirmed the same kind of magnetic and structural properties. There were, nevertheless, large differences in the prediction of band structures between the two approaches. As the authors of ref. [58] pointed out, in LSDA the Mn *d* bands lie near the top of the valence band, above the O *p* bands, whereas in their UHF the opposite was found. The same UHF band behaviour was predicted by Saitoh *et al.* [59], who fitted experimental photoemission results to a cluster configuration interaction model. And in the same ref. [45], using LSDA corrected with on-site Coulomb interaction U (the LDA + U approach), the order of the bands was switched compared to pure LSDA.

Exactly the same applies to the band structure of $CaMnO_3$ [44, 45, 46].

1.4 Intermediate concentrations. CMR

As previously mentioned, the series of $La_xCa_{1-x}MnO_3$ appeals for possible applications in magnetic sensor devices because for concentrations $0.2 < x < 0.5$ and low temperatures these materials are ferromagnetic and their conductivity is metallic (see Fig. 1.2). Lowering the temperature, the resistivity ρ increases (by 2 - 3 orders of magnitude) and reaches a maximum at a temperature T^* very close to the Curie temperature (but not exactly coincident with it; sometimes, nevertheless, they are assumed to be the same); below

T^*, then, ρ drops again very rapidly (within a few Kelvin). Application of a magnetic field lowers the resistivity around T^* and the percentage decrease can be very huge in a field of a few Tesla (typically $\sim$ 5 Tesla): this is the CMR phenomenon, which is mainly observed for $x \approx \frac{1}{3}$.

After the discovery by Jin *et al.* [11], many experiments have been performed and various values for CMR have been reported. The first results on a single crystal sample ($La_{0.65}(CaPb)_{0.35}MnO_3$) were given by Liu *et al.* [60] who found $\mathcal{R}(H) = 3$ (300 %). A study of laser deposited films of $La_{0.7}Ca_{0.3}MnO_3$ [61, 62] reported a value of $\mathcal{R}(H) \approx 10$. An interesting consequence of the application of a magnetic field is that T^* is shifted upward, typically by $dT^*/dH \approx 10$ K/T.

Essential ingredients for the comprehension of the physics of manganites are, as has already been stated, the spin, charge and orbital degrees of freedom which are available for these compounds. In particular, e_g electrons play a special role in producing the non-conventional metal-insulator transition via the coupling of the three types of ordering. The main parameters, i.e. the band filling (or doping level) and bandwidth (or electron hopping) can easily be controlled by varying the chemical composition; so the different regions of the phase diagram can be studied.

In the metallic range ($0.2 < x < 0.5$), the drop of ρ below T_C indicates that high temperature resistivity is mainly due to scattering of conduction electrons by disordered spin; as a consequence, the application of a magnetic field can recover the low resistivity state. What was also found is that in order to observe a metal-insulator transition the residual resistivity ρ_0 of the sample must be greater then a critical resistivity ρ_c [63].

Charge and orbital ordering is more evidently observed for x around 0.5. Because they are short range correlations, their presence results in an in-

Exchange	Sign
$J_{ab}^{(1)}$	-
$J_{ab}^{(2)}$	+
$J_{c}^{(1)}$	+
$J_{c}^{(2)}$	+

Table 1.2: Sign of exchange interactions in $La_{1/2}Ca_{1/2}MnO_3$; + corresponds to AF, - to FM interaction.

sulating state; when they disappear, a transition to a metal takes place. The 50-50 compound, $La_{1/2}Ca_{1/2}MnO_3$, is an antiferromagnetic insulator of CE-type (see Fig. 1.3) at low temperature; then, as the temperature is increased, it first becomes ferromagnetic ($T_N \approx 155$ K) and then paramagnetic ($T_C \approx 255$ K) [64]. In the CE-type four different magnetic couplings can be identified; they are usually referred to as follows:

i) $J_{ab}^{(1)}$, the Mn^{3+}-Mn^{4+} coupling corresponding to an occupied e_g orbital on the Mn^{3+} pointing toward the neighbouring Mn^{4+} in the plane of Fig. 1.7;

ii) $J_{ab}^{(2)}$, the Mn^{3+}-Mn^{4+} coupling corresponding to an occupied e_g orbital on the Mn^{3+} oriented perpendicular to the neighbouring Mn^{4+} in the plane of Fig. 1.7;

iii) $J_{c}^{(1)}$, the Mn^{4+}-Mn^{4+} coupling between planes;

iv) $J_{c}^{(2)}$, the Mn^{3+}-Mn^{3+} coupling between planes.

No experimental values have been reported, but the signs of the interactions are known. They are summarised in Table 1.2.

Charge and orbital ordering in this compound was shown earlier in Fig. 1.7. Using a dark-field imaging technique [14], transition to ferromagnetism

has been attributed to a commensurate-to-incommensurate charge ordering transition. Experimental studies [14, 64] also reveal how charge ordered domains can persist in the incommensurate phase; such a mysterious coexistence of ferromagnetism and charge ordering appears in the form of striped domains [65].

The experimentally observed charge distribution in $La_{1/2}Ca_{1/2}MnO_3$ (see Fig. 1.7) has been explained using a model of localised classical electrons coupled to lattice degrees of freedom and, via the Coulomb interaction, to each other [66].

Magnetic and transport properties have been studied in the LSD approximation for $x = \frac{1}{4}$ and $x = \frac{1}{3}$ [44]. The switch from AF to FM was reproduced by these calculations, in which a study of band structure reveals the importance of hybridisation between Mn d and O p states and the dependence of such a hybridisation on the spin structure.

1.5 The exchange coupling mechanism

This section is a short review of experimental and theoretical achievements in the understanding of the exchange coupling mechanism in manganites; it starts with Goodenough's model [67], which was the first systematic attempt, in 1955, to explain the magnetic behaviour of the recently discovered manganites. As already pointed out, a complete description is based on double exchange and superexchange, but it also has to include other more complicated aspects such as orbital degeneracy and the electron-phonon interaction leading to the Jahn-Teller splitting of the e_g levels.

A note is needed at this point to clarify the convention that will be adopted throughout the present work, as there are many different ways of defining the Heisenberg Hamiltonian that describes the exchange (one is

given, for example, in eq. (1.12)). In what follows the form adopted will be the one due to Domb and Sykes [68],

$$\mathcal{H} = \sum_{<ij>} J_{ij} \frac{\hat{\mathbf{S}}_i \cdot \hat{\mathbf{S}}_j}{S^2} \quad . \tag{1.14}$$

$\hat{\mathbf{S}}_i$ is the spin operator, S is the magnitude of the total spin of an ion and J_{ij} is the exchange coupling between spins at sites i and j; when $J < 0$ the coupling is ferromagnetic, when $J > 0$ the coupling is antiferromagnetic. The symbol $< ij >$ denotes a pair of neigbouring sites where double counting is excluded. Of course not all authors use the above convention, and conversions are often needed to compare results. In the remaining of this work such conversions will always be carried out, and results from the literature will always be reported according to (1.14).

1.5.1 Goodenough's model

The first comprehensive attempt to give an adequate description of the exchange coupling mechanism was produced by Goodenough [67] in 1955. The series of manganites $La_xCa_{1-x}MnO_3$ had been recently studied by Wollan and Koehler [20] and a theoretical explanation was needed. Goodenough proposed a model in which he discussed Mn-O hybridisation, leading to the concept of semicovalent exchange and to a successful description of the correlation between spin, orbital ordering and crystallographic structure.

The chemical binding in the manganites was explained in terms of specific bond types between Mn ions which depended on the charge and spin of pair of ions separated by an O ion. Formally the ions have charges of +3 or +4 (Mn) and -2 (O). However there is a degree of covalency (that Goodenough named semicovalency) in the Mn-O bonds and charge is shared between the O ion and its Mn neighbours in the Mn-O-Mn chain. The specific type of

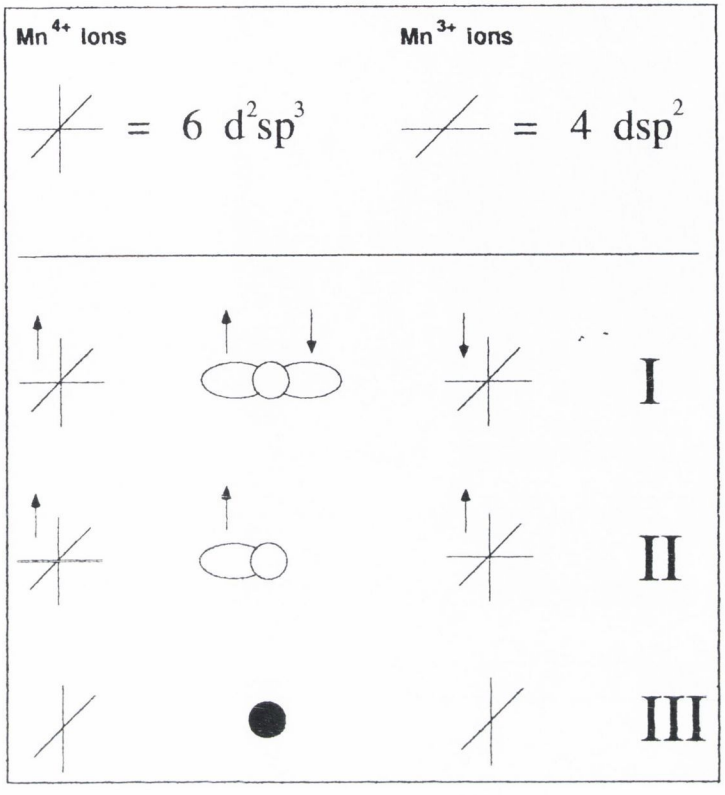

Figure 1.10: Schematic summary of the Goodenough model (see Table I of ref. [67]) showing the empty hybrids for each ionic configuration and the types of interactions.

binding depends on the relative spin orientation of the Mn ions as well as on the availability of empty Mn hybrid orbitals to accept O 2p electrons. If the Mn spins are parallel (FM coupling), a consequence of Pauli's exclusion principle is that only one of the O 2p electrons can be effectively shared with the Mn ion (the one with the spin parallel to the Mn ions' spin), but if the Mn spins are anti-parallel (AF ordering) *both* O 2p electrons can be shared, resulting in stronger Mn-O bonds than in the FM coupling case. Table I of ref. [67] is summarised in Fig. 1.10. O 2p electron sharing is illustrated by a double-lobe hybrid for AF coupling (type I interaction) and a single-lobe hybrid (type II interaction) for FM coupling. In terms of the Mn-Mn

separation, interaction I corresponds to a short distance, whereas interaction II corresponds to a large one.

The nature of Mn empty hybrids depends on the charge of the ion; according to Goodenough's model, an Mn^{4+} ion has an octahedral set of 6 d^2sp^3 empty hybrid orbitals formed by empty 3d, 4s and 4p orbitals while an Mn^{3+} ion has a square planar set of 4 dsp^2 empty hybrid orbitals. Mn-O covalent bonds only exist if the Mn ion has an empty hybrid pointing toward a neighboring O ion, otherwise the interaction is purely ionic (type III interaction, indicated by filled circles in Fig. 1.10); in the latter case the Mn-Mn distance is the longest.

Using this set of prescriptions, Goodenough was able to predict the magnetic structure, the nature of the exchange coupling and their relationship with the crystal symmetry across the $La_xCa_{1-x}MnO_3$ series.

For $x = 1$ ($CaMnO_3$) all Mn ions are Mn^{4+}; there is always an empty orbital available and every Mn-O bond can be semicovalent. All Mn^{4+}-Mn^{4+} interactions are of type I, with any ion antiferromagnetically coupled to its six neighbours, i.e. with a positive exchange coupling ($J > 0$) between them. Another consequence is that all Mn-Mn distances are the same and the cubic structure is stable.

The other end point compound, $LaMnO_3$, only contains Mn^{3+} ions. For Mn^{3+}, more than one combination of spin and hybrid orientation (and therefore of types of interaction) is possible; each of them would necessarily produce a distortion in the lattice, due to the different bond lengths associated with the different interactions. Goodenough describes one possible arrangement, in which the coplanar set of four empty hybrids is ordered in one plane, giving interactions of type I within that plane. Between planes, with no orbitals available for bonding, interactions would be of type III. This kind

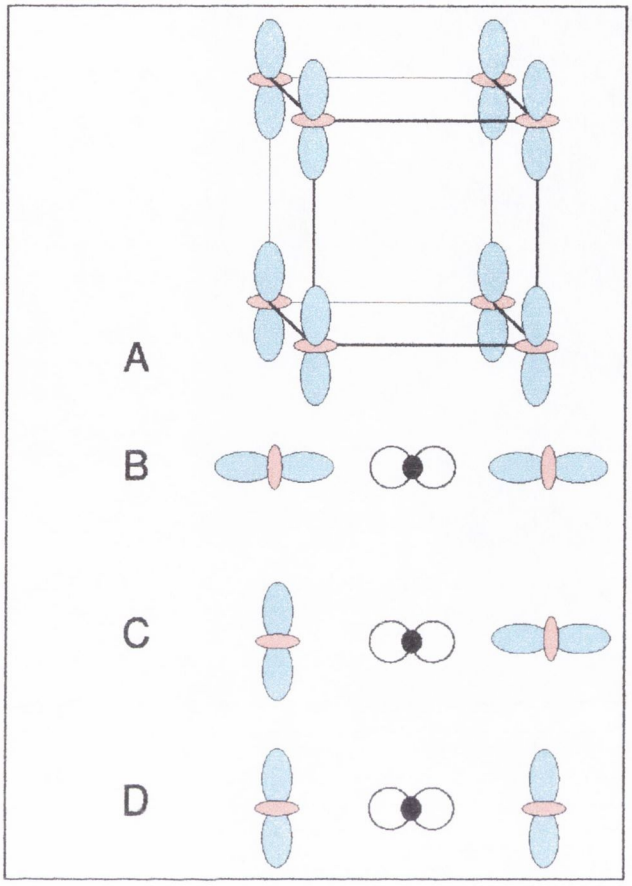

Figure 1.11: Higher energy ordering of Mn empty orbitals in $LaMnO_3$. (A) Possible arrangement resulting when occupied orbitals are $d_{x^2-y^2}$; (B) empty orbital arrangement with AF spin coupling (interaction type I); (C) empty orbital arrangement with FM spin coupling (interaction type II); empty orbital arrangement with weak spin coupling (interaction type III). Black circles represent oxygen ions.

of arrangement of empty orbitals is shown in Fig. 1.11(A). It is clear that such an ordering would produce a large crystal distortion to a tetragonal symmetry and would be energetically unfavourable.

There is, anyway, a possible ordered configuration which would produce smaller lattice distortions and would therefore be more stable. This is sketched in Fig. 1.12. The spins of the Mn ions alternate along the $\mathbf{a}_2$

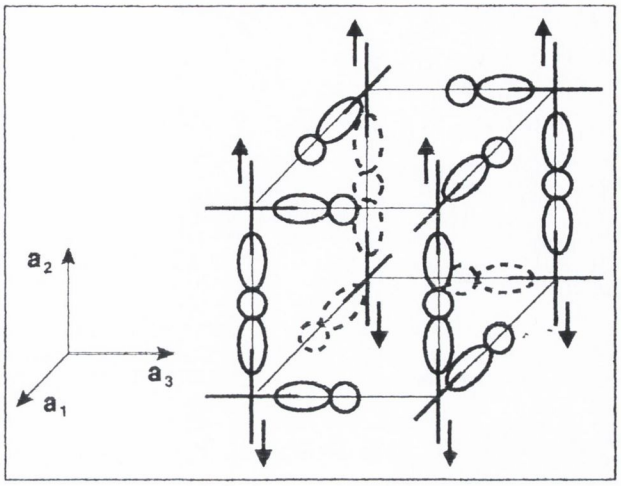

Figure 1.12: Predictions of the Goodenough model for $LaMnO_3$. The antiferromagnetism is A-type and the symmetry is tetragonal with $\mathbf{a}_2 < \mathbf{a}_1 = \mathbf{a}_3$.

direction, while they remain the same in planes perpendicular to $\mathbf{a}_2$; interactions of type III, which would cause the largest distortion in the lattice, are avoided and there are only interactions of type I (along $\mathbf{a}_2$, the antiferromagnetic direction) and of type II (in ferromagnetic planes perpendicular to the $\mathbf{a}_2$ directions). So Goodenough correctly predicted the compound to be an A-type antiferromagnet, with intra-plane FM coupling ($J < 0$) and inter-planar AF coupling ($J > 0$) and tetragonal symmetry ($\mathbf{a}_2 < \mathbf{a}_1 = \mathbf{a}_3$). He also noted that, due to the fact that in type II interactions the O ion is closer to the Mn ion with an empty orbital pointing toward it (with which it forms a covalent bond), the symmetry will actually be orthorhombic and orbital ordering should be observed.

Goodenough extended his analysis to all ranges of doping using the same kind of arguments. Regarding the $x = 0.5$ composition, for example, he successfully predicted the occurrence of charge ordering and, among all possible spin and orbital arrangements he identified the CE-type structure to be the most stable.

1.5.2 Experimental results

A few experimental works have been carried out aimed at a determination of exchange coupling constants. They make use of different techniques, among which are neutron scattering and measurement of the Néel temperature.

Moussa et al. [69] carried out a neutron scattering study on powder and single crystals of the orthorhombic phase of lanthanum manganite; they found their samples to be in the antiferromagnetic phase below $T_N = 139.5$ K. Their spin wave spectrum was well accounted for by a simple Heisenberg Hamiltonian plus a term including a single ion anisotropy contribution

$$\mathcal{H} = H_{\text{Heisenberg}} - D\sum_i S_i^{z2} \quad . \tag{1.15}$$

Only two exchange integrals were needed to describe the experimental data: $J_{||}$ between nearest neighbours in the basal plane and $J_\perp$ along the vertical direction. They found

$$J_{||} = -6.6 \text{ meV} \tag{1.16}$$

$$J_\perp = 4.6 \text{ meV}. \tag{1.17}$$

According to the sign convention in eq. (1.14), $J_{||}$ is ferromagnetic and $J_\perp$ is antiferromagnetic; the former is a factor 1.4 larger then the latter. They commented that such a result was in agreement with the expected behaviour according to Goodenough's prediction and that it was a signature of the existence of orbital ordering in $LaMnO_3$.

In later work the same experimental group [70] extended its study to the region of low doping ($x = 0.05$, $x = 0.08$), where new spin dynamics appear in addition to the normal superexchange spin waves.

Very similar results ($J_{||}$ = -6.7 meV, $J_\perp$ = 4.8 meV) were obtained in another neutron scattering study on an $LaMnO_3$ single crystal by Hirota *et al.* [71].

For $CaMnO_3$ only one exchange parameter is needed to describe the G-type AF interaction of Mn ions with their nearest neighbours. J can be estimated from the experimental Néel temperature (T_N = 110 K [20]) using the Rushbrook-Wood approximation [68]

$$\frac{k_B T_N}{J} = (z-1)(0.579s(s+1) - 0.072) \quad , \tag{1.18}$$

where k_B is the Boltzman constant, s is the spin and z is the coordination number; its value is

$$J = 6.6 \text{ meV}. \tag{1.19}$$

1.5.3 *Ab initio* and model Hamiltonian calculations

Many theoretical studies exist that have been able to calculate exchange couplings for $CaMnO_3$ and $LaMnO_3$. Most of them make use of models based on parametrised Hamiltonians, so that complications like the J-T effect, or the large on-site Coulomb interaction U, can be taken into account. Some of them are reviewed in this section, with the aim of giving some ideas of the way they are generated and of the results they produce.

There are, nevertheless, also *ab initio* calculations that proved successful, despite the fact that such a method is thought not to give good quantitative results for strongly correlated electron systems. Among them, those carried out in a work by Solovyev *et al.* [72] gave exchange couplings for $LaMnO_3$ in the Local Spin Density approximation. A crucial role was attributed by the authors to lattice distortions (i.e. to the J-T effect) which were found to be responsible for the actual magnetic structure of the compound. Without J-T distortions, the system remains ferromagnetic. The structural modifications induced by distortions can be defined by the parameter

$$R_t = \frac{d_L}{d_S} \quad , \tag{1.20}$$

where d_L and d_S are the long and short Mn-O bond length in the basal plane. In the experimental structure $R_t \sim 1.13$, whereas Solovyev *et al.* found that $J_\perp$ switched to an antiferromagnetic positive sign at $R_t \sim 1.12$, being still ferromagnetic at the experimental value. The calculated exchange couplings were

$$J_{||} = -9.1 \text{ meV} \tag{1.21}$$

$$J_\perp = -3.1 \text{ meV}. \tag{1.22}$$

Nevertheless, in their calculations the exchange along the vertical direction due to second neighbour interaction was of comparable size; once this interaction was included in the expression for $J_\perp$, its antiferromagnetic behaviour could be recovered.

A different *ab initio* approach, the UHF approximation, was used by Su *et al.* [58] to study the electronic structure of cubic and orthorhombic $LaMnO_3$. Exchange couplings $J_{||}$ and $J_\perp$ were both ferromagnetic in the cubic idealised structure, as a consequence of the FM structure being the ground state. In the distorted orthorhombic structure the correct sign of the exchange was found, even if the values,

$$J_{||} = -3.5 \text{ meV} \tag{1.23}$$

$$J_\perp = 0.8 \text{ meV}, \tag{1.24}$$

particularly $J_\perp$, did not agree well with experiment. In such a calculation, interactions between non-nearest neighbours were practically zero, in contrast to LSDA [72].

Turning now to model Hamiltonian calculations, the first to be mentioned is the one carried out by Millis [73], who gave an estimate of exchange coupling in $CaMnO_3$ and $LaMnO_3$ using arguments based on Anderson's superexchange. It is, in other words, a quantitative version of Goodenough's

	State Label	Mn (e_g)	O ($2p_\sigma$)	Mn (e_g)	Energy
$CaMnO_3$	C1	0	2	0	0
	C2	1	1	0	Δ'
	C3	0	1	1	Δ'
	C4	1	0	1	$2\Delta' + U_O$
$LaMnO_3$	L1	1	2	1	0
	L2	2	1	1	Δ
	L3	1	1	2	Δ
	L4	2	0	2	$2\Delta + U_O$
	L5	2	2	0	U_{Mn}
	L6	1	0	1	U_{Mn}

Table 1.3: States, occupancies and energies used in Millis' theory [73].

model. Millis focused on an Mn-O-Mn bond and in particular on the role of Mn e_g and O $2p_\sigma$ orbitals. Then, starting from an idealised ground state, he considered all possible states than can be reached with one or two electron hops. For $CaMnO_3$ the ground state has no e_g electrons on the Mn atoms and two electrons on the oxygen; for $LaMnO_3$ the ground state has one e_g electron on each Mn and two electrons on O. t_{2g} electrons were supposed not to be involved in these transitions and to form an "inert core" of spin 3/2; e_g electrons, on the other hand, were assumed to be always parallel to the core spins (Hund's rule). Table 1.3 (taken from ref. [73]) lists all states that can be taken into account and defines all energies involved in the various processes. States that differ by a single electron hop are connected by a matrix element t. Hamiltonian matrices can now be written for both compounds in the basis of Table 1.3, and the magnetic exchange constant can be calculated in terms of the difference between the ground state energy with core spins parallel and the state with core spins antiparallel.

The way to proceed is shown here in the case of $CaMnO_3$; for $LaMnO_3$

the situation is complicated by the presence of the extra e_g electron on the manganese, but a very similar procedure applies. States entering the Hamiltonian for parallel spins are C1, C2 and C3, whereas all states C1-C4 enter the one for antiparallel spins:

$$H_{\uparrow\uparrow} = \begin{pmatrix} 0 & t & t \\ t & \Delta' & 0 \\ t & 0 & \Delta' \end{pmatrix} \quad . \tag{1.25}$$

$$H_{\uparrow\downarrow} = \begin{pmatrix} 0 & t & t & 0 \\ t & \Delta' & 0 & t \\ t & 0 & \Delta' & t \\ 0 & t & t & 2\Delta' + U_O \end{pmatrix} \quad . \tag{1.26}$$

4th order perturbation theory yields, for the difference in lowest eigenvalues,

$$E_{\uparrow\uparrow} - E_{\uparrow\downarrow} = \frac{2t^4}{\Delta'^2 \left(\Delta' + U_O/2\right)} \quad , \tag{1.27}$$

which is of order t^4/Δ'^3. Millis interpreted this difference as the classical Heisenberg energy $2Js^2$ and, taking $s = 3/2$, the exchange constant is

$$J = \frac{4t^4}{9\Delta'^2 \left(\Delta' + U_O/2\right)} \quad . \tag{1.28}$$

Using the Rushbrook-Wood approximation approximation (eq. (1.18)), together with the experimental Néel temperature $T_N \approx 110$ K, Millis found $J \approx 10$ K (i.e. 7.8 meV using our convention).

Feiner and Oleś [74] derived a spin orbital model for $LaMnO_3$ which included the following terms:

$$H = H_{e_g} + H_{t_{2g}} + H_{JT} + H_{\tau} \quad . \tag{1.29}$$

H_{e_g} and $H_{t_{2g}}$ are the superexchange terms due to e_g and t_{2g} excitations

$$H_{e_g} \longrightarrow \left(t_{2g}^3 e_g\right)\left(t_{2g}^3 e_g\right) \rightleftharpoons \left(t_{2g}^3\right)\left(t_{2g}^3 e_g^2\right)$$

$$H_{t_{2g}} \longrightarrow \left(t_{2g}^3 e_g\right)\left(t_{2g}^3 e_g\right) \rightleftharpoons \left(t_{2g}^2 e_g\right)\left(t_{2g}^4 e_g\right) \quad ,$$

whereas H_{JT} and H_{τ} describe the J-T interaction and the contribution of the crystal field. The authors identified in H_{e_g}, i.e. in the hopping of an e_g electron from its site to the neighbouring one, the strongest channel of superexchange. It should be noted that, unlike the model proposed in [73], oxygen electrons are not included in the hopping process and don't take part in superexchange. For $CaMnO_3$, where no e_g electrons are present, Feiner and Oleś pointed out that $H_{t_{2g}}$ would be the only channel of superexchange; they calculated, in this case,

$$J = 10.3 \text{ meV} \quad , \tag{1.30}$$

which corresponds to $T_N = 124$ K. For $LaMnO_3$ the two exchange couplings were calculated as

$$J_{\parallel} = -9.2 \text{ meV} \tag{1.31}$$

$$J_{\perp} = 7.0 \text{ meV}; \tag{1.32}$$

though they are higher then the experimental value, the ratio $\frac{J_{\perp}}{|J_{\parallel}|} = 0.77$ agrees well with the experimental 0.7 [69].

Meskine, König and Satpathy [75] have proposed an electronic Hamiltonian model for the Mn-O-Mn triad to explain the microscopic origin of the exchange interaction in manganites. The Hamiltonian for the triad was written as a sum of three contributions, namely kinetic, Coulomb and Hund's rule energies:

$$\mathcal{H} = \mathcal{H}_{\text{KE}} + \mathcal{H}_{\text{Coulomb}} + \mathcal{H}_{\text{Hund}} \quad . \tag{1.33}$$

Such a Hamiltonian was exactly solved by direct diagonalisation using the Lanczos method, and the results were rationalised using fourth-order perturbation theory.

The magnetic structures of $CaMnO_3$, $LaMnO_3$ and $La_{1/2}Ca_{1/2}MnO_3$ were successfully explained taking into account the orientation of the e_g orbitals

induced by a J-T distortion and the appropriate Mn-O hopping. The magnitudes of the exchange coupling were found to be strongly dependent on the hopping parameter t, varying as t^4 in fourth order perturbation theory. Different effects influencing the exchange were considered. The inclusion of the t_{2g} hopping, for example, produced an FM contribution that could be substantial for an Mn-O-Mn bonding angle θ far from 180°; in $CaMnO_3$ it could switch the sign of the exchange to ferromagnetic for $\theta \leq 132°$. The calculated exchange couplings were in good agreement with the experimental values. For $CaMnO_3$

$$J = 6.6 \text{ meV} \quad , \tag{1.34}$$

and for $LaMnO_3$

$$J_{\|} = -7.8 \text{ meV} \tag{1.35}$$

$$J_{\perp} = 2.6 \text{ meV}. \tag{1.36}$$

Exchange couplings were also calculated for $La_{1/2}Ca_{1/2}MnO_3$. For this compound there are no experimental values, only the sign of the interaction has been determined (see Table 1.2). The results found by Satpathy and collaborators agree with the signs of all interactions.

Chapter 2

Ab initio calculations of properties of periodic systems

In this chapter an overview is given of the main *ab initio* methods currently adopted for the determination of the electronic properties (i.e. those depending on the electronic structure) of a crystalline system [76, 77], with special attention to transition metal materials [78].

Ab initio calculations can provide the chemical and physical properties of a system given the chemical composition and the crystal structure. In principle there is no need for other *a priori* information; nevertheless some empirical notion can be used in practice and previous experience always turns out to be valuable in any new situation. Codes based on *ab initio* methods have been developed; they are able to return accurate results at a reasonable cost in computational time. The field is rapidly and constantly growing. The characteristics of a program that mainly appeal to solid state physicists and chemists are ease of use, simplicity of input, understandable output, good documentation. Speed of execution is, of course, another much sought-after property, especially in light of the bigger and bigger systems that theoreticians are willing to test. A little effort in terms of time and

study is needed in the beginning to acquire familiarity with such codes, but that turns out to always be a good investment because programs have now quite a long lifetime (ten years or even more) and upgrades (new versions) are issued regularly. *Ab initio* (or first principles, as they are often called) methods have played a prominent role in the last years, due to the availability of more and more powerful computers that can perform faster calculations and allow the theory to be tested on more realistic systems. Their success in the description of simple metals, semiconductors and organic materials is surprising.

Different approaches can be used in solid state physics and chemistry according to the kind of system being studied. It should be kept in mind that the main requirement for the wave function of the system is that it must be antisymmetric with respect to the interchange of both the space and spin coordinates of any two electrons (Pauli exclusion principle). In the special case of magnetic materials (the object of the present study) or of molecules with an odd number of electrons, one is dealing with properties that derive from unpaired electrons. There is the need to describe open shells, i.e. orbitals occupied by one electron only, as opposed to closed shells, which are doubly occupied.

The wave function for a single particle is called orbital. A spatial orbital $\psi_i(\mathbf{r})$ is a function of the position vector $\mathbf{r}$ and describes the spatial distribution of an electron. To take the spin into account, two orthonormal functions are used, $\alpha(\omega)$ (spin up) and $\beta(\omega)$ (spin down), which form a complete set. A spin orbital is the product of the space and spin part and is indicated by $\chi(\mathbf{x})$, where $\mathbf{x}$ stands for both the space and the spin coordinates. So from a spatial orbital one can form two different spin orbitals, one for spin up ($\chi(\mathbf{x}) = \psi_i(\mathbf{r})\alpha(\omega)$) and one for spin down ($\chi(\mathbf{x}) = \psi_i(\mathbf{r})\beta(\omega)$).

The computational schemes which are mainly used for *ab initio* calculations, and which are discussed in the present chapters, are the Hartree-Fock (HF), the Density Functional Theory (DFT) and the Configuration Interaction (CI).

2.1 One-electron Hamiltonian

The starting point for a theory is always to write down the complete Hamiltonian for the solid; it contains the kinetic energies of electrons and nuclei plus interaction terms between electrons and nuclei. The knowledge of such a Hamiltonian and of the number of electrons contains in itself all the necessary information about the electronic structure of the system, but, in order to be able to extract this information, a few simplifications are needed in the form of the Hamiltonian: the Born-Oppenheimer approximation is employed, and relativistic effects are neglected. So one is left with the time-independent, non-relativistic Shrödinger equation for the N-particle wave function of all the N electrons in the system, $\Psi(\mathbf{r}_1 s_1, \mathbf{r}_2 s_2 \ldots \mathbf{r}_N s_N)$, which depends on the spin s and the position $\mathbf{r}$; in atomic units, it is written as:

$$\sum_i \left(-\frac{1}{2}\nabla_i^2 - \sum_{\mathbf{R}} \frac{Z}{|\mathbf{r}_i - \mathbf{R}|} + \frac{1}{2}\sum_{j \neq i} \frac{1}{|\mathbf{r}_i - \mathbf{r}_j|} \right) \Psi = E\Psi \quad . \tag{2.1}$$

Here the first term is the electron kinetic energy, the second term is the electron-ion interaction V_{ei} (including contributions from all ionic positions $\mathbf{R}$), and the third is the electron-electron Coulomb repulsion.

It is this last term that makes eq. (2.1) notoriously not separable into N distinct electron problems. The Hartree-Fock approximation and the Density Functional Theory are two standard ways to proceed. They originate from two different points of view, but in both of them the result is that each electron moves independently in the field of all the others through the action

of an effective potential V_{eff} (mean field theory); this makes the Hamiltonian separable and the problem of N electrons reduces to N independent electrons problems. Eq. (2.1) can be re-written as

$$H = \sum_i \left(-\frac{1}{2}\nabla_i^2 + V_{\text{ei}}(\mathbf{r}_i) + V_{\text{eff}}(\mathbf{r}_i) \right) \quad . \tag{2.2}$$

The history of application of HF and DFT to solid state physics is long and well established; they have been applied to a variety of systems, in particular to semiconductors and insulators [79, 80, 81, 82, 83]. After many years of great success of DFT, in particular for the description of semiconductors and insulators, there has been recently a resurgence of popularity of the HF approximation among solid state scientists due to its success in the description of ground state properties of transition metal compounds, a field where results are much more reasonable compared to DFT. A good example could be the study of NiO and MnO, for which better agreement with experiment is achieved within HF theory [78, 84, 85]; or, similarly, the study of manganese perovskites, as described in the previous chapter.

The next two sections will briefly present the HF and DFT approaches to the solution of eq. (2.2). Then a description will also be given of the packages used for the calculations carried out in the present work.

2.2 The Hartree-Fock approximation

In the **Hartree-Fock** (HF) approach [86, 87, 88] one starts with an approximate description of the ground state wave function Ψ_0. This is done using a Slater determinant, which is an antisymmetrised product of N one-electron

spin orbitals (so it satisfies Pauli principle):

$$\Psi_0(\mathbf{r}_1 s_1, \mathbf{r}_2 s_2 \ldots \mathbf{r}_N s_N) = (N!)^{-1/2} \begin{vmatrix} \chi_1(\mathbf{x}_1) & \chi_1(\mathbf{x}_2) & \cdots & \chi_1(\mathbf{x}_N) \\ \chi_2(\mathbf{x}_1) & \chi_2(\mathbf{x}_2) & \cdots & \chi_2(\mathbf{x}_N) \\ \vdots & \vdots & & \vdots \\ \chi_N(\mathbf{x}_1) & \chi_N(\mathbf{x}_2) & \cdots & \chi_N(\mathbf{x}_N) \end{vmatrix} . \tag{2.3}$$

The factor $(N!)^{-1/2}$ ensures normalisation. It can actually be shown that the Slater determinant is the best single determinant approximation for Ψ_0 in a variational sense [89]. Minimisation of the quantity

$$\frac{< \Psi_0 | H | \Psi_0 >}{< \Psi_0 | \Psi_0 >}$$

with respect to the ψ_i (the spin dependence has been left out for brevity), leads to the set of Hartree-Fock equations:

$$\begin{aligned} &-\frac{1}{2}\nabla^2 \psi_i(\mathbf{r}) + V_{\rm ei}(\mathbf{r})\psi_i(\mathbf{r}) + V_{\rm Har}(\mathbf{r})\psi_i(\mathbf{r}) \\ &- \sum_j \int d\mathbf{r}' \frac{1}{|\mathbf{r} - \mathbf{r}'|} \psi_j^*(\mathbf{r}')\psi_i(\mathbf{r}')\psi_j(\mathbf{r}) = \epsilon_i \psi_i \end{aligned} \tag{2.4}$$

In this case $V_{\rm eff}$ (see eq. (2.2)) is the sum of two contributions. The first, $V_{\rm Har}$, is the classical (Hartree) electron-electron Coulomb interaction

$$V_{\rm Har}(\mathbf{r}_i) = -\int d\mathbf{r}' \rho(\mathbf{r}') \frac{1}{|\mathbf{r}_i - \mathbf{r}'|} \quad , \tag{2.5}$$

where

$$\rho(\mathbf{r}) = -\sum_i |\psi_i(\mathbf{r})|^2 \tag{2.6}$$

is the total electron density; the second is the explicit non-local exchange interaction. Then eq. (2.2) is solved with a Self Consistent Field (SCF) procedure. By definition, the only approximation is in the beginning, in the choice of the Slater determinant as a form for the ground state; apart from this, the method is exact.

The main limitation of the HF method is the fact that it neglects electron-electron correlation; by considering that each electron moves in an average field due to all the others, their repulsion is actually overestimated [90]. HF theory is also not suitable for the calculation of excited states which, in principle, correspond to energy values higher than the occupied ones. Koopman's theorem [77] gives a method to calculate approximate ionisation energies, but it assumes that the removal of one electron does't affect the other occupied orbitals. This lack of relaxation produces ionisation potentials which are too large; taking into account correlation effects (whose importance increases with the number of electrons) could fix in part this error. As a consequence, calculated band gaps, for example, are usually about twice the value from experiments. For insulators and semiconductors, though, band structures can easily be corrected using procedures such as the GW approximation [91]. The HF approximation gives very poor results when applied to metals, where correlation effects are essential for screening the r^{-1} dependence of the Coulomb interaction; as a result, the gap is too big and there is zero density of states at the Fermi level, which is, of course, in contrast with experimental evidence [92].

In the HF approximation each electron experiences the same mean field, so the self-interaction term arising from the Coulomb potential is exactly cancelled by a corresponding contribution from the exchange term (see eq. (2.4)). This is believed to be the main reason that makes HF more suitable for the description of the strongly correlated electron systems [78].

In the standard Hartree-Fock theory (also referred to as **Restricted Hartree-Fock** - RHF) each orbital is occupied by two electrons with opposite spin (closed shell system); in this case a single Slater determinant is enough for the description of the ground state wave function. When deal-

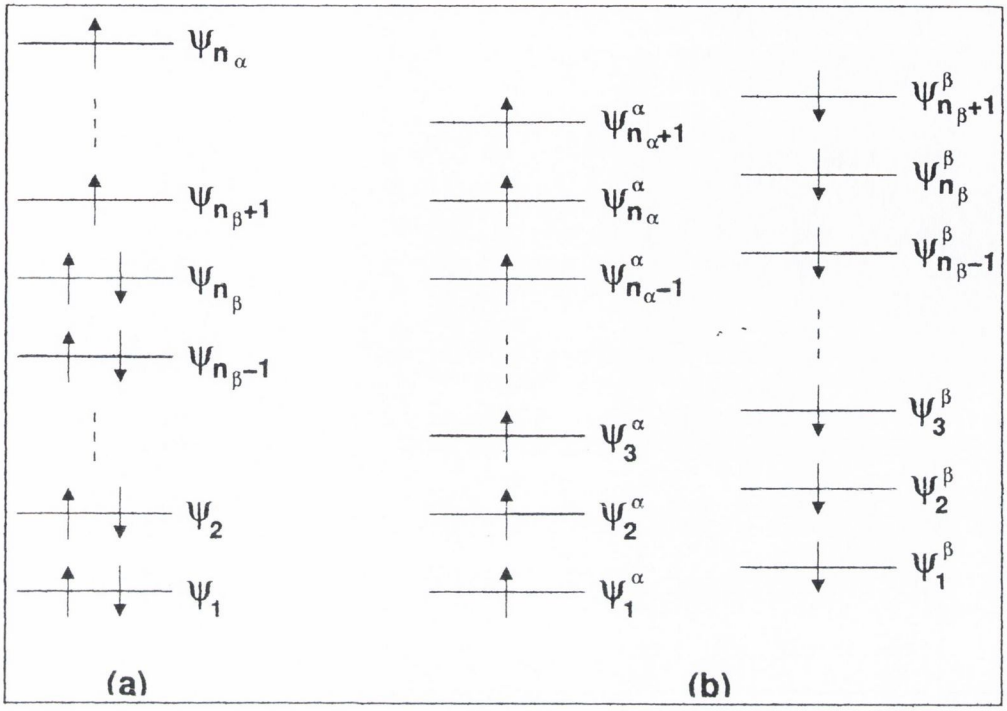

Figure 2.1: Definition of the molecular orbitals in the Restricted Hartree-Fock Open Shell (a) and Unrestricted Hartree-Fock (b) approximations [93, 112].

ng with open shell systems (e.g. magnetic systems), a single determinant is iot, in the most general case, an appropriate wave function; in order to get he correct spin eigenfunctions it is necessary to use a linear combination of Slater determinants [93].

There are two versions of the HF theory that make it suitable for the descryption of open shell sysytems. The **Restricted Hartree-Fock Open Shell** (ROHF) wave function is one choice and is, in general, a sum of Slater determinants. Each determinant contains a subset of closed shell (doubly occupied) orbitals and a subset of open shell (singly occupied) orbitals. In the special case of maximum spin (high spin case), nevertheless, a single determinant is still sufficient. Alternatively, the **Unrestricted Hartree-Fock** (UHF) approximation retains the mono-determinantal description by using

two separate sets of orbitals for spin up (α) and spin down (β) electrons (so there are no doubly occupied orbitals). Fig. 2.1 shows the molecular orbital diagrams corresponding to the ROHF and UHF definitions. Unlike ROHF, UHF wave functions are not eigenfunctions of the total spin operator S^2 because they are a mixture of spin states. For example, in the case of the H_2 molecule, the ROHF wave function is a singlet, whereas the UHF wave function is a combination of a singlet and a triplet. Dispite this limitation, UHF wave functions are energetically more stable and most of all allow solution with a local negative spin density (antiferromagnets), a feature that is not possessed by ROHF.

2.3 Density Functional Theory

The **Density Functional Theory** (DFT) approach is based on two theorems proposed by Hohenberg and Kohn [94] in 1964 and on a computational scheme implemented by Kohn and Sham [95] (K-S) the following year. The quantity used to describe the ground state Ψ_0 and the properties of the system is the one-electron density matrix

$$\begin{aligned} \rho(\mathbf{r},\mathbf{r}') &= N \int \ldots \int d\mathbf{r}_2 \ldots d\mathbf{r}_N \times [\Psi_0(\mathbf{r},\sigma_1;\mathbf{r}_2,\sigma_2;\ldots;\mathbf{r}_N,\sigma_N) \\ &\quad \Psi_0^*(\mathbf{r}',\sigma_1;\mathbf{r}_2,\sigma_2;\ldots;\mathbf{r}_N,\sigma_N)] \quad . \end{aligned} \tag{2.7}$$

V_{eff} contains, in this case, all information about many body interactions through the exchange and correlation potential which is, in turn, a universal functional of $\rho(\mathbf{r},\mathbf{r}')$ (i.e. it uniquely depends on the total charge density) [94].

Unlike HF, the aim of DFT is not to give an approximate form for Ψ_0, but to exactly calculate (in the limit of an exact exchange-correlation potential) the ground state energy E_0 and electron density. If the exact functional was

known, the self consistent solution of equation (2.2) would give the exact ground state density and energy; actually, it's analytic form is unknown and some approximations must be made, as will be explained in a moment. In this sense the wave function $\Psi_{K\text{-}S}$ which solves the equation is not the true Ψ_0, apart from the fact that it defines the same density; it only corresponds to a fictitious non-interacting system whose role is to parametrise the variation of energy with respect to the ground state densities [94]. For the same reason the eigenvalues ϵ_i of the Hamiltonian don't have the same physical meaning as those appearing in the HF equations (2.4) and should not be used to describe excitation energies (Koopman's theorem cannot be applied in this case).

Another thing to be noticed is that the electron-electron Coulomb interaction term includes a spurious contribution arising from the interaction of each electron with itself (self-interaction). It is not exactly cancelled by a corresponding exchange term of opposite sign, as in HF (see previous section), because of the approximate treatment of the exchange-correlation potential. Methods have been proposed for the inclusion of self-interaction corrections; see ref. [96] for a review.

As mentioned before, a few approximations have been proposed for the description of the exchange-correlation potential. Among these, the **Local Density Approximation** (LDA) [97, 98] has been very successful because it is quite accurate and computationally convenient. In general the exchange-correlation potential in $\mathbf{r}$ depends on $\rho(\mathbf{r}')$ ($\mathbf{r}' \neq \mathbf{r}$), so it is non-local. LDA assumes locality: $V_{\text{eff}}(\mathbf{r})$ only depends on the density in the same point $\mathbf{r}$. Such an assumption is justified when effects of spatial variations of the electron density may be neglected, so that the exchange-correlation potential is taken from the known results of electron systems with constant density (the

homogeneous electron gas.

Application of LDA to the study of strongly correlated systems encountered many difficulties because most of the results were not in agreement with experiment. For example, when applied to insulating, magnetically ordered compounds (for example NiO, MnO, NiS, $YBa_2Cu_3O_6$ and La_2CuO_4 [99, 100, 101]), a metallic, non-magnetic ground state was found.

Several improvements to LDA were proposed to get a better description ofthese materials. Among them, the **Local Spin Density Approximation** (LSDA) [102, 103] allows the description of open shell systems, in the same way as the UHF does in the framework of the HF approximation. LSDA introduces a spin dependence in the electron density, which splits into a density for spin up ($\rho_\uparrow(\mathbf{r})$) and a density for spin down ($\rho_\downarrow(\mathbf{r})$), to allow for possible spin-density waves or antiferromagnetic states. Following this approach, the presence of the gap at the Fermi level for MnO was correctly predicted [100], as well as the antiferromagnetic insulating behaviour of $LaMO_3$ (M = Cr, Mn, Fe, Ni) [55], but LSDA fails in many other contexts. Even in MnO the result is not completely satisfactory because the gap only opens as a consequence of the antiferromagnetic order, whereas the material is observed to be insulating also at temperatures well above the Néel temperature.

Another correction to LDA was proposed through the use of gradient corrected functionals in the so-called **Generalized Gradient Approximation** (GGA) [104, 105, 106, 107]. Simple LDA is too drastic in the sense that V_{eff} only depends on the local electron density; this is, of course, not true in strongly correlated materials, where the spatial dependence is very important. So LDA is can be seen as the zeroth order term in an expansion of the exact functional. GGA takes into account also terms in $\nabla\rho(\mathbf{r})$ in such an expansion. Results, once again, only show partial improvement compared

o LDA [108, 109].

Initially this failure was thought to originate from the independent electron approximation, i.e. from the fact that strongly correlated systems could not be described by band theory. Now it is acknowledged that this is not the case [78]. The main problem of LDA and its modifications is, as already mentioned, the approximate treatment of the exchange interaction that does not lead to a cancellation of the self-interaction in the Coulomb term; this unphysical effect causes LDA to work very poorly for strongly correlated materials. Ground state properties are better described within the framework of the HF approximation, which gives results in better agreement with experiments, for example in the case of manganese oxides [85] or manganites [38, 46, 110, 111].

Apart from the ground state, though, in general strongly correlated materials are not accurately described with a single determinant wave function. In order to include correlation effects and to be able to study excited states, a multi-determinantal approch is necessary. One of such approaches is the Configuration Interaction approximation, which has been used in this work and which will be introduced in a following section.

2.4 The CRYSTAL 98 package

The present section contains a brief description of the code that was used for the UHF calculations on $CaMnO_3$ and $LaMnO_3$ carried out in the present work and described in Chapter 3. They were performed using the commercial package CRYSTAL 98 [112, 113], which is an *ab initio* code for both HF and DFT treatment of periodic systems; it was developed jointly by the Dipartimento di Chimica Teorica - Università di Torino (Italy) and CCLRC (Council for the Central Laboratories of the Research Councils) - Daresbury

Laboratory (UK). CRYSTAL 98 has been used with success (together with its previous releases, in 1988, 1992 and 1995), on a huge variety of systems. For a full list of materials studied and bibliography the official CRYSTAL web sites at the University of Torino and at Daresbury Laboratory can be visited [80]. Here only the basics of its working principles will be outlined; for a complete documentation see refs. [112] and [113]. .

In any *ab initio* program the first step is the choice of the basis set that has to describe molecular orbitals. There are basically two different possibilities available: plane waves (PW) or Gaussian type orbitals (GTO). In CRYSTAL the latter choice is employed. Each crystalline orbital $\psi_i(\mathbf{r};\mathbf{k})$ is a linear combination of Bloch functions (with coefficients $a_{\mu,i}(\mathbf{k})$) $\phi_\mu(\mathbf{r};\mathbf{k})$, defined in terms of local functions (or atomic orbitals) $\varphi_\mu(\mathbf{r})$:

$$\psi_i(\mathbf{r};\mathbf{k}) = \sum_\mu a_{\mu,i}(\mathbf{k})\phi_\mu(\mathbf{r};\mathbf{k}) \tag{2.8}$$

$$\phi_\mu(\mathbf{r};\mathbf{k}) = \sum_{\mathbf{T}} \varphi_\mu(\mathbf{r} - \mathbf{A}_\mu - \mathbf{T})e^{i\mathbf{k}\cdot\mathbf{T}} \quad . \tag{2.9}$$

$\mathbf{A}_\mu$ is the coordinate of the nucleus, in the reference cell, on which φ_μ is centred; the $\sum_{\mathbf{T}}$ is extended to all lattice vectors $\mathbf{T}$. The atomic orbitals are expressed as linear combinations (contractions) of n_G individually normalized Gaussian type functions G with the same centre, with coefficients d_j and exponents α_j:

$$\varphi_\mu(\mathbf{r} - \mathbf{A}_\mu - \mathbf{T}) = \sum_j^{n_G} d_j G(\alpha_j; \mathbf{r} - \mathbf{A}_\mu - \mathbf{T}) \quad . \tag{2.10}$$

Compared to a PW basis, Gaussian orbitals allow the description of core and valence states with a limited number of basis function. On the other hand, there is a price to pay and this is loss of orthogonality, universality and the need for more sophisticated algorithms.

The Gaussian basis sets used for Ca, La, Mn and O were identical for both the bulk UHF and the cluster Configuration Interaction calculations

(performed with the GAMESS-UK package). They are slightly modified versions of those used in a HF study of $CaMnO_3$ [46] and of MnO and NiO [85]. For lanthanum, the basis set that was used is one optimised for the La^{3+} ion [1], modified in the exponents of the outer shells. A more detailed description of the basis sets will be given in Appendix.

CRYSTAL 98 carries out an SCF calculation until convergence on energy (or on eigenvalues) is reached. The theoretical description of the method used can be found in the CRYSTAL manual [112] or in the paper by Roetti [113].

The integration in reciprocal space plays a very important role, at each stage of the SCF procedure as well as, at convergence, for determining the Fermi energy and a number of other observable quantities. The integral evaluation is carried out over a specified portion of the BZ defined by a special net of inequivalent sampling points called the *Monkhorst net* [114]. Some details about the grid of k-points used in the present work is given in Appendix.

A feature of CRYSTAL largely exploited in the present work is that it allows the user to converge the SCF solution to the desired spin structure, making it possible to study spin polarised systems. Atoms in the crystallographic cell can be assigned either an up or a down spin, and the total magnetic moment can be locked to the desired value for some SCF cycle; such a choice for the initial guess ensures that the solution falls into a local minimum and converges. As a result, total energies can be calculated in the same crystal for different spin orientations and the nature of the magnetic ground state can be investigated.

CRYSTAL also allows the alteration of orbital occupation before the SCF

[1] This basis set is unpublished, but is available at http://www.tcm.phy.cam.uk/mdt26/crystal.html.

by shifting upward selected eigenvalues (the shift is then removed after the first cycle); this option artificially removes orbital degeneracy and can be used to converge the solution to some particular orbital occupation. In other words, it can be used to study orbital ordering in cases like $LaMnO_3$, where two e_g orbitals are available to be occupied by one electron.

Finally, there are many properties that CRYSTAL is able to calculate after convergence. The full list is available in the user's manual [112]. Among them it is worth mentioning the Mulliken population analysis, the band structure, the charge and spin density, the density of states; these are the main ones used to study the properties of the manganites in the present thesis.

2.5 Configuration Interaction

As seen in section 2.2, the HF approximation doesn't include any description of the correlation among electrons. The correlation energy is the difference between the exact (non relativistic) energy E of the system and the HF energy E_0 in the limit of a complete basis set:

$$E_{\text{corr}} = E - E_0 \quad . \tag{2.11}$$

The problem of electron correlation has been extensively dealt with in modern molecular quantum chemistry and many schemes have been developed to include it in the wave function of the system; they all use occupied and virtual orbitals as basic ingredients. Among such correlation schemes, **Configuration Interaction** (CI) is a very simple one, at least conceptually [121]. The use of the CI approximation is well established in theoretical quantum chemistry. A few examples of applications can be found in Chapter 4 of the book by Szabo and Oslund [77] and in the references cited in there. It has been recently applied to La_2CuO_4 [115, 116] and $KNiF_3$ [118] for the

calculation of exchange couplings.

The exact, non relativistic N-electron wave function Ψ can be expressed as a linear combination of Slater determinants ψ (trial basis functions). The matrix representation of the Hamiltonian in the chosen basis

$$H_{ij} =< \psi_i|H|\psi_j > \tag{2.12}$$

can then be diagonalised to find the eigenvalues. In principle, if the basis were complete (i.e. if all excited states of the system were included), one would obtain the exact energies not only for the ground state, but also for all the excited states. In practice, however, only a finite set of trial N-electron functions can be handled; consequently CI provides an upper limit to exact energies and good estimates of energy differences.

Given a set of 2n one-electron spin orbitals and N electrons (with $N \leq 2n$), there are $\begin{pmatrix} 2n \\ N \end{pmatrix}$ ways of forming an N-electron Slater determinant. Even for small molecules and limited basis sets, though, this is a huge number and, as already said, only a limited fraction of them can be handled. The determinantal trial wave functions can be constructed from the Hartree-Fock molecular orbitals; it is then natural to describe then by specifying how they differ from the HF wave function $|\Psi_0>$. This is formed using the N lowest energy spin orbitals; from them, one can construct all possible N-electron determinants which differ from $|\Psi_0>$ in having one excited orbital, then two and so on.

Defining $|\psi_a^r>$ as the singly excited determinant that differs from $|\Psi_0>$ in having the spin orbital χ_a replaced by χ_r, $|\psi_{ab}^{rs}>$ as the doubly excited determinant that differs from $|\Psi_0>$ in having the spin orbitals χ_a and χ_b replaced by χ_r and χ_s and so on, the expansion of the exact many-electron

wave function $|\Psi>$ is:

$$|\Psi> = c_0|\Psi_0> + \sum_{a,r} c_a^r|\psi_a^r> + \sum_{\substack{a<b \\ r<s}} c_{ab}^{rs}|\psi_{ab}^{rs}>$$

$$+ \sum_{\substack{a<b<c \\ r<s<t}} c_{abc}^{rst}|\psi_{abc}^{rst}> + \sum_{\substack{a<b<c<d \\ r<s<t<u}} c_{abcd}^{rstu}|\psi_{abcd}^{rstu}> + \ldots \quad . \tag{2.13}$$

The limitation to indices $a < b$, $r < s$ and so on ensures that double excitations are not counted twice. This is the form of the so-called **full CI matrix**. If $|\Psi_0>$ is a good approximation for the ground state of the system, one expects c_0 to be much greater than the other expansion coefficients.

A significant number of determinants is eliminated (although the number left is still too big) by considering that the matrix element between wave functions with a different number of α and β spins is zero.

The most general form of a CI wave function for N electrons with a particular total spin S in the active space is a linear combinations of spin adapted functions (SAFs)

$$\psi_{\rm CI} = \sum_i c_i \psi_i^{\rm SAF} \quad . \tag{2.14}$$

A SAF is the antisymmetrised product of a spatial orbital and a spin eigenfunction (SEF), Θ_a, for the specific spin state:

$$\psi_i^{\rm SAF} = A\left(\{\text{core}\}\phi_j\phi_k...\phi_s\phi_t\Theta_a\right) \quad , \tag{2.15}$$

where A is the antisymmetrising operator and {core} is the product of the doubly occupied orbitals in the core space. Each SEF consists of an orthonormal combination of products of the one-electron eigenspinors α and β, the primitive functions θ_i:

$$\Theta_a = \sum_i c_i\theta_i \quad . \tag{2.16}$$

SEFs are eigenfunctions of $\hat{S}^2$ and of $\hat{S}_z$ and can be generated in many different ways [77].

Using SAFs of specific $\hat{S}^2$ and $\hat{S}_z$ reduces the number of configurations because of the orthonormality of the primitive functions ($< \theta_i | \theta_j >= \delta_{ij}$).

As an example of SEFs, consider the case of six unpaired electrons; this is the situation arising when dealing with the three t_{2g} electrons on each of two neighbouring Mn ions in $CaMnO_3$. There are five SEFs if the six electrons are coupled into a singlet and one SEF if they are coupled into a septet state.

Denoting with 1 a spin up and with 0 a spin down, the five SEFs relative to the singlet state are:

$$\begin{array}{l} 101010 \\ 101100 \\ 110010 \\ 110100 \\ 111000 \ . \end{array} \qquad (2.17)$$

For the case in question there are twenty possible primitive functions; theorems exist that allow the calculation of the coefficients of eq.(2.16) [119].

Apart from the determinants eliminated on the basis of the above considerations about spin, there are others which do not appear in the full CI expansion matrix. First of all there is no coupling between the HF ground state and singly excited states (Brillouin's theorem [120]); because matrix elements between Slater determinants which differ by more than two spin orbitals are zero [77], there is also no coupling between the ground states and triple or quadruple excitations, nor between singles and quadruples and so on. Denoting, in a symbolic form, with $|S>$ all the terms of eq. (2.13) involving singly excited states, with $|D>$ all the doubly excited and so on,

the block structure of the full CI matrix (which is Hermitian) looks like the following:

$$\begin{bmatrix} < \Psi_0|\mathcal{H}|\Psi_0 > & 0 & < \psi_0|\mathcal{H}|D > & 0 & 0 & \dots \\ & < S|\mathcal{H}|S > & < S|\mathcal{H}|D > & < S|\mathcal{H}|T > & 0 & \dots \\ & & < D|\mathcal{H}|D > & < D|\mathcal{H}|T > & < D|\mathcal{H}|Q > & \dots \\ & & & < T|\mathcal{H}|T > & < T|\mathcal{H}|Q > & \dots \\ & & & & < Q|\mathcal{H}|Q > & \dots \\ & & & & & \vdots \end{bmatrix} \tag{2.18}$$

The fact that single excitations don't couple with $|\psi_0>$ doesn't mean there is no interaction between them at all: they mix indirectly via double excitations because they both couple to them.

With the exception of small molecules, even with a minimal basis set, there are so many possible spin adapted configurations that full CI becomes computationally impracticable. The CI expansion needs to be truncated somehow, for example by considering only a limited number of possible excitations; this will result, of course, in an approximate treatment of correlation, with the error getting bigger for systems with a larger number of electrons.

The simplest of such truncations is achieved by taking into account only single and double excitations from the ground state and is generally referred to as **Singles and Doubles Configuration Interaction** (SDCI) approximation; it is described by taking only the first two terms the sum (2.13). CI calculations on manganites clusters carried out in the present work (see Chapter 4), make use of the SDCI approximation as implemented in the GAMESS-UK package described in the next section.

2.6 The GAMESS-UK package

GAMESS-UK [122] is an *ab initio* electronic structure program that allows the HF, DFT and Multi-Configuration Self Consistent Field (MCSCF) treat-

ment of molecules and clusters. It also includes the possibility of performing a variety of post-SCF calculations. It has been developed with the contribution of many authors.

Molecular orbitals are described, in the same way as in CRYSTAL, by Gaussian type functions; s, p, d, f and g shells can be used. After the SCF calculation, the user has many available tools for the analysis of the wave function. Among them, for example, there is the determination of the orbital and atomic charges using both Mulliken and Distributed Multipole Analyses, together with a graphical analysis of the wave function by the calculation of charge densities, molecular orbitals, atom difference densities and electrostatic potentials on a grid of points. Another feature is the localisation of orbitals using the Foster-Boys algorithm [123].

Among the post-SCF modules, a few CI schemes, based on different approaches, can be used. Conventional Table CI [124] and Direct CI [125, 126] are the main ones. They are both multi-reference schemes i.e. more then one configuration can be given as reference in the input; then all possible single and double excitations from them are taken into account for the construction of the CI wave function. The difference between the Table CI and the Direct CI formulations is that in the former the Hamiltonian matrix elements for one pair of configurations are calculated at a time (configuration-driven), while in the latter the integrals over the one-electron basis functions are examined in sequence to determine Hamiltonian matrix elements to which they contribute (integral-driven).

For the CI calculations on $CaMnO_3$ and $LaMnO_3$ clusters described later in Chapter 4, the Direct CI approximation has been used. The main advantage of Direct CI is in the fact that one can avoid the explicit construction of the CI Hamiltonian matrix; instead, directly from the list of transformed

nolecular integrals, a matrix times vector multiplication is performed

$$\mathbf{Z} = \mathbf{HC} \quad , \tag{2.19}$$

vhere $\mathbf{C}$ is a trial column of CI expansion coefficients.

The N-electron antisymmetrised SEFs are constructed from molecular or-)itals which are partitioned into an internal (normally occupied orbitals) and ın external space (normally unoccupied in the ground state); lower indices ıre assigned to internal MOs and higher indices to external MOs.

The Direct CI scheme in GAMESS makes use of the Yamanouchi-Kotani YK) genealogical spin functions [127], the coupling order being such that ıigher indexed MOs are coupled before lower indexed MOs. Then spin functions are ordered following a particular convention. This will be clarified with ı specific example. Consider five singly occupied MOs coupled to a doublet total spin 1/2); then there are five possible spin functions [77]. If 1 and 0 are ısed to represent spin up and spin down respectively, proceeding from the owest indexed singly occupied MO (left), write down the appropriate digits or all the spin functions. The resulting binary number defines the way they ıre ordered:

- 10101: Spin function 1
- 10110: Spin function 2
- 11001: Spin function 3
- 11010: Spin function 4
- 11100: Spin function 5.

Single and double excitations are generated with the requirement that ı maximum of two electrons can be allowed to occupy the external space.

The number of generated configurations can be quite large even if the CI process is limited to single and double excitations; a selection procedure is applied by calculating the coupling of each configuration with the reference ones and discarding those that lie below a certain threshold. According to the occupation and spin pattern found in the external space, the spin functions are placed in four states: *vacuum* states, with no electrons in the external space, *doublet* states, with one electron in the external space, *singlet* and *triplet* states, with two electrons in the external space, appropriately spin coupled.

Chapter 3

UHF calculations on $CaMnO_3$ and $LaMnO_3$

In this chapter the first part of the work done, i.e. the Unrestricted Hartree-Fock study of $CaMnO_3$ and $LaMnO_3$, is reported. The UHF approximation, as implemented in the CRYSTAL package, has been used to investigate the magnetic properties of these compounds, in particular the nature of the ground state (and its relationship with the structural symmetry) and the value of the exchange coupling constants.

For $CaMnO_3$, only the experimentally observed cubic structure has been studied. The correct ground state is found; results are in agreement with the Goodenough model, which is able to explain the relative energies of the different spin ordered structures. The calculated value of J, though, is larger then the experimental estimate [20, 68].

In the case of $LaMnO_3$, there is a need for a deeper understanding of the relationship between magnetism, structure and orbital ordering. Calculations in the present study have been first carried out on an idealised cubic crystal; these identify independent spin and orbital ordering contributions to the Hamiltonian. Then the experimental *Pnma* structure was analysed, as well as a cubic structure in which simple Jahn-Teller distortions are present; lattice

parameters and atomic positions have been optimised for $LaMnO_3$ in the *Pnma* structure. Experimental distortions are found to be very important for a correct description of the magnetic ground state; calculated exchange couplings reproduce the correct A-type AF behaviour of $LaMnO_3$, though their value is below the ones reported from experiments.

3.1 $CaMnO_3$

As described in Chapter 1, $CaMnO_3$ is experimentally found to be in the cubic ideal perovskite structure (Fig. 1.1) with a lattice constant $a = 3.73$ Å; its ground state is the AF G-type structure and the Néel temperature is $T_N = 110$ K. For this UHF study, two sets of calculations have been carried out, at lattice constants equal to 3.73 Å and 3.75 Å, for the FM and for the A, C and G AF spin orderings. Relative energies and magnetic moments (from Mulliken population analysis[1]) are summarised in Table 3.1, which also reports other calculations from the literature [46, 44], together with the experimental estimate of the magnetic moment [20]. The lowest energy was found for the G-AF at 3.73 Å, which is 24.3 meV below the corresponding G structure at 3.75 Å.

Mulliken populations had very similar values in all calculated structures and lattice constants; Table 3.2 shows charge values for the lowest energy G-type AF at $a = 3.73$ Å. It should be noticed that, unlike Ca which is practically 2+, charges on Mn and O are quite different from the nominal values. The detailed output of the Mulliken population from the CRYSTAL program, for both alpha+beta (charge) and alpha-beta (spin) electrons, is given in the Appendix as a reference. Though the Mulliken analysis only gives

[1]The magnetic moment, in this case, only includes the spin contribution; taking into account the orbital part might, of course, bring some minor correction to its value.

	Magn. ordering	Rel. energy (meV/Mn ion)	Magn. moment (μ_B/Mn)
Present work, a = 3.73 Å	FM	0	3.16
	A-AF	-23.6	3.18
	C-AF	-45.1	3.18
	G-AF	-64.3	3.23
Present work, a = 3.75 Å	FM	0	3.19
	A-AF	-22.2	3.21
	C-AF	-42.4	3.23
	G-AF	-60.6	3.25
UHF [46]	FM	0	3.17
	G-AF	-66.0	3.25
LSDA [44]	FM	0	2.81
	A-AF	-57	2.72
	G-AF	-116	2.48
Experiment [20]			2.65

Table 3.1: Summary of UHF results for $CaMnO_3$; relative energies from UHF calculations (in meV/Mn ion) and magnetic moments from Mulliken population analysis (in μ_B/Mn) are shown for two lattice constants. Also shown are other UHF and LSDA calculations and the experimental value of the magnetic moment.

an approximation for the orbital and atomic populations, some conclusions are still possible using a semicovalent model based on Goodenough prescriptions. Oxygen, with its charge equal to -1.33, is missing 0.67 electrons in the valence orbitals (which would allow it to reach the nominal charge of -2); on the other hand, Mn has an excess charge of 1.87 electrons, that partially populate the two (nominally empty) e_g orbitals (see Appendix). Manganese has six empty hybrids available for semicovalent bonding, each for any of the six neighbouring oxygens; so each O has transferred 0.33 electrons on each

ion	tot. charge	ionic charge	Mn $3d$ population		
Ca^{2+}	18.14	+1.86	t_{2g}	e_g	total
Mn^{4+}	22.87	+2.13	3.29	1.41	4.70
O^{2-}	9.33	-1.33			

Table 3.2: Calculated charge values (in e) for $CaMnO_3$ from Mulliken population analysis; details of the Mn $3d$ populations are also shown.

side to an Mn ion[2] and this roughly adds up to the total excess charge on Mn. An evidence of the fact that there is a good degree of covalency can be found in the overlap Mulliken population (also reported in the Appendix). It shows that the only appreciable overlap is between Mn and O and involves 0.074 electrons.

In spite of having almost five electrons in the d orbitals (see Table 3.2 and Appendix), i.e. of being a nearly 2+ ion, the magnetic moment on the manganese is close to the expected 3 μ_B. The detailed alpha-beta population analysis shows that the magnetic moment mainly comes from the t_{2g} electrons (2.79 μ_B) and that the e_g orbitals contribute much less to it (0.40 μ_B); this is because an Mn ion receives, by symmetry, electrons of opposite spin from the two sides in the O-Mn-O chain.

As a comparison for UHF energies, it is worth presenting some results (see Table 3.3) obtained within the Local Spin Density Approximation (LSDA) to Density Functional Theory (DFT); in particular the calculations made use of the von Barth-Hedin [102] form for the exchange and correlation potential. Even if both UHF and LSDA predict the correct magnetic ground state, energy differences between the various spin structures in the latter case turn out to be much bigger then the corresponding UHF ones. Because exchange

[2]Looking at the oxygen p_x, p_y and p_z orbital population in details, what actually happens is that the charge is mainly missing from the orbital which points toward the Mn ion.

Magn. ordering	Rel. energy (meV/Mn ion)	Magn. moment (μ_B/Mn)
FM	0	2.54
C-AF	-180.2	2.41
G-AF	-231.4	2.40

Table 3.3: DFT results for $CaMnO_3$; relative energies and magnetic moments from Mulliken population analysis (in μ_B/Mn) are shown for $a = 3.75$ Å.

couplings are calculated from energy differences, they will also be larger (and as noticed above, UHF already overestimates them). This is in agreement with what is generally believed, i.e. that the HF approximation is more appropriate then DFT for a description of the ground state of transition metal compounds.

3.1.1 $CaMnO_3$ and Goodenough's model

Goodenough's model [67], the first successful attempt to describe in a systematic way the relationship between exchange coupling and crystallographic structure in manganites, gives the correct predictions in the case of $CaMnO_3$. In that model, because Mn ions are 4+ ions, there is always a hybrid orbital available to be shared with a O^{2-}; as a consequence, all interactions can be of type I (see Fig. 1.10). The resulting structure is cubic, as the Mn-Mn separations are all the same, and the AF G-type structure is the ground state.

The model has been applied to explain the relative energies of the A-AF, G-AF and FM spin orderings in $CaMnO_3$ and $LaMnO_3$ in the idealised perovskite cubic structure [110]. Using a simplified argument in which it was assumed that an empty e_g orbital is either available or not, it was found that the relative energies of these magnetic structures can be explained by

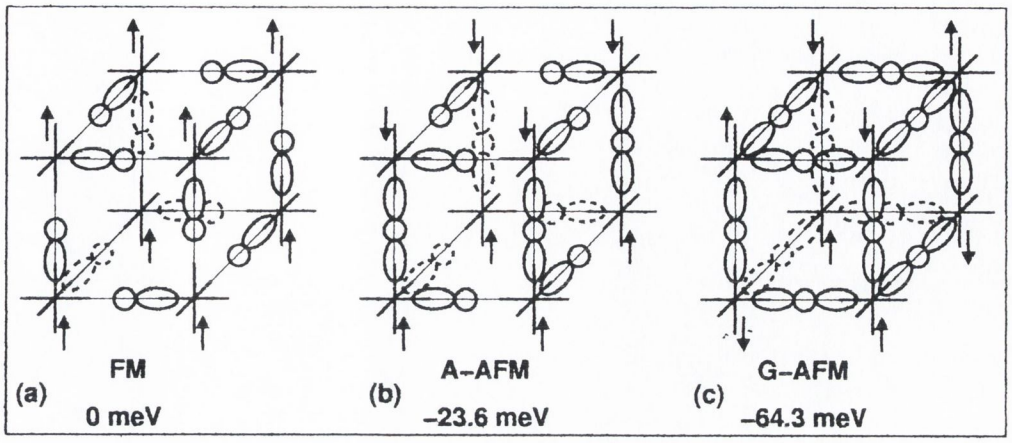

Figure 3.1: Covalent exchange structures in $CaMnO_3$ derived from the Good-enough model (see Fig. 1.10). $a = 3.73$ Å.

counting the numbers of each type of interaction in each magnetic state and then calculating the relative energy of each type of interaction. Fig. 3.1(a) shows empty Mn hybrids and spin orientations appropriate for 6 type II interactions per Mn^{4+} ion in FM $CaMnO_3$. When layered AF coupling of spins is introduced (fig. 3.1(b)) the total energy is lowered by 23.6 meV per formula unit. In this case there are 2 type I and 4 type II interactions per Mn ion. In the G-AF structure (fig. 3.1(c)) each Mn spin is surrounded by 6 neighbours with opposite spin and the number of type I interactions is maximised to 6 per Mn ion. The relative energy is -64.3 meV. From these results it can be estimated that type I interactions are ~20 meV lower in energy than type II interactions in $CaMnO_3$ with the cubic perovskite structure [110].

3.1.2 Exchange coupling; Heisenberg and Ising Hamiltonians

Calculated energy differences can be used to derive the exchange coupling J for $CaMnO_3$; this has been done by mapping these differences onto a simple

Hamiltonian. It has been specified earlier that the form used is the one of equation (1.14); a few comments are needed at this point to clarify the validity of such a mapping and the comparison with results by other authors and from experiments.

The type of package used for the present calculations only allows two possible values for the atomic spin (up or down), so that the scalar product is either 1 or -1. What is actually done, then, is to map energy differences on an **Ising** rather than on a Heisenberg Hamiltonian (the latter takes into account all spin orientations through the scalar product $\hat{\mathbf{S}}_i \cdot \hat{\mathbf{S}}_j$). Equation (1.14) has to be re-written as

$$\mathcal{H} = \sum_{<ij>} J_{ij} \frac{\hat{\mathbf{S}}_{z_i} \cdot \hat{\mathbf{S}}_{z_j}}{S^2} \quad , \tag{3.1}$$

where $\hat{\mathbf{S}}_{z_i}$ is the z component of the i-th atom.

On the other hand, experimental values for J are always derived using the Rushbrook-Wood approximation (eq. (1.18)) [68], which is a fitting formula based on the Heisenberg Hamiltonian. The question about how to relate J values calculated using Ising and Heisenberg Hamiltonians can be addressed by finding a formula to fit Ising data. Such data can be found in a paper by Butera and Comi [117] who study an Ising model using high temperature expansions. In this way it is possible to derive kT_c/J values and compare them to the fit by Rushbrook and Wood. Table 3.4 shows the fit for three different spins and also gives the Ising/Heisenberg ratio; the Ising values (third column) have been converted to Heisenberg units multiplying by $4s^2$.

In the case of $CaMnO_3$ (s=3/2) Table 3.4 shows that J calculated using an Ising Hamiltonian will be 2.32 times smaller than the one calculated with a Heisenberg Hamiltonian.

s	kT_c/J Heisenberg	kT_c/J Ising	Ising/Heisenberg ratio
1/2	1.81	4.51	2.49
1	5.43	12.76	2.34
3/2	10.49	24.39	2.32

Table 3.4: Comparison between Heisenberg and Ising Hamiltonians for three liffferent values of the spin s. The second column is the Rushbrook-Wood approximation [68], the third is based on data by Butera and Comi [117].

Having discussed this point, it is possible to turn to the calculation of J. With three relative energies available (see Table 3.1), exchange interactions up to the third nearest neighbour can be calculated. Denoting with J_1, J_2 and J_3 the interactions in the cubic lattice corresponding to the interatomic vectors $[a,0,0]$, $[a,a,0]$ and $[a,a,a]$, the three equations for their determination are:

$$E_{FM} - E_{A-AF} = \frac{1}{2}(4J_1 + 16J_2 + 16J_3) \tag{3.2}$$

$$E_{FM} - E_{C-AF} = \frac{1}{2}(8J_1 + 16J_2) \tag{3.3}$$

$$E_{FM} - E_{G-AF} = \frac{1}{2}(12J_1 + 13J_3)\,. \tag{3.4}$$

Solving them, J_1, J_2 and J_3 turn out to be

$$\begin{aligned} J_1 &= 10.7 \text{ meV} \\ J_2 &= 0.3 \text{ meV} \\ J_3 &= 0.0 \text{ meV} \ , \end{aligned} \tag{3.5}$$

for $a = 3.73$ Å, and

$$\begin{aligned} J_1 &= 10.1 \text{ meV} \\ J_2 &= 0.2 \text{ meV} \\ J_3 &= 0.0 \text{ meV} \ , \end{aligned} \tag{3.6}$$

for $a = 3.75$ Å.

The above values clearly show how interactions further than the nearest neighbour ones fall to zero very rapidly. It is impossible, in the present calculation, to check (as is generally believed) whether exchange interactions connecting magnetic ions along a linear chain are stronger then the ones which don't (like $[a, 0, 0]$); this is because interactions along, for example, $[2a, 0, 0]$, contribute equally to the four spin structure and cancel out in energy differences.

The experimental value for J, estimated from $T_N = 110$ K [20] using the Rushbrook-Wood approximation (eq. (1.18)), is 6.6 meV. According to what has been said before about Ising and Heisenberg Hamiltonians, with the same T_N the Ising value for J estimated from experiment will be smaller by a factor of 2.32 (see Table 3.4), i.e. it will be 2.84 meV. In their theoretical work Satpathy and collaborators [75] report the same calculated J of 6.6 meV[3]; Millis [73] estimates $J = 10$ K, i.e 7.8 meV. There is good agreement between our calculated value and the one from ref. [75], though ours is slightly overestimated.

If, for comparison, the calculation of J is repeated in the LDA case, it is found that

$$\begin{aligned} J_1 &= 38.6 \text{ meV} \\ J_2 &= 3.2 \text{ meV}. \end{aligned}$$

Such values are much bigger then the corresponding UHF ones, and this is again an indication of the fact that LDA proves less adequate for describing these type of systems.

[3]Due to the different definition used in that work, the difference between a pair of ferro and antiferromagnetically coupled Mn ions is twice the exchange energy defined in eq. 1.14. Hence their values have to be divided by 2 in order to compare them to the present work.

3.1.3 Band structures and hybrid DFT theory

Band structures of $CaMnO_3$ have been reported by several groups, both in the LSDA [44, 45] and in the UHF [46] approximation; some of them have been discussed in the previous chapter.

The main difference between the two approaches is that UHF overestimates the gap. This can be seen from the band structure plotted below for $CaMnO_3$ in the ground state G-AF structure (Fig. 3.2). Comparison with FIG. 4 in ref. [44], an LSDA calculation, clearly shows such a difference: the calculated gap is 0.015 Hartree in LSDA and about 0.36 Hartree in the present UHF case.

The density of states projected on O 2p and Mn t_{2g} and e_g orbitals is reported in Fig. 3.3. From both the band structure and the density of states a narrow Mn t_{2g} band can be observed around -0.73 Hartree; above that, a wider oxygen $2p$ band extends from -0.6 Hartree up to the Fermi level. This is a characteristic generally found in the HF approximation [58]. At the bottom of the conduction band, Mn e_g and t_{2g} bands can be observed around 0.1 and 0.25 Hartree respectively. The occupied t_{2g} band is consistent with the calculated moment of 3.25 μ_B, i.e. coming, as expected, mainly from t_{2g} electrons.

As an intermediate step between pure HF and pure DFT, it is possible to implement a DFT scheme that includes a certain percentage of exact Hartree-Fock exchange. Such a theory has been successfully applied to La_2CuO_4 by Martin and Illas [116], who used an hybrid exchange potential containing an equal mixture of the exact HF exchange and of the Dirac-Slater LDA exchange [128]; the correlation potential was the Vosko-Wilk-Nusair parametrisation of the Ceperley-Alder free electron-gas correlation results [129].

Exploiting a feature of CRYSTAL 98, that allows the use of hybrid

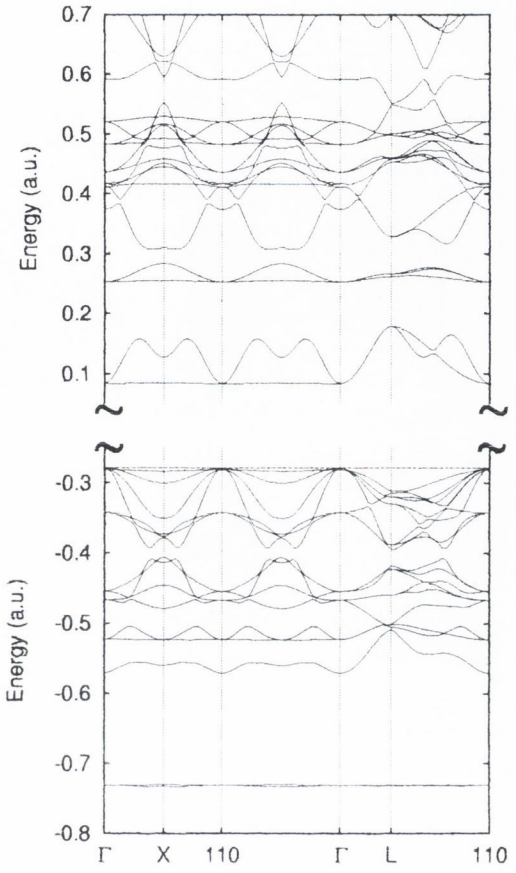

Figure 3.2: Band structure of $CaMnO_3$ in the G-AF spin structure - UHF calculation. The Fermi energy is indicated by a dashed line.

exchange-correlation potentials, a similar kind of calculation has been carried out on the G-AF ground state of $CaMnO_3$, using the same 50% mixture of HF and LDA exchange and the same correlation potential as in ref. [116]. Fig. 3.4 and Fig. 3.5 show the new band structure and density of states following this hybrid choice. The main thing to note is the reduction of the gap, which is now about 0.15 Hartree; this is half the pure HF one, indicating an approximately linear scaling with the percentage of HF exchange. The other difference with the previous pure HF band structure is that now Mn

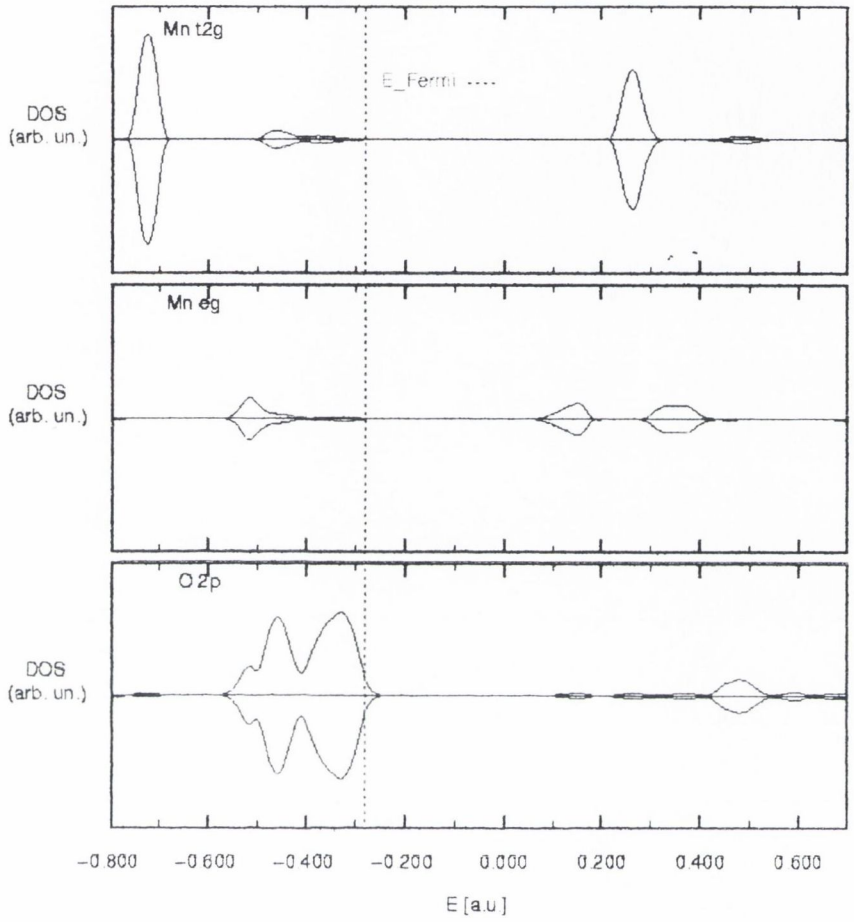

Figure 3.3: Projected density of states for the G-AF structure of $CaMnO_3$ from a UHF calculation.

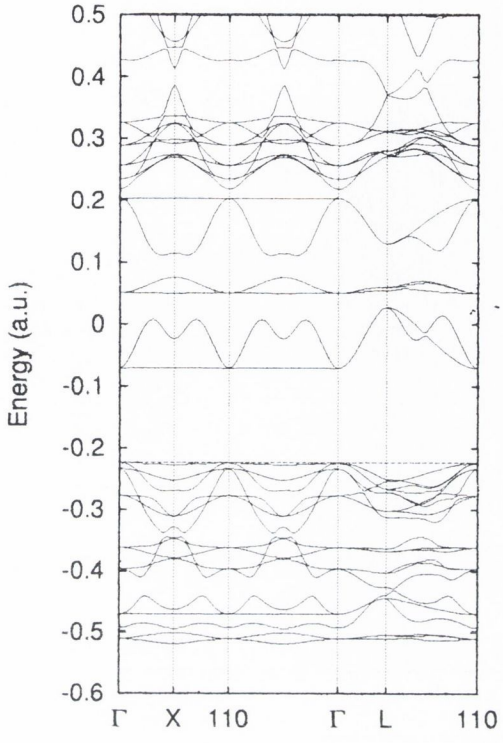

Figure 3.4: Band structure of $CaMnO_3$ in the G-AF spin structure - hybrid DFT calculation. The Fermi energy is indicated by a dashed line.

t_{2g} bands start to hybridise with the oxygen and move closer to the oxygen bands at around -0.5 Hartree. The charge from Mulliken population analysis, in this case, is +1.81 for Mn and -1.2 for O, to show that indeed more hybridisation is present.

Finally, the energy differences between the FM and the G-AF structures in the hybrid DFT case has been evaluated; the G-AF structure is below the FM one by 202.2 meV, which results in an exchange coupling $J = 33.7$ meV. This value is closer to the experimental estimate (6.6 meV) then the one calculated in the LSDA approximation (38.6 meV); both of them, anyway, are much higher the the HF value (10.7 meV).

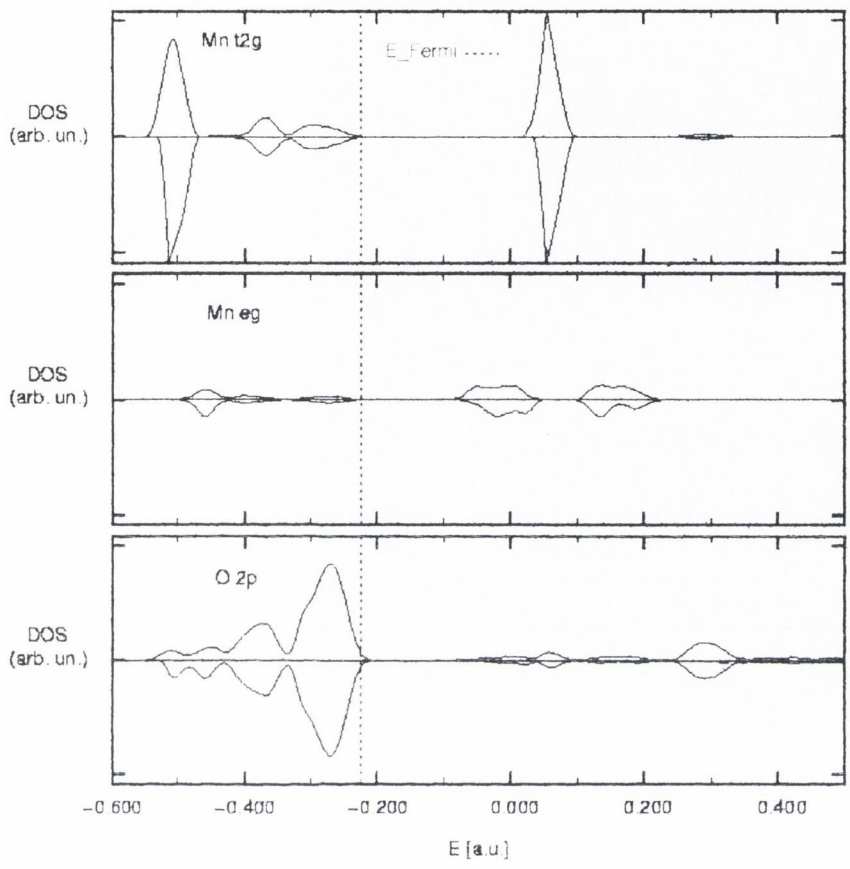

Figure 3.5: Density of states for $CaMnO_3$ in the G-AF structure from an hybrid DFT calculation.

3.2 $LaMnO_3$

In $LaMnO_3$ the situation changes and, as was remarked before, becomes more complicated due to the presence of an extra electron that populates an e_g orbital in the $3d$ shell. The compound is experimentally observed in the distorted (orthorhombic) *Pnma* structure [47] and is an A-type AF [20]. Configuration Interaction (CI) cluster calculations are needed to provide detailed information on exchange coupling between neighbouring Mn ions; nevertheless, in the case of $LaMnO_3$, UHF calculations are helpful for a study of orbital ordering in this compound. Obviously one can expect that exchange constants will depend on orbital ordering: the latter determines which orbital is empty and therefore available for exchange coupling. What is not known is whether there is a relationship between the e_g charge density for a particular orbital ordering and the spin ordering.

A series of calculations in the (ideal) cubic perovskite structure shows that a Hamiltonian with independent exchange and orbital ordering terms describes total energies of $LaMnO_3$ with different spin and orbital ordering accurately. An optimised *Pnma* structure shows the correct ground state, as well as the correct sign for the exchange constants; it is almost isoenergetic with a cubic perovskite structure with a 5% J-T distortion. This is described in more detail in the following sections.

3.2.1 Cubic idealised structure

Results of calculations where a cubic unit cell is used are presented first. The most important feature found is that the solution of the SCF calculation converges to different orbital occupancies starting with different initial conditions.

The CRYSTAL package allows the choice of the initial guess for orbital

ccupancy, so that the system which is being studied can be converged to he desired final state. Using this technique, total energy calculations on ubic $LaMnO_3$ with different spin and orbital ordering have been performed. The extra electron can populate any of the two e_g orbitals ($d_{3z^2-r^2}$ or $d_{x^2-y^2}$) n the $3d$ shell. Using a doubled cubic perovskite unit, containing two Mn toms, the occupied e_g orbitals can be chosen to be the same or to be different. It is important to stress here the fact that in the distorted *Pnma* tructure occupied orbitals are not pure $d_{3z^2-r^2}$ or $d_{x^2-y^2}$ but linear combinations of them taking different orientations in space; nevertheless a study of rbital ordering in an idealised cubic $LaMnO_3$ can be useful in order to get a letter understanding of the mechanisms determining the exchange coupling properties of this compound.

A cubic unit cell with the same volume as the experimental structure (60.88 $Å^3$ [47]) has a lattice constant $a = 3.934$ Å. This was optimised by Patterson [111] through total energy minimization (using the ferromagnetic spin ordering in the experimental orbital ordering) and the calculated minimum energy lattice constant, $a = 3.953$ Å, for a volume of 61.77 $Å^3$, is dose to the experimental one in the 'cubic' phase of $LaMnO_3$ (3.947 Å) that ccurrs at temperatures above 750 K [54]. Such an optimised structure lies about 10 mev below the $a = 3.934$ Å one. An analysis of total energies in the different spin and orbital orderings shows that they can be well fitted by a Hamiltonian of the form

$$\mathcal{H} = \sum_{<ij>} J_{ij} \frac{\hat{\mathbf{S}}_{z_i} \cdot \hat{\mathbf{S}}_{z_j}}{S^2} + H_{OO} \quad , \tag{3.7}$$

where H_{OO} is the orbital ordering term, i.e. a term depending on orbital ordering only.

In Table 3.5 relative energies and magnetic moments (from Mulliken population analysis) are reported for $a = 3.934$.

Spin and Orbital ordering	Relative Energy (meV/Mn ion)	Magnetic moment (μ_B/Mn ion)
FM $d_{x^2-y^2}/d_{x^2-y^2}$	0.00	3.88
FM $d_{3z^2-r^2}/d_{3z^2-r^2}$	-6.1	3.88
A-AF $d_{x^2-y^2}/d_{x^2-y^2}$	-14.4	3.90
G-AF $d_{3z^2-r^2}/d_{3z^2-r^2}$	-34.0	3.88
A-AF $d_{3z^2-r^2}/d_{3z^2-r^2}$	-34.4	3.87
G-AF $d_{x^2-y^2}/d_{x^2-y^2}$	-34.9	3.88
A-AF $d_{3z^2-r^2}/d_{x^2-y^2}$	-40.23	3.89
G-AF $d_{3z^2-r^2}/d_{x^2-y^2}$	-95.4	3.89
FM $d_{3z^2-r^2}/d_{x^2-y^2}$	-131.5	3.88

Table 3.5: Relative energies and magnetic moments (from Mulliken population analysis) for cubic $LaMnO_3$ with different spin and orbital orderings. Lattice constant is 3.934 Å.

These calculations must, of course, be carried out in a doubled unit cell; in this way one is able to assign a different spin (and/or a different e_g orbital occupancy) to the two Mn ions in the cell. In the A-type AF the cell is doubled along the [001] direction, in the G-type it is doubled along the [110], [101] and [110] directions. For an FM spin ordering any doubling of the cell is equivalent (same total energy), but orbital ordering removes this degeneracy. If the aim is to look at the $d_{3z^2-r^2}/d_{x^2-y^2}$ orbital ordering, the cell must be doubled in a G-type way, to ensure that the orbital of one species is surrounded by six orbital of the other species; A-AF $d_{3z^2-r^2}/d_{x^2-y^2}$ orbital ordering is not compatible with the corresponding unit cell doubling and cannot be used to determine H_{OO}.

For $d_{3z^2-r^2}/d_{3z^2-r^2}$ and $d_{x^2-y^2}/d_{x^2-y^2}$ orbital orderings two distinct exchange constants are postulated, one in the xy plane ($J_{||}$) and one along the direction perpendicular to that plane ($J_{\perp}$); for $d_{3z^2-r^2}/d_{x^2-y^2}$ only a single exchange constant ($J_{||} = J_{\perp}$) is postulated. Then, first, energy differences between different spin structures and same orbital ordering can be used to

Orbital ordering	$J_{\|}$ (meV)	$J_{\perp}$ (meV)
$d_{3z^2-r^2}/d_{3z^2-r^2}$	-0.1	14.2
$d_{x^2-y^2}/d_{x^2-y^2}$	5.1	7.2
$d_{3z^2-r^2}/d_{x^2-y^2}$	-6.0	-6.0

Table 3.6: Exchange constants in cubic $LaMnO_3$ for various orbital orderings. $J_{\|}$ couples Mn ions in the xy plane, $J_{\perp}$ those along a direction perpendicular to the xy plane.

calculate exchange coupling constants for each orbital ordering; they are listed in table 3.6.

Once the exchange couplings have been calculated for each orbital ordering, relative energies of the same orbital but different spin orderings can be used to calculate the H_{OO} terms in eq. (3.7). Their values will depend on the energy chosen as a reference; taking for this purpose the energy of the FM structure in the $d_{x^2-y^2}/d_{x^2-y^2}$ ordering (just as in table 3.5) it is found that

$$\begin{aligned} H_{d_{3z^2-r^2}/d_{3z^2-r^2}} &= -20.1 \text{ meV} \\ H_{d_{x^2-y^2}/d_{x^2-y^2}} &= -17.4 \text{ meV} \\ H_{d_{3z^2-r^2}/d_{x^2-y^2}} &= -113.5 \text{ meV}. \end{aligned}$$

When these values for H_{OO} are substituted back in eq. (3.7), relative energies for the spin and orbital ordering considered agree very well with the values reported in table 3.5 (the maximum discrepancy is less then 0.2 meV), confirming the suitability of the Hamiltonian.

For each spin structure and orbital ordering charge density difference plots have been obtained. A charge density difference plot is a plot of the difference in charge density between the UHF wave functions of the bulk solid and the one from the isolated ions, using the same basis set in both cases. It allows visualisation of orbital ordering as well as charge displacements in the

crystal. In order to achieve this, instead of subtracting the charge density of an isolated Mn^{3+} ion, it is more suitable to subtract the charge density of an Mn^{4+} ion; in this way the extra e_g electron can be clearly observed. Such plots were almost identical for different spin orderings and only changed when orbital ordering changed, again indicating that independent spin and orbital ordering components contribute to total energies in cubic $LaMnO_3$; they are shown in fig. 3.6. By looking at fig. 3.6 and table 3.6 it can be noticed that a positive, antiferromagnetic exchange occurs whenever two identical orbitals are found side by side (with the exception of the small $J_{||} = -0.1$ meV in the $d_{3z^2-r^2}/d_{3z^2-r^2}$ ordering); a negative, ferromagnetic exchange occurs, on the other hand, when the two orbitals are different. This is a characteristic that will be found in the *Pnma* symmetry as well, and is actually a property of the real material. Distortions of the oxygen charge are also related to the type of exchange that occurs between the manganese ions. In the lower panel of fig. 3.6 ($d_{3z^2-r^2}/d_{x^2-y^2}$ ordering) there is an evident build-up of charge on the oxygen in the direction of negative value contour lines of a neighbouring manganese; such a distortion occurs even if the oxygen is exactly in the center of the Mn-Mn distance and results in FM ($J < 0$) coupling. It should also be noted that there is relatively little distortion in the O charge density in fig. 3.6(b) along the z direction, where a large AF coupling is present.

The main conclusion now, having presented the results of cubic $LaMnO_3$ calculations, is that spin and orbital ordering contributions to the Hamiltonian are independent. Different final states are found, depending on the orbital occupancy in the initial guess. It was already pointed out that when two neighbouring electrons in the crystal occupy e_g orbitals corresponding to the same combination of $d_{3z^2-r^2}$ and $d_{x^2-y^2}$, an AF coupling is established between them; when alternated combinations of orbitals are present the cou-

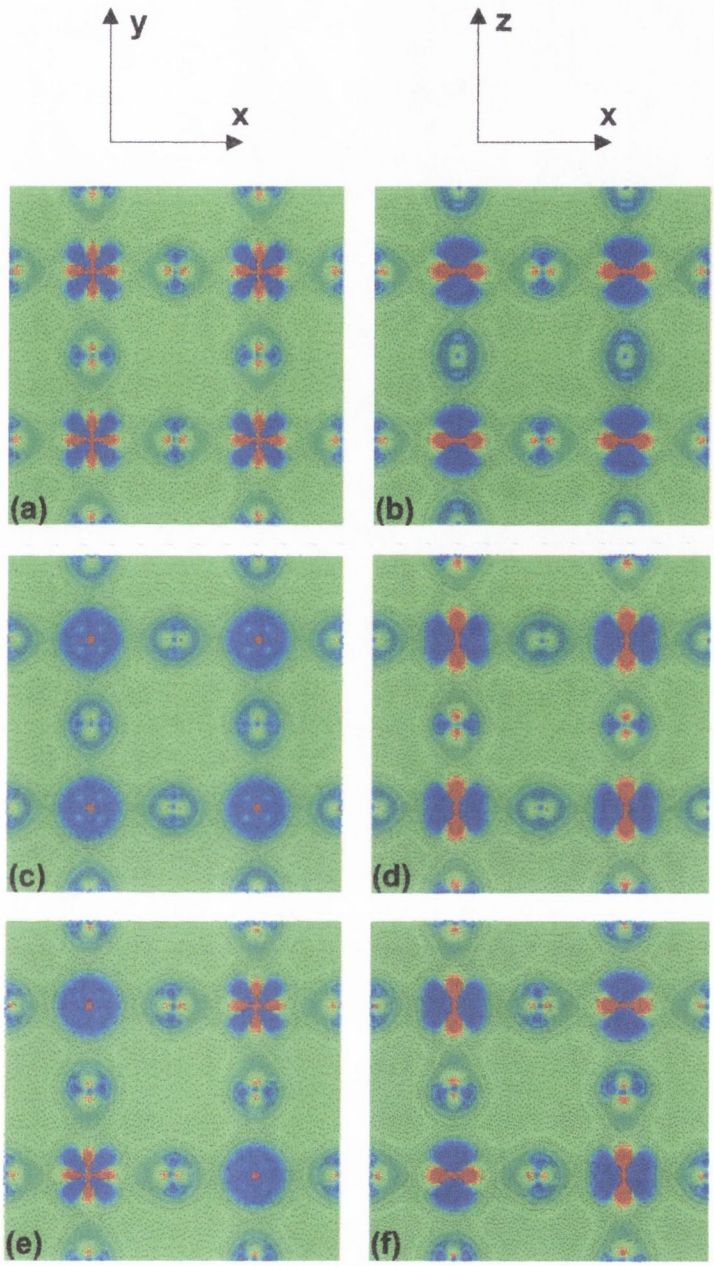

Figure 3.6: Charge density difference plots for cubic $LaMnO_3$ in the xy (left) and xz (right) plane. Orbital ordering is $d_{3z^2-r^2}/d_{3z^2-r^2}$ ((a),(b)), $d_{x^2-y^2}/d_{x^2-y^2}$ ((c),(d)) and $d_{3z^2-r^2}/d_{x^2-y^2}$ ((e),(f)). The difference in charge densities is between the UHF density for the bulk solid and the UHF density for isolated Mn^{4+} and O^{2-} ions. Blue, red and green lines represent positive, negative and zero values respectively.

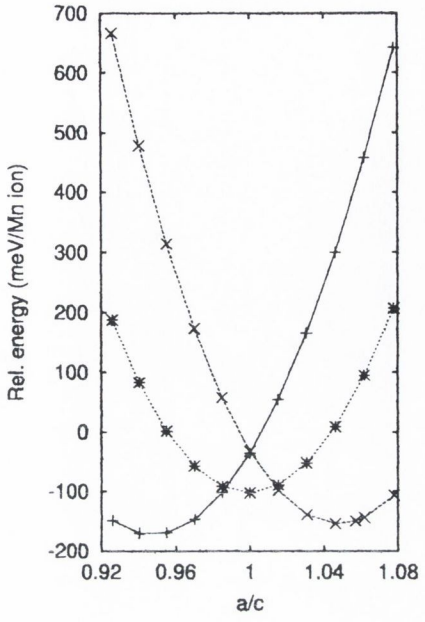

Figure 3.7: Plot of relative energies as a function of the ratio between lattice constants a and c for the tetragonal $LaMnO_3$ in the G-AFM structure. The constant volume corresponds to that of a cube with edge $a = 3.953$ Å. Orbital ordering is $d_{3z^2-r^2}/d_{3z^2-r^2}$ (solid), $d_{x^2-y^2}/d_{x^2-y^2}$ (dashed) and $d_{3z^2-r^2}/d_{x^2-y^2}$ (dotted). Reference energy is the same as in table 3.5.

pling is ferromagnetic. In this way energy differences within a particular spin structure can be explained even in the case of a distorted lattice.

3.2.2 Tetragonal $LaMnO_3$

The relationship between orbital ordering and crystal symmetry has been explored further. In the G-AF structure, the total energy was calculated as a function of tetragonal distortion. A tetragonal distortion is a modification of the cubic lattice such that either $a = b < c$ or $a = b > c$ (P4/mmm space group); the volume was kept constant 61.77 Å^3, corresponding to one of the minimum energy cubic structure.

Fig. 3.7 shows the results at various orbital occupancies. It can be

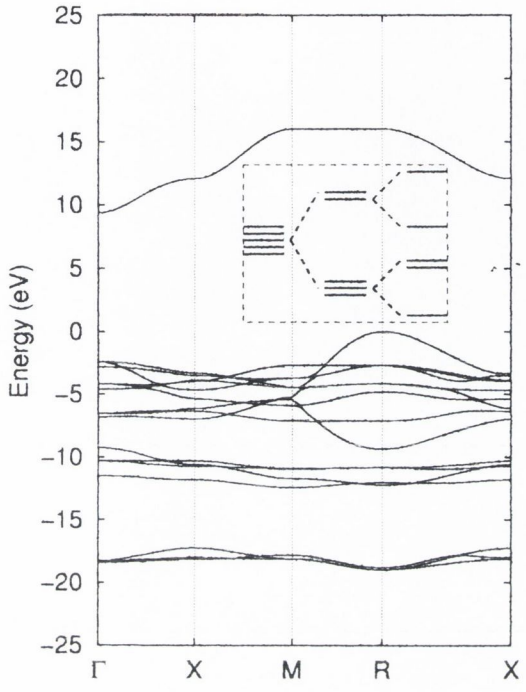

Figure 3.8: UHF majority spin band structure of tetragonally distorted $LaMnO_3$ with FM spin ordering. Mn^{3+} occupied d bands are clustered around -10 eV and the unoccupied d band is around +10 eV at the Γ point. Inset shows the splitting of the five degenerate d levels into a t_{2g} + e_g set in a octahedral environment and further splitting following a tetragonal distortion.

observed that the $d_{3z^2-r^2}/d_{x^2-y^2}$ orbital ordering is the most stable for a narrow region around the cubic structure ($a/c = 1$); otherwise the stability switches to $d_{3z^2-r^2}/d_{3z^2-r^2}$ for $a < c$ and to $d_{x^2-y^2}/d_{x^2-y^2}$ for $a > c$. In other words, the preferred e_g orbitals are always oriented along the direction where the elongation takes place in the tetragonal modification. So it looks like the explanation could be simply electrostatic: the orbitals try to avoid each other in order to minimize Coulomb repulsion.

The most stable energy, as seen from fig. 3.7, occurs for an a/c ratio

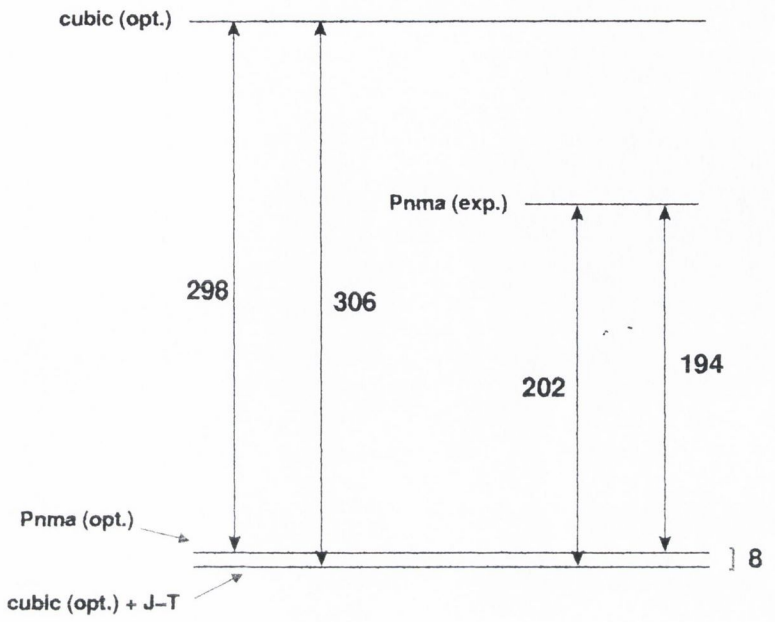

Figure 3.9: Summary (in scale) of relative energies (in meV/Mn ion) for FM $LaMnO_3$ in the various structures studied.

around 0.94; that energy, at least for the G-AF structure, is about 160 meV below the reference energy. It will be shortly shown that such an energy lowering is, anyway, smaller than the one that is obtained with a J-T distortion or when the energy minimised *Pnma* structure is used.

A band structure calculation in tetragonal $LaMnO_3$ can also show the reduction of orbital degeneracy when the cubic symmetry is broken. Fig. 3.8 shows the FM majority spin band structure of $LaMnO_3$ with tetragonal symmetry; as expected, four levels are filled and one level is unfilled. The splitting of the five degenerate levels is the same as the one described in Fig. 1.5 for tetragonal symmetry breaking.

3.2.3 J-T distorted and *Pnma* structure

The study of cubic $LaMnO_3$ has given, as a result, some insight into the relationship between structure and orbital ordering. Because of the cubic symmetry, all Mn-O-Mn distances being the same, $d_{3z^2-r^2}$ and $d_{x^2-y^2}$ orbitals are equivalent in principle. Forcing occupancy to follow a particular pattern produces the consequences described above and it can be learned how magnetic exchange is related to orbital ordering.

The experimental structure of $LaMnO_3$ is of distorted *Pnma* symmetry; the magnetic ordering is antiferromagnetic of A-type. Structural parameters determined by neutron diffraction [47] were shown in table 1.1. Such parameters have been optimised by energy minimization in the A-FM spin ordering; all seven internal parameters (the ones not fixed by symmetry) were optimised, as well as the three lattice constants. The resulting structure is 194 meV below the experimental one and 298 meV below the optimised cubic structure. A calculation has also been performed using the optimised cubic structure to which a simple in-plane 5% J-T distortion has been added (see fig. 1.9); this structure is almost isoenergetic with the optimised *Pnma* (it is, more exactly, 8 meV below). Fig. 3.9 displays these energy differences in a schematic way; Table 3.7 contains lattice parameters used in the calculations (experimental ones are presented as well for comparison).

It is worth analysing in more detail the main changes that take place when going from the experimental to the optimised *Pnma* structure. The volume is increased from 60.88 to 62.53 $Å^3$, i.e by 2.7% (the volume of the lowest energy cubic structure is 61.77$Å^3$). The a lattice vector is practically unchanged, whereas b and c increase by 1.1 and 1.6% respectively. Mn-O and La-O distances change as well; they are reported in table 3.8.

The first thing to notice is that the extent of the J-T distortion is reduced

		x/a	y/b	z/c
Experimental [47]	La	0.549	0.250	0.010
$a = 5.742$ Å	Mn	0.000	0.000	0.000
$b = 7.668$ Å	O_I	-0.014	0.250	-0.070
$c = 5.532$ Å	O_{II}	0.309	0.039	0.224
Optimised	La	0.517	0.250	0.001
$a = 5.740$ Å	Mn	0.000	0.000	0.000
$b = 7.754$ Å	O_I	-0.002	0.250	-0.027
$c = 5.620$ Å	O_{II}	0.290	0.014	0.237
Jahn-Teller	La	0.500	0.250	0.000
$a = 5.590$ Å	Mn	0.000	0.000	0.000
$b = 7.905$ Å	O_I	0.000	0.250	0.000
$c = 5.590$ Å	O_{II}	0.2625	0.000	0.2625

Table 3.7: Structural parameters for J-T distorted and *Pnma* $LaMnO_3$.

in the optimised *Pnma* structure: the ratio between the long and the short Mn-O in-plane bonds goes from 1.15 to 1.12. Then the Mn-O distance shrinks as well. The La-O distances, on the other hand, increase significantly. In other words lower energy is found in the case of smaller distortions and larger La-O distances. The sum of the La^{3+} and O^{2-} ionic radii [130] is 2.76 Å. La-O distances in the optimised *Pnma* structure are just below this value, whereas the experimental distances are much smaller.

Relative energies for *Pnma* and J-T distorted $LaMnO_3$ are reported in table 3.9, as well as the calculated magnetic moment.

Charge values from Mulliken population analysis are given in Table 3.10. As can be seen, the compound is more ionic compared to $CaMnO_3$, with the actual charges being closer to their nominal values. In the same way as in $CaMnO_3$, the detailed output of the UHF Mulliken population analysis (reported in the Appendix) can help understanding the ionic charge in terms of semicovalent bonds between Mn and O. Mn is, again, a nearly 2+ ion, with almost five electrons in the $3d$ orbital. This time each manganese only has

	Mn-O	La-O
cubic (opt.)	1.976	2.795
Pnma (exp.)	1.903	2.433
	1.957	2.461
	2.185	2.548
Pnma (opt.)	1.910	2.609
	1.944	2.666
	2.135	2.684
cubic (opt.) + J-T	1.877	2.795
	1.976	2.797
	2.075	

Table 3.8: Mn-O and La-O distances (in Å) in $LaMnO_3$.

four empty hybrids available for accepting electrons from the oxygens, which form the pattern shown earlier in Fig. 1.12. Oxygen can transfer charge to Mn on both sides along the vertical AF direction and on one side only in the FM plane; this explains why O_I is missing more charge (0.25 electrons) than O_{II} (0.18 electrons). Mn has an extra 0.76 electrons, 0.66 of which in the $3d$ shell; this is more or less the number obtained if one takes into account the charge tranferred from the four oxygens that can form a bonding with it. Regarding the magnetic moment, this is close to the expected 4 μ_B; in particular a contribution of 2.56 μ_B comes from t_{2g} orbitals and a contribution of 1.37 μ_B comes from e_g orbitals. The overlap population analysis shows, first of all, that the degree of semicovalency is much less than in $CaMnO_3$ (as stated before, $LaMnO_3$ is more ionic). Then it also shows that the largest overlap (0.030 electrons) is found between Mn and the oxygen which has the shortest bonding distance in the plane.

Now exchange couplings can be calculated from energy differences; as usual $J_{\parallel}$ and $J_{\perp}$ represent the coupling in the plane (a/c in *Pnma*) and along the vertical distance (b axis). The calculated values for the *Pnma* structure,

Spin and Orbital ordering	Relative Energy (meV/Mn ion)	Magnetic moment (μ_B/Mn Ion)
Pnma (exp.) FM	0.0	4.00
Pnma (exp.) A-FM	-1.2	4.00
Pnma (exp.) G-FM	13.9	3.96
Pnma (opt.) FM	0.0	4.00
Pnma (opt.) A-FM	-2.0	3.96
Pnma (opt.) G-FM	21.9	3.94
J-T FM	0.0	4.00
J-T A-FM	1.1	3.98
J-T G-FM	33.6	-

Table 3.9: Relative energies and magnetic moments for *Pnma* and J-T distorted $LaMnO_3$.

using both the experimental lattice parameters and the optimised ones, and for the J-T distorted structure, are listed in Table 3.11, where they are also compared to the experimental values (from neutron scattering data) and to other calculations found in the literature. The experimental estimates are based on a Heisenberg Hamiltonian. In order to get the corresponding estimates from an Ising Hamiltonian, it can be observed that in Table 3.4 the Ising/Heisenberg ratio is nearly converged at 2.32 for $s = 3/2$, so it is reasonable to assume the same ratio for $s = 2$. Such a factor brings the experimental values for $J_\perp$ and $J_{||}$ to 2.0 and -2.9 meV respectively.

ion	tot. charge	ionic charge	Mn 3*d* population		
La^{3+}	53.85	+3.15	t_{2g}	e_g	total
Mn^{3+}	22.76	+2.24	2.94	1.72	4.66
O_I^{2-}	9.75	-1.75			
O_{II}^{2-}	9.82	-1.82			

Table 3.10: Calculated charge values (in e) for $LaMnO_3$ in the *Pnma* structure from Mulliken population analysis. O_I and O_{II} are vertical and in-plane oxygens respectively. Details of the Mn 3*d* populations are also shown.

	$J_\perp$ (meV)	$J_\parallel$ (meV)
Pnma (exp.)	0.6	-3.7
Pnma (opt.)	1.0	-6.0
cubic (opt.) + J-T	-0.6	-8.1
UHF *Pnma* (exp.) [58]	0.8	-3.5
LSDA *Pnma* (exp.)[72]	-3.1	-9.1
Model Hamiltonian [75]	2.6	-7.8
Experiment [69]	4.6	-6.6
Experiment [71]	4.8	-6.7

Table 3.11: Calculated exchange couplings for *Pnma* and J-T distorted structures; results reported by other authors are also shown, together with experimental values.

The Js that were obtained using the optimised *Pnma* structure have the correct sign but they are underestimated; in particular $J_\perp$ is very different from the experimental value. The structure with the 5% J-T distortion, though lower in energy, gives a very small ferromagnetic value for $J_\perp$ (this is because the A-AF is slightly above the FM spin ordering).

The relationship between exchange coupling and orbital ordering can be analysed with the help of charge density difference plots. In fig. 3.10 they are reported for the J-T distorted $LaMnO_3$. The plots are very similar in the *Pnma* case, but an advantage of the J-T distorted structure is that oxygen and manganese atoms lie in the same plane and are more easily visualised. First of all it can be noticed that only orbitals of one symmetry alternate in the x-y plane; they are $d_{3x^2-r^2}$ and $d_{3y^2-r^2}$ and they are oriented along the longest Mn-O distance. Again, as in fig. 3.6, the oxygen charge is distorted, now toward the closest manganese. This gives a FM coupling in the plane. Along the vertical direction (z axis in fig. 3.10(b)) orbitals are oriented in the same way and the coupling is AF. It should also be pointed out that it is possible to recognise in fig. 3.10(a) and (b) the same pattern of orbitals

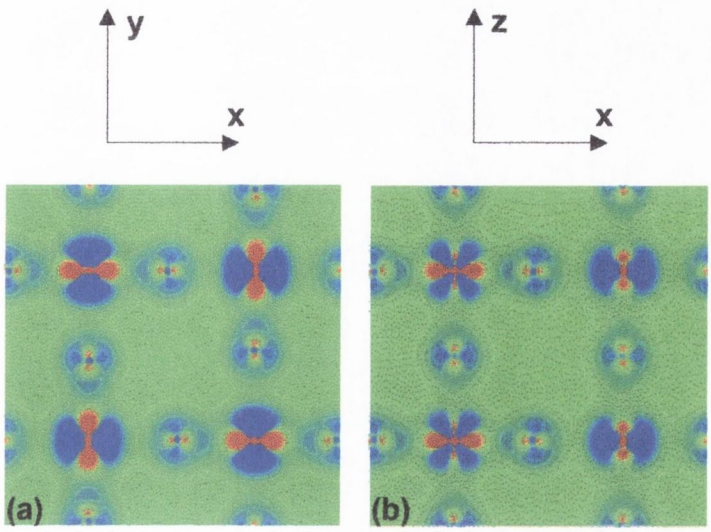

Figure 3.10: Charge density difference plots for J-T distorted $LaMnO_3$ in the xy (a) and xz (b) plane. Orbital ordering is $d_{3x^2-r^2}/d_{3y^2-r^2}$ in (a), whereas in (b) orbitals of the same type order along the z axis. The difference in charge densities is between the UHF density for the bulk solid and the UHF density for isolated Mn^{4+} and O^{2-} ions. Blue, red and green lines represent positive, negative and zero values respectively.

that were schematically drawn in Fig. 1.11 (C) and (D) respectively.

3.2.4 Band structures and hybrid DFT theory

As in $CaMnO_3$, band structures have been plotted in the UHF approximation and in an hybrid DFT theory containing 50% of exact Hartree-Fock exchange.

Figs. 3.11 and 3.12 show the band structure and the projected density of states for the A-type AF $LaMnO_3$ in the optimised *Pnma* structure. Mn t_{2g} and e_g form a band that extends for about half a Hartree and is centred around 0.52 Hartree; eight bands are occupied, which is consistent with the calculated magnetic of 3.96 μ_B. Such a band is again below the wide oxigen band. Above the Fermi level, bands are a mixture of Mn t_{2g} and e_g.

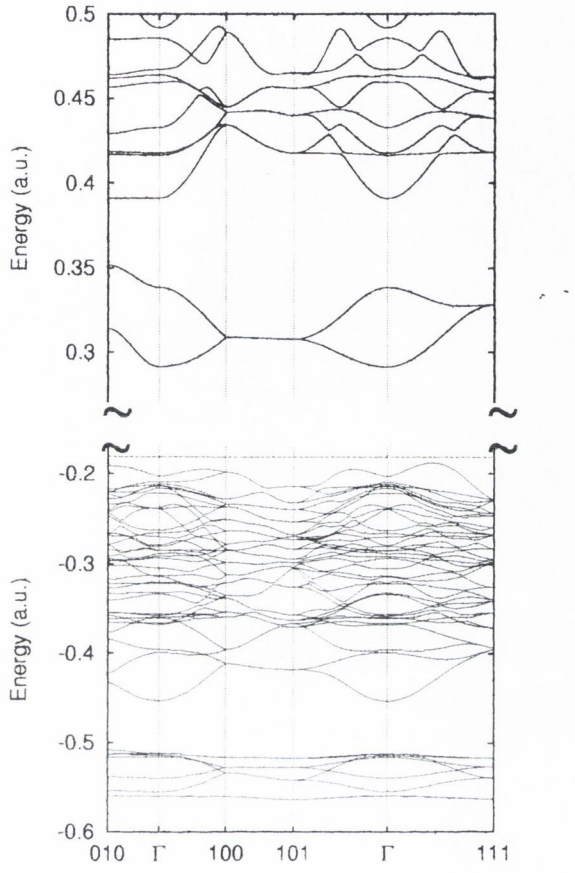

Figure 3.11: Band structure of *Pnma* $LaMnO_3$ in the A-AF spin structure - UHF calculation. The Fermi energy is indicated by a dashed line.

The corresponding plots in the case of the hybrid DFT theory are shown in Figs. 3.13 and 3.14. The gap is reduced from about 0.5 Hartree to about 0.2 Hartree when the hybrid exchange potential is used. Such a value is still much bigger than the 0.026 Hartree reported from pure LSDA calculations [44].

In the Hybrid DFT case, energy differences between the various spin structures become larger, and, as a consequence, exchange interactions become larger as well. Using the optimised *Pnma* structure, the G-AF structure

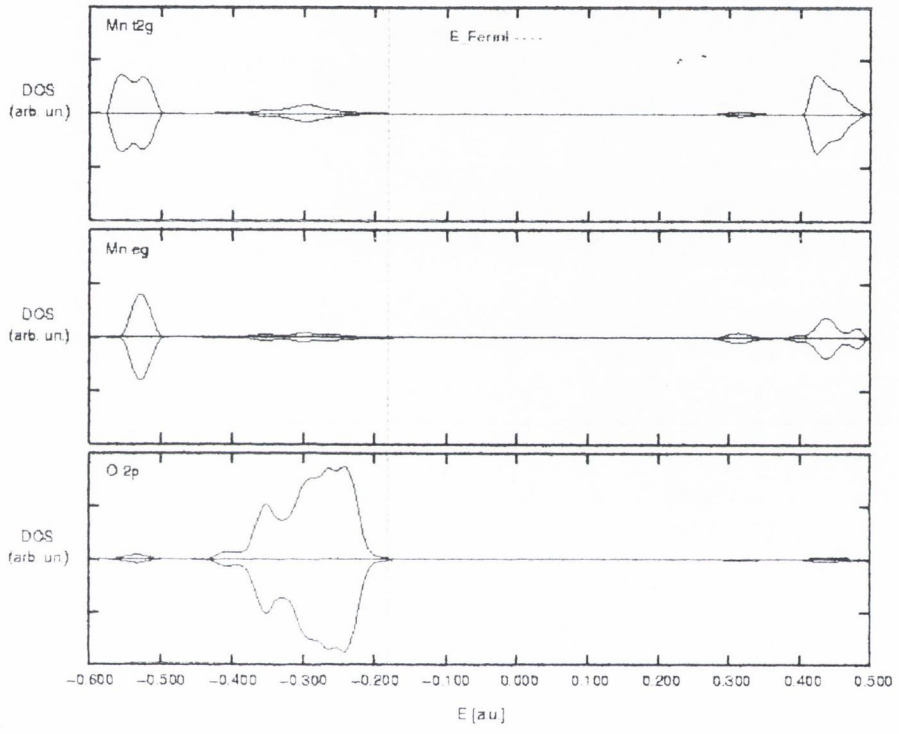

Figure 3.12: Density of states for $LaMnO_3$ in the A-AF structure from UHF calculations. The Fermi energy is indicated by a dashed line. Energies are in Hartree.

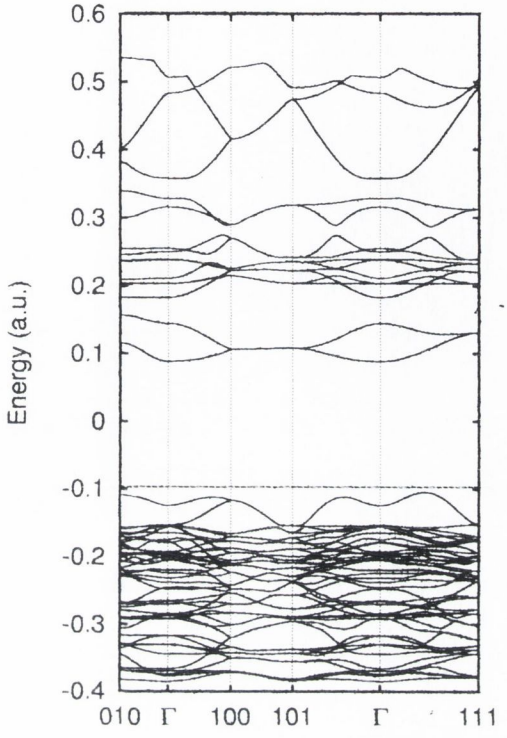

Figure 3.13: Band structure of *Pnma* $LaMnO_3$ in the A-AF spin structure - hybrid DFT calculation. The Fermi energy is indicated by a dashed line.

is above the reference FM energy by 43.0 meV, while the A-FM is 6.7 meV below the same reference energy. The resulting exchange couplings are, then,

$$J_{\perp} = 3.3 \text{ meV}$$

$$J_{\parallel} = -12.4\text{meV}.$$

Comparison of these values with the ones reported in Table 3.11, shows that they are actually about three times larger then those calculated in the UHF approximation on the same crystal structure (first line of Table 3.11).

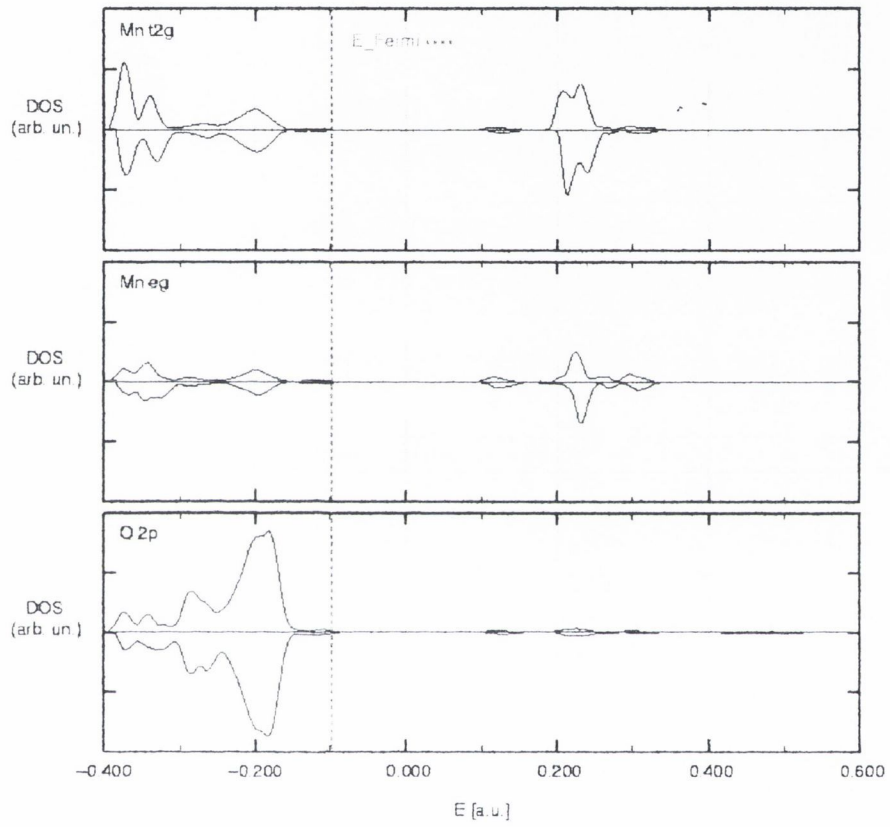

Figure 3.14: Hybrid DFT calculation of the density of states for the A-type AF $LaMnO_3$.

33 Conclusions

The UHF calculations reported in the present chapter have allowed the study of the ground state properties of $CaMnO_3$ and $LaMnO_3$.

The Mulliken population analysis finds a total charge on Mn which is close to +2 in both $CaMnO_3$ and $LaMnO_3$, indicating the presence of extra electrons. These come from semicovalent bonds with oxygen on the O-Mn-O chain; the degree of semicovalency is higher in $CaMnO_3$, with more charge transferred from O to Mn than in $LaMnO_3$. The situation is consistent with a picture based on availability of empty hybrids for electron sharing, like in Goodenough's model. The way UHF describes the change in valence states in going from $CaMnO_3$ to $LaMnO_3$ is, therefore, in terms of decreasing semicovalency, with a total charge that stays around +2. The magnetic moment, on the other hand, is always close to the expected Hund's rule value, as confirmed by band structure and density of states plots. UHF calculations of energy differences for various spin orderings in cubic $CaMnO_3$ predict the correct ground state, in agreement with experiments and with the Goodenough model. The value of the (antiferromagnetic) exchange interaction is in good agreement with other calculations but is overestimated (about 63% higher) compared to the experimental one.

In the case of $LaMnO_3$, a study of the idealised cubic structure allows to identify independent spin and orbital ordering terms in the Hamiltonian; charge density difference plots are a very useful tool to visualise the relationship between spin, orbital ordering and crystal distortions. UHF calculations on *Pnma* $LaMnO_3$ with optimised lattice parameters and atom positions well describe the ground state of the compound, giving exchange coupling with the expected sign. Calculated Js are, nevertheless, below the experimental values.

This discrepancy will be eliminated by performing Configuration Interacton calculations. They will give an insight into the mechanism of exchange coupling, identifying the interactions that are mainly responsible for it, and will make it possible to get better values for J as well. All this will be the subject of the next chapter, in which the results of the CI study of $CaMnO_3$ and $LaMnO_3$ are reported.

Chapter 4

CI calculations on $CaMnO_3$ and $LaMnO_3$

UHF calculations on $CaMnO_3$ and $LaMnO_3$ presented in the previous chapter show that the ground state of these compounds is correctly described and that the exchange couplings have the expected sign. Their values, though, are overestimated in one case and underestimated in the other. In this chapter Configuration Interaction (CI) calculations performed on clusters of manganites are discussed.

CI provides a way to go beyond the HF approximation and to improve on it by introducing electron correlation. It gives a simple and straightforward way of exploring the role that configurations other than the ground state have in determining the magnetic behaviour in strongly correlated materials and of checking the validity of the proposed theories based on model Hamiltonians.

In the present chapter, results are reported for CI calculations on clusters of manganites representing $CaMnO_3$ and $LaMnO_3$; they have been carried out using the Direct CI module as implemented in the package GAMESS-UK, described in Chapter 2. Exchange couplings were calculated as energy differences between two spin states in a localised orbital basis and they are in good agreement with reported experimental values for $CaMnO_3$ and

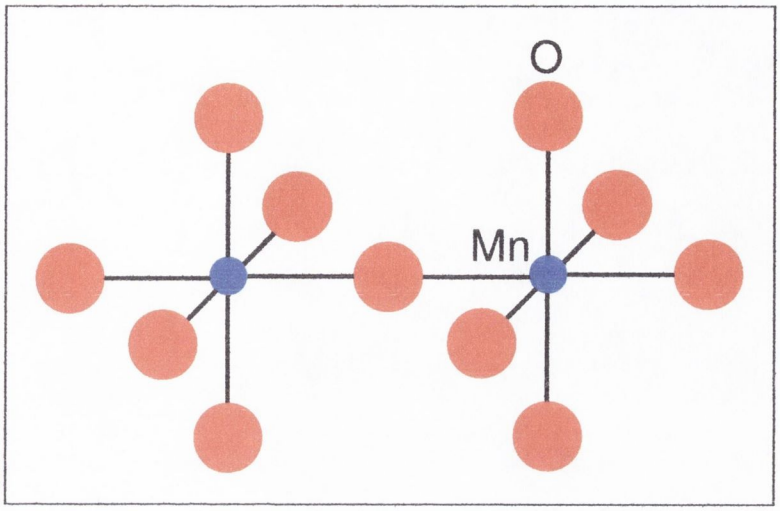

Figure 4.1: Cluster used in the study of manganites; the Mn-O-Mn axis is along the z direction.

$LaMnO_3$; an analysis of the wave functions also made it possible to determine which exchange processes turn out to be important in the exchange coupling mechanism.

The chapter starts with an introduction to describe the way calculations were performed; then the results for $CaMnO_3$ and $LaMnO_3$ are presented and discussed.

4.1 Introduction to the calculations

The first step in the CI study is the identification of the cluster to be used. The aim of the present calculations is to investigate the exchange coupling mechanism between two neighbouring Mn ions via the central oxygen; so the cluster chosen includes the two manganese atoms with their surrounding (nearest neighbour) oxygen octahedra sharing a common vertex, for a total of thirteen atoms (see Fig. 4.1). Of course, atomic positions are assigned in such a way to reproduce distances occurring in the crystal. These thirteen

atoms are treated quantum mechanically, using the same Gaussian basis set as in the UHF calculations.

A different number of electrons (or, in other words, a different total charge) is present in the cluster, depending on whether it is used to describe $CaMnO_3$ or $LaMnO_3$. So an $Mn_2O_{11}^{14-}$ cluster represents $CaMnO_3$ and an $Mn_2O_{11}^{16-}$ cluster represents $LaMnO_3$.

An important feature of the exchange coupling constants in $CaMnO_3$ and $LaMnO_3$ is that their value strongly depends on the population of the Mn e_g and of the O $2p$ orbital. Fig. 4.2 shows how the Js calculated from clusters representing $CaMnO_3$ and $LaMnO_3$ vary as a function of the charge of the Mn ion. It then becomes a fundamental issue to be able to reproduce a population as close as possible to the one found in the bulk by the UHF calculations (see Tables 3.2 and 3.10). To achieve this, the cluster has been embedded in a spherical array of point charges; they were placed at the ionic sites of the compounds and the value of the charges was adjusted so that the correct population on the cluster ions was obtained. This was necessary to recreate the crystal environment and to generate the correct Madelung potential. In both $CaMnO_3$ and $LaMnO_3$ the radius of the sphere was about 20 Å and included over 3000 charges.

In the previous chapter it was found that the number of electrons in the $3d$ shell for the two compounds is actually five (rather than three and four). The question arises of what is the effect of the number of cluster electrons on the calculated value of the exchange couplings. In other word, whether it would be possible to reproduce the current results by using a cluster with a total number of electrons equal to the number found in the UHF approximation. A test calculation with such a number in the cluster representing calcium manganite and no point charge around it, though, could not be successfully

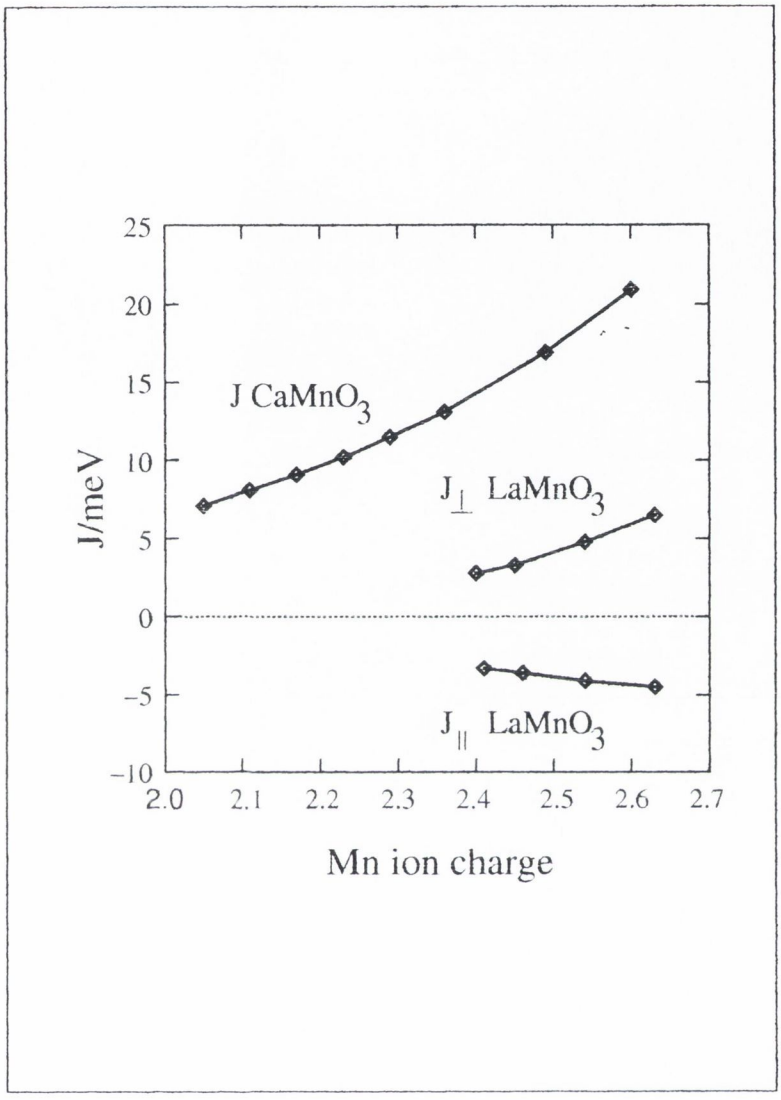

Figure 4.2: Exchange coupling constants for $CaMnO_3$ and $LaMnO_3$ from CI calculations as a function of Mn ion Mulliken populations.

run because the self-consistent cycles before the CI treatment of the wave function (see below) were very unstable and did not converge. So the problem remains unsolved and the question is still open.

The effect of truncating the point charge array at a finite distance has been examined in detail in ref. [115]; using smaller point charge arrays than

tie ones used in the present work, the authors of that paper found that tie Madelung potential in the centre of the cluster had a root mean square dfference from the full Madelung potential of about 3 %. Details about the vilues of the point charges for the two clusters will be given in the following sictions.

The next thing to do in this type of calculation is to generate a suitable starting wave function for the successive CI treatment. This is found if one notes that high spin multiplicity states, such as the septet and the nonet states of the clusters used here, are generally well described by a self consistent field (SCF) restricted open shell Hartree-Foch (ROHF) wave function. So ROHF orbitals were generated using the corresponding module in GAMESS. The spin multiplicity of the wave function was seven for $CaMnO_3$ and nine for $LaMnO_3$, i.e. the high spin states for both clusters which have six and eight unpaired electrons, respectively.

The CI calculations were carried out in a localised orbital basis which provides a means of identifying the exchange coupling mechanism in terms of fluctuations of electrons between the localised orbitals. Orbitals were localised using the Foster-Boys algorithm [123] which generates localised orbitals with maximally separated centroids. Orbitals were actually localised in three separate steps: doubly occupied O $2p$ were localised first, then singly occupied Mn d orbitals (t_{2g} only for $Mn_2O_{11}^{14-}$, t_{2g} and the occupied e_g for the $Mn_2O_{11}^{16-}$ cluster), and then empty Mn e_g orbitals. Three separate localisation steps are necessary to preserve the invariance of the ROHF energy, since any mixing of orbitals with different occupancy would result in an increase of the total energy.

The way the wave functions for the CI calculations were constructed from this localised orbitals is now explained in more detail. First of all, following

he procedure used in GAMESS, the orbital space was partitioned into a ore space, an active space and a space of redundant, unoccupied orbitals vhich were discarded in the construction of the CI wave function. Doubly ccupied orbitals belong to the core space, with the exception of the three O p orbitals (p_x, p_y and p_z) localised at the site of the central oxygen atom, the ne that forms the common vertex of the two octahedra. They belong to the ctive space, together with the occupied and unoccupied Mn d orbitals. The ctive space was further divided into an internal (doubly or singly occupied rbitals) and an external space (orbitals, initially unoccupied, the occupation f which is allowed during the CI process).

As already mentioned in Chapter 2, eigenstates of a Hamiltonian describing spin systems can be written as linear combinations of SAFs, which are anti-symmetrised products of space orbitals and SEFs (eqs. (2.14) and (2.15)); the Direct CI module in GAMESS uses the Yamanouchi-Kotani (YK) scheme[127] for generating them. Referring, for example, to the septet state for the $Mn_2O_{11}^{14-}$ cluster, the corresponding SAF was constructed from six singly occupied t_{2g} orbitals and doubly occupied core orbitals. The form of the wave function can be written as

$$\psi^{\text{sept}} = A\left(\{\text{core}\}(\phi_{xy,l}\phi_{xz,l}\phi_{yz,l}\phi_{xy,r}\phi_{xz,r}\phi_{yz,r})(\alpha\alpha\alpha\alpha\alpha\alpha)\right). \qquad (4.1)$$

Here {core}, the product of the doubly occupied orbitals in the core space, includes the three O $2p$ orbitals localised on the central oxygen; l and r on the t_{2g} orbitals indicates whether they are centered on the left or on the right Mn ion, respectively.

The singlet was constructed from the same set of localised orbitals; the satisfactory results obtained demonstrate that the localised orbitals generated for the high spin state are a very good approximation to the optimal orbitals for open-shell low-spin multiplicity states and that a high-spin mul-

tplicity ROHF wave function is an excellent starting point for perturbative calculations on high and low spin multiplicity states in the solid state. The spin coupling, in the singlet case, has the form

$$\frac{1}{\sqrt{2}}(\alpha\alpha\alpha\beta\beta\beta - \beta\beta\beta\alpha\alpha\alpha) \quad . \tag{4.2}$$

Eq. (4.2) is one of the five spin eigenfunctions Θ_a for six electrons coupled into a singlet state[1].

Hund's rule requires all three spins on each Mn ion to point in the same direction; so this SEF is expected to have the larger weight in the CI wave functions. This is actually what happens, provided that the spatial orbitals multiplying this SEF are previously ordered in such a way that Mn orbitals localised on each side are grouped together. The spin-adapted wave function for the singlet is, therefore,

$$\psi^{\text{sing}} = \frac{1}{\sqrt{2}} A\left(\{\text{core}\}(\phi_{xy,l}\phi_{xz,l}\phi_{yz,l}\phi_{xy,r}\phi_{xz,r}\phi_{yz,r})(\alpha\alpha\alpha\beta\beta\beta - \beta\beta\beta\alpha\alpha\alpha)\right) . \tag{4.3}$$

SEFs for the nonet and the singlet in $LaMnO_3$, containing eight electrons, are constructed in exactly the same way.

If the determinantal energies of the singlet and of the high spin wave functions are evaluated (using conventional rules[77]), **the singlet always has a higher energy**[2].

When the CI expansion of the wave function is carried out, all possible single and double excitations into the empty, available orbitals are included. So the septet and the singlet described in eqs. 4.1 and 4.3 (or the nonet and

[1] GAMESS simply indicates this as the SEF number five (see (2.17)); anyway, even if formed with contributions from all twenty primitive functions, that SEF can be approximated with the form of eq. (4.2).

[2] The same property, for example, is found for the He atom in the $1s2s$ configuration; in that case the triplet is below the singlet when they are described by the Heitler-London valence bond wave functions.

singlet in the case of the $Mn_2O_{11}^{16-}$ cluster) are the dominant SAFs (main configurations) in the more general CI expansion which includes other SAFs. These SAFs will be described in more details in the next two sections, which report the results of the CI calculations on the clusters studied.

4.2 CI results for $CaMnO_3$

This section reports the results of the CI calculations on the $Mn_2O_{11}^{14-}$ cluster representing $CaMnO_3$. Some of the localised orbitals used in the calculation are shown in fig. 4.3. In the calculations the Mn-O-Mn bonding is along the z axis, so the doubly occupied O $2p_z$ (fig. 4.3(a)) and the empty (e_g) Mn $d_{3z^2-r^2}$ (fig. 4.3(c)) are the orbitals which are mainly responsible for the exchange coupling.

In the previous section the dependence of the exchange couplings on the Mn charge and on the Madelung potential of the cluster was pointed out. The latter has been taken into account by surrounding the cluster with an array of point charges, located at the ionic sites of the crystal. The dependence on the Mn population is shown in Fig. 4.2 (upper curve). It can be seen that J increases for increasing population on the Mn, and it is easy to understand why. Since the Mn ionic charge is different from 4+, there is a population on the (nominally empty) e_g orbitals. Because (see below) the main process involved in the exchange coupling mechanism is the charge transfer to/from the e_g orbitals, for greater values of Mn charge there is more room for charge transfer and J increases.

UHF calculations on $CaMnO_3$ found Mulliken populations which were quite different from the nominal values; they were taken as a guide to build up charges in the present case. From Table 3.2 it can be seen that they were $Ca^{+1.86}Mn^{+2.13}O^{-1.33}$; if these are used as values for the corresponding point

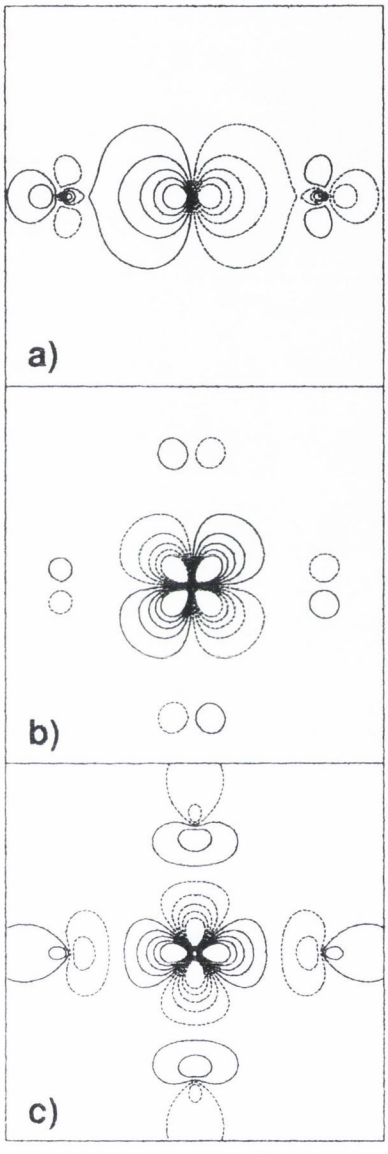

Figure 4.3: Localised orbitals used in the cluster CI calculations for $CaMnO_3$. a) O $2p_z$; b) Mn d_{xz}; c) Mn $d_{3z^2-r^2}$.

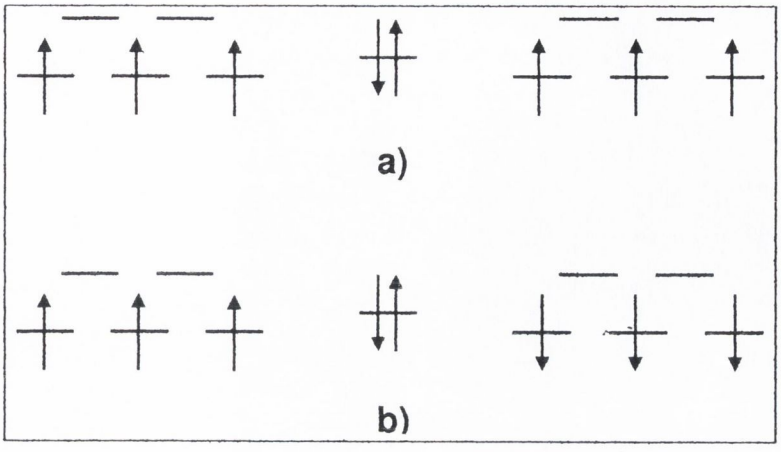

Figure 4.4: Fundamental SAFs for $CaMnO_3$; a) septet, b) singlet. Only one O $2p$ orbital is shown for clarity.

charges, however, the resulting ROHF population on the Mn-O-Mn central triad is $Mn^{+2.60}O^{-1.31}Mn^{+2.60}$, i.e. there is excessive charge on the Mn ions. So the point charge values were adjusted to $Ca^{+1.15}Mn^{+2.84}O^{-1.33}$, and this choice resulted in $Mn^{+2.17}O^{-1.61}Mn^{+2.17}$ for the central triad and $O^{-1.64}$ and $O^{-1.67}$ for the other two types of oxygen in the cluster; in other words, as a consequence of the adjustment, charge is tranferred from the outer oxygens to the central Mn and O ions, each gaining about 0.4 e. Note that these adjustments leave each point charge unit cell neutral, while the radius of the sphere of point charges is also adjusted to return an entire cluster with a total charge close to zero (this is achieved with a total of 3019 centres in the present case).

The fundamental SAFs for the septet and singlet state were given in eqns. 4.1 and 4.3; a schematic picture to help visualising them is found in fig. 4.4. When these are the only SAFs present in the CI wave function for each of the two spin states, they come with a coefficient c_i of unity. As pointed out above, the singlet is above the septet and the energy difference between

them is 3.6 meV. When additional SAFs are permitted by allowing single and double excitations to take place, the weight of the fundamental SAFs is below one and the additional SAFs appear in the wave function, even if with a much smaller weight. Although the active space used is very limited, there are quite a few SAFs entering the CI wave function; there are, for example, four possible SAFs in which an electron hops from one Mn t_{2g} orbital on the right to another t_{2g} orbital on the left (no contribution, as expected, comes from xy orbitals, as well as several SAFs in which an electron is excited from an O $2p$ orbital to an Mn e_g orbital. In order to analyse the wave function, it is convenient to use the sum of the squares of the occupancies (i.e. $|c_i^2|$) of all configurations of a particular type; comparing them, it is then possible to quantify the relative importance that each configuration holds in the total wave function. Table 4.1 shows relative energies and summed occupancies obtained from the CI calculations for the cluster representing $CaMnO_3$; occupation numbers refer to $t_{2g} \rightarrow t_{2g}$ exchange, in which an electron has hopped from one Mn ion to the other, and to O$\rightarrow e_g$ exchange, in which 1 or 2 electrons are transferred from an O $2p$ orbital to an Mn ion[3]. A schematic picture of these excitations is also given in fig. 4.5.

From the table it can be seen that when the single and double excitations in the active space are allowed, the main SAF contributes to the wave function with an occupation of 0.9926 in the singlet and of 0.9943 in the septet state; therefore there are larger correlations for the singlet than for the septet. In the singlet case there is a contribution from the $t_{2g} \rightarrow t_{2g}$ exchange (these fluctuations are absent in the septet as a consequence of Pauli exclusion principle), but this contribution is only 0.0005, much smaller

[3]The sum of SAF occupancies is slightly less than unity when excitations are allowed. This is because there is a large number of configuration with a coefficient smaller, in absolute value, than 0.003, which would only contribute 0.000009 to the sum and have therefore been omitted.

State	Energy[a]	Main SAF	$t_{2g} \rightarrow t_{2g}$	O $\rightarrow e_g$ (1e)	O $\rightarrow e_g$ (2e)
singlet[b]	+3.6	1.0000	0.0000	0.0000	0.0000
septet[b]	0.0	1.0000	0.0000	0.0000	0.0000
singlet[c]	-149.6	0.9926	0.0005	0.0038	0.0017
septet[c]	-133.4	0.9943	0.0000	0.0027	0.0017

Table 4.1: Relative energies (in meV) and SAF occupation numbers for singlet and septet states of the $Mn_2O_{11}^{14-}$ cluster representing $CaMnO_3$.
[a] Energies are relative to the ROHF septet state
[b] Fundamental SAFs only
[c] Fundamental SAFs + all single and double excitations into the active space

than the others. O$\rightarrow e_g$ contribution are the same for both spin states for the hopping of two electrons; what is different is the coefficient that gives the contribution of single O$\rightarrow e_g$ excitations: it is 0.0038 for the singlet and 0.0027 for the septet.

Table 4.1 also lists the energies of the states relative to the ROHF septet. The septet is 133.4 meV below the fundamental septet SAF energy (which is, of course, the same as the ROHF septet); this is the correlation energy for that state. Eq. (2.11) gives a general definition of the correlation energy in solid state physics as the difference between an SCF energy (e.g. the HF energy) and the energy of a wave function in which correlations have been included (exact wave function). Here it is defined as the difference between the fundamental SAF energy and the energy calculated when excitations are allowed to take place within the active space [4]. The singlet fundamental SAF energy is 3.6 meV higher then the corresponding septet one; when excitations are allowed the singlet energy is 149.6 meV lower than the reference septet energy, so that the correlation energy for the singlet state is 153.2 meV.

[4] The active space considered is of limited size and additional correlation energies might be present. There might be, for example, fluctuations within an O ion. They have not been considered here because they are believed to give a minor contribution to the exchange constants

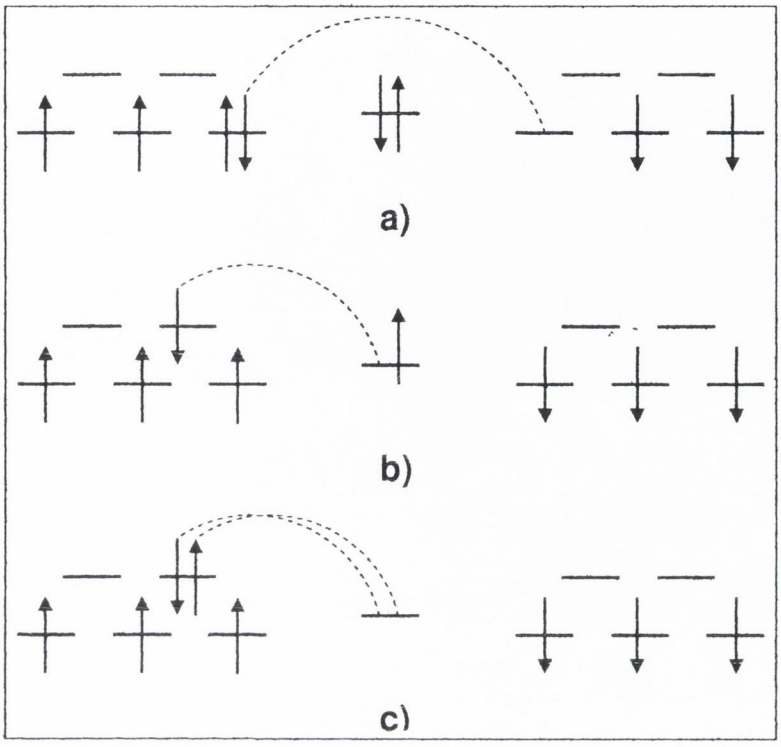

Figure 4.5: Schematic view of the main excitations included in the CI expansion of the singlet and septet wave function for $CaMnO_3$ (see Table 4.1). a) $t_{2g} \rightarrow t_{2g}$; b) O $\rightarrow e_g$ $(1e)$; c) O $\rightarrow e_g$ $(2e)$.

According to eq. (1.14), the exchange coupling is calculated as half the energy difference between septet and singlet when the additional SAFs are taken into account; this gives for J a value of 8.1 meV, which is in good agreement with the reported experimental value of 6.6 meV, estimated from a Néel temperature of 110 K, and with recently reported values from model Hamiltonian calculations [75].

To end this section, it worth adding a final note about the effect that point charges have on the exchange coupling. First of all, a calculation was carried out on the $Mn_2O_{11}^{14-}$ cluster with no external point charges.The Mulliken population on the central Mn-O-Mn chain was, in that case, $Mn^{+2.46}O^{-0.94}Mn^{+2.46}$ and the exchange coupling was calculated to be 58.5 meV i.e. too much in

excess compared to the experimental value. Then a calculation in which the point charges were set at the UHF Mulliken population values gave $J = 21.0$ meV. When they were adjusted to the values described above, J dropped to 8.1 meV and there was a sharp decrease in degree of correlation of the wave function. This could have been expected and is in agreement with experiment.

4.3 CI results for $LaMnO_3$

In the case of $LaMnO_3$ two exchange couplings are defined: a ferromagnetic one in the plane ($J_{||}$) and an antiferromagnetic one along the vertical direction ($J_{\perp}$). So two different $Mn_2O_{11}^{16-}$ clusters need to be considered. The first one, describing an Mn-O-Mn triad (and the corresponding surrounding octahedra) situated in the plane, in which two different Mn-O bond lengths are present, was used for the calculation of $J_{||}$. The second one described a cluster oriented along the vertical direction, where there is only one Mn-O bond length, and this was used to calculate $J_{\perp}$. Atom distances and bond angles were the same as the ones used in the optimised *Pnma* structure described in the previous chapter. Both types of cluster were surrounded by a spherical array of point charges, again located at the positions corresponding to the optimised *Pnma* crystal; their values were adjusted in order to recreate the bulk Mulliken population on the Mn ions and on the central oxygen found within the UHF approximation, i.e. $La^{+3.15}Mn^{+2.24}O^{-1.75,-1.82}$ (see Table 3.10). Using the same kind of approach as in the $Mn_2O_{11}^{14-}$ cluster for $CaMnO_3$, point charges were adjusted to be $La^{+2.80}Mn^{+2.60}O^{-1.80,-1.80}$, and this choice resulted in a Mulliken population of $Mn^{+2.45}O^{-1.65}Mn^{+2.45}$ for the central triad ions. The total charge of the cluster was kept close to neutrality by using a total number of centres equal to 3735.

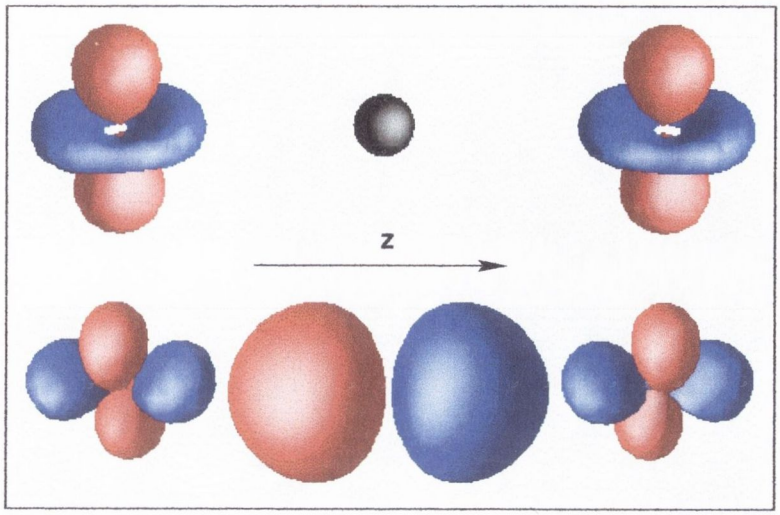

Figure 4.6: Localised orbitals used for the CI calculation of the exchange constant $J_\perp$ in the cluster representing $LaMnO_3$. Top: occupied Mn e_g; bottom: empty Mn e_g orbitals and O $2p_z$. The dark sphere is at the oxygen position.

The strong dependence of the exchange coupling on the Mn charge can be observed in the middle and lower curve in fig. 4.2. Both of them show the same kind of behaviour that was described for J in $CaMnO_3$; in the curve for $J_{||}$ the coupling depends less dramatically on the Mn ion charge, nevertheless an increase in its negative value is still observed for increasing Mn ion charge.

Some of the localised orbitals used in the CI calculations are shown in Figs. 4.6 and 4.7 in a 3d representation. Fig. 4.6 shows the orbitals that were used for the calculation of the antiferromagnetic $J_\perp$, so there is only one kind of occupied e_g orbital, oriented perpendicular to the Mn-O-Mn axis (top), and one kind of unoccupied e_g orbital, oriented along the Mn-O-Mn axis (shown it the bottom, together with the O $2p_z$ orbital).

Orbitals used for the calculation of the ferromagnetic $J_{||}$ are, instead, shown in fig. 4.7. The top panel shows occupied e_g orbitals of alternate $d_{3y^2-r^2}$ and $d_{3z^2-r^2}$ symmetry. The opposite alternation is found in the bot-

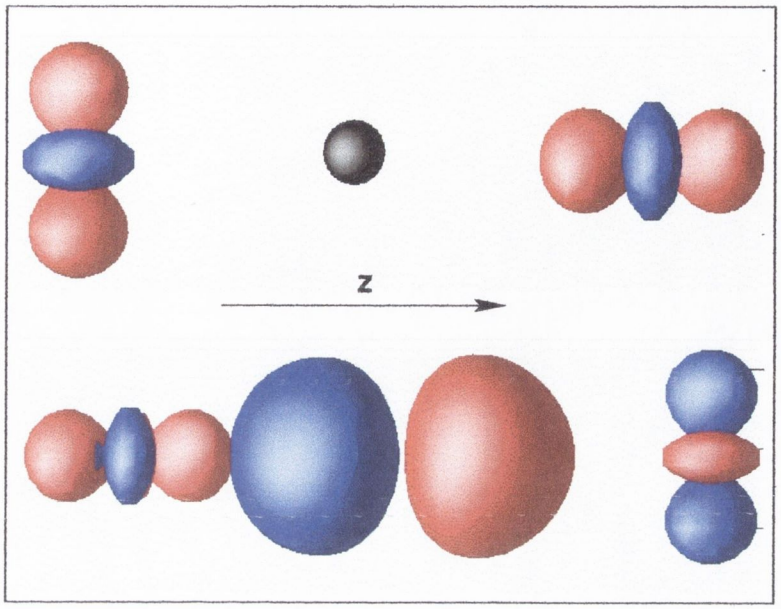

Figure 4.7: Localised orbitals used for the CI cluster calculation of the exchange constant $J_{||}$ in $LaMnO_3$. Top panel: occupied Mn e_g; bottom panel: empty Mn e_g and O $2p_z$. The e_g orbital on the left is the one involved into the exchange process. The dark sphere is at the oxygen position.

tom panel containing the empty e_g orbitals, as well as the O $2p_z$ orbital; the e_g orbital on the left is the one involved in the exchange process.

Looking at the localised orbitals in $LaMnO_3$, the dependence of the exchange coupling on the e_g population shown in Fig. 4.2 has a simple, intuitive explanation. To change the population of the e_g orbitals means to change their shape and orientation in space, which in turn affects the extent of the coupling.

The fundamental SAFs in this case are the singlet and nonet states and can be derived in the same way as the singlet and septet for $CaMnO_3$ were derived in eqns. 4.3 and 4.1. A schematic representation is given in Fig. 4.8.

Energy differences and summed occupation numbers from the CI calcula-

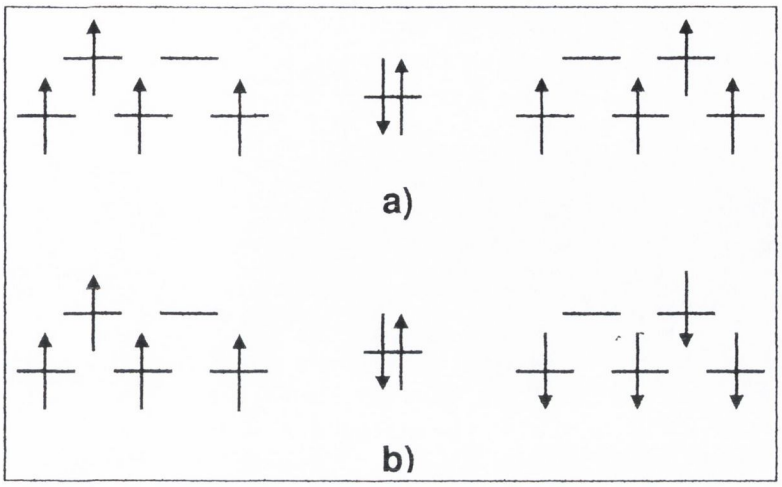

Figure 4.8: Fundamental SAFs for $LaMnO_3$; a) nonet, b) singlet. Only one O $2p$ orbital is shown for clarity.

tions are given in Table 4.2. In the cluster calculation corresponding to Mn ions coupled along the vertical direction by the exchange coupling $J_\perp$, the fundamental SAF for the singlet state is 11.9 meV above the nonet. When additional SAFs are included by allowing all single and double excitations within the considered active space the singlet and the nonet are found to be 93.5 and 83.3 meV respectively below the reference fundamental SAF energy. So the correlation energies are 83.3 meV for the nonet and 105.4 meV for the singlet. In the case of the calculation on the cluster corresponding to Mn ions coupled in the plane by $J_{||}$, the fundamental SAF for the singlet state is 17.9 meV higher then the nonet. After excitations have been included in the CI process, the singlet and the nonet have a relative energy of -64.9 and -79.9 meV, and the correlation energies are 82.8 and 79.9 respectively.

From the table it can be seen that, as in the case of $CaMnO_3$, the excitations from O to e_g involving one electron are the main fluctuations about the fundamental SAFs. Both for $J_\perp$ and $J_{||}$, occupation numbers for the singlet are smaller the for the nonet, to indicate that larger correlations are present

$J_\perp$

State	Energy[a]	Main SAF	$t_{2g} \rightarrow t_{2g}$	O $\rightarrow e_g$ (1e)	O $\rightarrow e_g$ (2e)
singlet[b]	+11.9	1.0000	0.0000	0.0000	0.0000
nonet[b]	0.0	1.0000	0.0000	0.0000	0.0000
singlet[c]	-93.5	0.9937	0.0006	0.0037	0.0007
nonet[c]	-83.3	0.9954	0.0000	0.0030	0.0007

$J_\parallel$

State	Energy[a]	Main SAF	$t_{2g} \rightarrow t_{2g}$	O $\rightarrow e_g$ (1e)	O $\rightarrow e_g$ (2e)
singlet[b]	+17.9	1.0000	0.0000	0.0000	0.0000
nonet[b]	0.0	1.0000	0.0000	0.0000	0.0000
singlet[c]	-64.9	0.9949	0.0004	0.0025	0.0006
nonet[c]	-79.9	0.9946	0.0000	0.0038	0.0008

Table 4.2: Relative energies (in meV) and SAF occupation numbers for singlet and nonet states of the $Mn_2O_{11}^{16-}$ cluster representing $LaMnO_3$.
[a]Energies are relative to the ROHF nonet state
[b]Fundamental SAFs only
[c]Fundamental SAFs + all single and double excitations into the active space

compared to the high spin case.

From the energy difference between nonet and singlet the exchange couplings can be calculated, and they turn out to be

$$J_\perp = 5.1 \quad \text{meV}$$

and

$$J_\parallel = -7.5 \quad \text{meV}.$$

It should be recalled that they have to be compared to experimental values of 4.8 and -6.7 meV [69].

A CI calculation was also performed on a cluster in which experimental structural parameters and atomic positions were used. Surrounding point charges had values that were close to the Mulliken population values from UHF calculations, namely +2.6 for Mn, -1.8 for O and +2.8 for La. The resulting exchange coupling constants were 3.3 (for $J_\perp$) and -3.6 meV (for

$J_{||}$). They are quite different from the ones reported above, and this shows the effect that a proper choice of point charge values has on the final results.

A further test of the influence the Madelung constants of the cluster has on the exchange constant has also been carried out. Obviously ions which are several lattice constants away from the central cluster will have negligible influence on the central cluster and can be treated as point charges rather then distributed charges without significantly alterate the potential and affect the calculation [115, 116, 118]. In order to estimate the consequences of terminating the cluster with point charges, a CI calculation was performed in which the 12 La ions situated immediately close to the central cluster were replaced by La^{3+} pseudopotentials (the 54 electron core LANL pseudopotential was used [131]). This resulted in a small increase in $J_{\perp}$ (from 5.1 to 5.2 meV) and in no change for $J_{||}$ (-7.5 meV were obtained again). So no difference is found compared to the previous calculation.

4.4 Conclusions and discussion

Cluster CI calculations provide a way to get detailed information on the exchange coupling mechanism. Results are strongly dependent on the Madelung potential of an array of point charges surrounding the cluster; the magnitude of such point charges needs to be adjusted in order to recreate a charge population close to the value found in the bulk UHF calculations on the central Mn and O ions. This is true for both $CaMnO_3$ and $LaMnO_3$; the latter compound is, though, more ionic, with UHF charges closer to the nominal values. In $CaMnO_3$ a calculation in which the point charges were kept at the nominal values has given an energy difference between septet end singlet of 57 meV (i.e. a J of 28.5 meV), far larger than the experimental result. This characteristic of the manganites is well shown in fig. 4.2. Once this has been

taken into account, calculated exchange couplings are in good agreement with reported experimental values.

In order to understand the main processes involved in the exchange mechanism, occupation numbers have been tabulated for the various SAFs that take part in the CI wave function (see Tables 4.1 and 4.2). The $O \rightarrow e_g$ exchange involving 1 electron always gives the higher contribution, so it can be considered as the main responsible for the exchange coupling. It is worth noting, at this point, that the type of excitations described by Millis [73] to be fundamental in the exchange process, i.e. those obtained when a couple of electrons from the central oxygen hop onto the two Mn ions on the left and on the right *simultaneously*, is not found in the present calculations. The common feature of the two theories, though, is that the $2p \rightarrow e_g$ exchange is the main process involved, a conclusion which is also found in the work by Satpathy and collaborators [75].

An important role is played by the correlation energy of the different states involved. In the singlet state, they are always higher than the correlation energy for the corresponding high spin case. This is true for a wide range of magnetic ions which are exchange coupled *via* a closed shell non-magnetic anion. The reason is because there are many more singlet SAFs then high spin SAFs in any particular active space. In the case, for example, of the active space used for $LaMnO_3$, there are over 18,000 singlet SAFs compared to about 1,500 nonet SAFs: given a specific number of electrons, there are many more ways to arrange them to form singlet states than there are to form nonet states. So, even if only a few of them appear in the CI wave function with a significant weight, it is not surprising that the singlet correlation energy is larger.

The correlation energy is related to the number of empty e_g orbitals avail-

able in the exchange process. In $CaMnO_3$ and along the vertical direction in $LaMnO_3$ there are two empty Mn e_g orbitals available and, as a consequence, the singlet correlation energy is significantly larger then the high spin state correlation energy. This is enough to bring the singlet (which was higher when only the fundamental SAFs were considered) below the high spin state and an antiferromagnetic coupling is obtained. For the other case studied, namely the calculation of the in-plane constant $J_{||}$, there is only one available Mn e_g orbital and the singlet correlation energy is just higher then the nonet correlation energy. In this case, considering that the fundamental SAF for the singlet is 17.9 meV above the nonet, the exchange process is not enough to bring the singlet below the nonet and a ferromagnetic coupling is found. In other words, the coupling of a couple of Mn ions is antiferromagnetic when the difference in the singlet and high spin state correlation energies *exceeds* the splitting between the fundamental SAFs of the singlet and of the high spin state.

Fig. 4.9 is presented as a conclusion to the present chapter. It summarises the main results of this CI study of $CaMnO_3$ and $LaMnO_3$. It shows, for each of the clusters considered, the correlation energies, the energy difference between low and high spin states and the occupancy of the main SAF in each spin state.

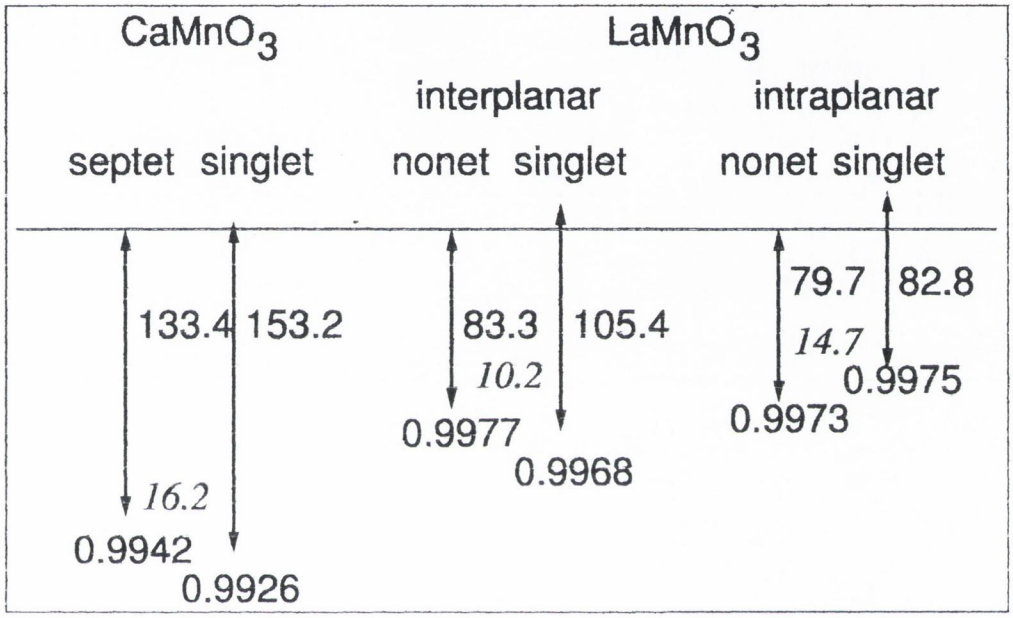

Figure 4.9: Summary of main results of cluster CI calculations. Correlation energies are represented by vertical arrows and are given in meV in plain text. Energy differences between low and high spin states (which are equivalent to double the corresponding exchange constant) are given in italics and occupancies of the fundamental SAF in each state are printed at the base of each arrow. The horizontal line is the reference SCF ROHF energy for each state.

Conclusions and outlook for future work

I never think of the future. It comes soon enough.

A. Einstein

The present thesis has dealt with the calculation of exchange coupling constants in $CaMnO_3$ and $LaMnO_3$; this has been done using two *ab initio* methods, the Unrestricted Hartree-Fock and the Configuration Interaction.

Manganites have been extensively studied in the last few years because of their colossal magnetoresistance properties and the consequent possibility of practical applications in magnetic devices. But these compounds are also interesting in themselves, for the fundamental questions that they pose to theoreticians. Orbital ordering, charge ordering, Jahn-Teller effect, magnetic polarons and many other concepts have been introduced in order to explain the magnetoresistance and the other particular behaviours (such as the metal-insulator transition) in manganites. A comprehension of the mechanisms governing the exchange coupling (and hence the magnetic properties) is still far from complete, and the present thesis aims to contribute in this direction.

It is well known that a single-particle theory is not suitable for an accurate description of stongly correlated electron systems such as the manganites.

Nevertheless, UHF has proven to give reasonable results, at least for ground states; due to its exact treatment of the exchange, that leads to the cancellation of the unphysical electron self-interaction, it performs definitely better than Density Functional Theory, where the exchange-correlation potential is approximated.

The UHF study carried out in this work has reproduced the expected magnetic behaviour and crystal structure of $CaMnO_3$ and $LaMnO_3$. In particular, for the latter compound, by investigating an idealised cubic structure, it has been possible to identify independent contributions to the Hamiltonian from spin and orbital ordering terms.

Hartree-Fock wave functions have been used as a starting point for a successive Configuration Interaction study of clusters representing $CaMnO_3$ and $LaMnO_3$. CI is one of the simplest methods to include correlation effects in the Hamiltonian. The calculations were carried out in a basis of localised orbitals. By allowing single and double excitations to take place from the ground-state HF configuration, the exchange coupling has been studied in terms of fluctuations of electrons. This has allowed to identify which configurations other than the ground state take part in the exchange coupling mechanism and their weight in the total wave function. $O \rightarrow e_g$ hopping have been found to be the main source of superexchange.

A central issue of the CI calculations is that the results are strongly dependent on the population of the e_g and O $2p$ orbitals, which is in turn influenced by an array of point charges surrounding the cluster. The values of such point charges needed to be adjusted to reproduce the correct Madelung potential of the crystal and, as a consequence, the UHF population of the e_g and O $2p$ orbitals. Following these adjustments, the exchange coupling constants have been calculated; they are in good agreement with experimental estimates and

with other reported values from *ab initio* or model Hamiltonian methods.

Fig. 4.9 at the end of Chapter 4, which summarises the results of the CI calculations, can be regarded as the main conclusion of the present thesis. In particular it clearly shows the role that the correlation energy has in determining the spin ordering, i.e. in selecting the ground state spin arrangement.

Apart from the results obtained, the work carried out in this thesis has also laid the foundation for some future work. The same kind of study can be extended to manganites with mixed Mn^{3+}-Mn^{4+} valence, and in particular to the region of the phase diagram characterised by colossal magnetoresistance behaviour. Some preliminary UHF calculations on $La_{1/2}Ca_{1/2}MnO_3$ [134] show that the simple picture of a lattice of alternating Mn^{3+} and Mn^{4+} ions is not actually realised; instead, both manganese have a charge of about 3+ and the hole is by preference localised on the oxygen. The ROHF treatment of the corresponding cluster confirms this result: the calculation with an Mn^{3+}-Mn^{4+} alternation is about 0.3 eV higher in energy than the one in which the hole is on the oxygen.

Another possible application of the same technique could be the study of layered cuprates superconductors, where the exchange coupling also have an important role [135].

The Configuration Interaction approximation can also provide parameters for model Hamiltonian calculations. Such parameters are usually guessed on the basis of physical considerations. CI allows them to be obtained from an *ab initio method*. Work is in progress at the moment to calculate such parameters; then they will be used to solve the Hamiltonian with a quantum Monte Carlo technique [136].

Appendix: Details of calculations

This appendix shows details of the *ab initio* calculations on $CaMnO_3$ and $LaMnO_3$ and described in Chapters 3 and 4. The basis sets employed for the description of the atomic orbitals of calcium, lanthanum, manganese and oxygen are reported and explained. The k-point mesh used in the reciprocal space integration and the method for its selection are outlined.

A. Gaussian basis sets

Gaussian basis sets used for both UHF and CI calculations were briefly described in section 2.4. This section reports the details of the basis sets used for Ca, La, Mn and O; the basis sets describing the last two elements were the same in the case of $CaMnO_3$ and of $LaMnO_3$.

Each atomic orbital is described by a linear combination of individually normalized Gaussians (eq. (2.10)); exponents (in $Bohr^{-2}$) and contraction coefficients must be specified in the input file. The type of shell must also be specified: s, p or d. The sp type can also be chosen, in which an s and a p shell have different contraction coefficients but share the same exponent; such a choice results in a reduction of the auxiliary functions that need to be calculated for the evaluations of electron integrals and is, therefore, is computationally more convenient from the point of view of speed of execution.

It is conventional to describe the basis set using a string of digits representing the number of gaussian primitives in each contraction. Core and valence functions are separated by a dash; polarisation functions are preceded by the corresponding letter according to their type (s, p, d). The string terminates with a G which stands for Gaussian.

For example, the basis set used for Mn is labelled 86-411d41G. It means that the two core shells ($1s$ and $2sp$) are formed with 8 and 6 contractions respectively, and that there are 4, 1 and 1 contractions in the valence shells ($3sp$, $4sp$ and $5sp$). Finally, two d polarisation functions follow ($3d$ and $4d$), with 4 and 1 contractions. This basis set for Mn was originally optimised for MnO and NiO [85]; the outer d exponent was furtherly optimised for $CaMnO_3$ by changing it from 0.249 to 0.259 Bohr^{-2} [46].

The oxygen basis set is the 8-411G with principal quantum number up to $n = 4$; in the same way as Mn, it was derived in ref. [85] and optimised in ref. [46] for $CaMnO_3$; in the present calculations the value of the outer sp exponents has been changed to 0.4763 and 0.22 Bohr^{-2}.

Calcium is described by the 86-511d3G basis set originally designed for CaF_2 [132] and also used for $CaMnO_3$ [46].

Finally, the basis set used for La (976633-31G) is one optimised for La^{3+} (see footnote at page 56); it was slightly modified for the purpose of the present calculations in that the $5d$ orbital was removed from the basis and the $6sp$ and $7sp$ were replaced by a single sp orbital exponent of 0.3917 Bohr^{-2}.

What follows is the basis set input for CRYSTAL 98. The first line indicates the atomic number and the total number of shells. Shells are introduced by a line containing 5 numbers:

- type of basis set used (integer); 0 designes a general basis set given as

input

- type of shell (integer): 0 (s), 1 (sp), 2 (p) or 3 (d)
- number of contraction in the shell (integer)
- number of electrons in the shell (real)
- scale factor.

For each contraction in the shell, the values of the exponent and of the contraction coefficient are given; in the case of an sp shell an s and a p contraction coefficient are present.

Calcium (Ca) - 86-511d3G

```
20 6
0   0   8   2. 1.
  191300.          .0002204
   26970.          .001925
    5696.          .01109
    1489.          .04995
     448.3         .1701
     154.6         .3685
      60.37        .4034
      25.09        .1452
0   1   6   8. 1.
     448.6       -.00575    .00847
     105.7       -.0767     .06027
      34.69      -.1122     .2124
      13.5        .2537     .3771
```

```
       5.82      .688     .401
       1.819     .349     .198
0  1  5  8. 1.
      20.750     .0020  -.0365
       8.400    -.1255  -.0685
       3.5970   -.6960   .1570
       1.408    1.029   1.4820
       0.7260    .9440  1.0250
0  1  1  0. 1.
        .453    1.       1.
0  1  1  0. 1.
        .246    1.       1.
0  3  3  0. 1.
       3.191     .16
       0.8683    .3130
       0.3191    .4060
```

Lanthanum (La) - 976633-31G

```
57 8
0  0  9  2. 1.
 5466346.5       .0000487
  793978.        .000403
  171448.        .00231
   44597.4       .0111
   12964.8       .046
    4141.92      .1533
    1476.39      .3473
```

```
     589.139     .4339
     248.08      .2063
0  1  7  8. 1.
   16031.7      -.00037   .00111
    3742.77     -.00629   .00997
    1165.38     -.0515    .0574
     421.229    -.1462    .2169
     173.294     .0772    .4582
      81.3786    .6067    .4778
      39.822     .5197    .241
0  1  6  8. 1.
     412.647     .00653 -.0124
     153.798    -.021    -.077
      62.6774   -.3186   -.0082
      28.6625   -.0991    .8707
      13.8388    .857    1.4362
       6.8213    .4321    .5764
0  3  6  10. 1.
     457.627     .015
     135.973     .1052
      51.0043    .3295
      21.368     .4739
       9.8229    .2641
       4.8497    .0446
0  1  3  8. 1.
      10.5834    .53     -.1348
       6.5736    .3373    .3206
```

```
       3.0748    .0398    .4518
0  3  3  10. 1.
       8.9453    .2225
       3.6796    .588
       1.554     .4048
0  1  3  8. 1.
       7.6157    .2651    .0281
       2.7531    .8808    .3278
       1.3323    .4515    .2509
0  1  1  0. 1.
        .3917  1.       1.
```

Manganese (Mn) - 86-411d41G

```
25 7
0  0  8  2. 1.
  292601.        .000227
   42265.        .0019
    8947.29      .0111
    2330.32      .0501
     702.047     .1705
     242.907     .3691
      94.955     .4035
      39.5777    .1437
0  1  6  8. 1.
     732.14     -.0053    .0086
     175.551    -.0673    .0612
      58.5093   -.1293    .2135
```

```
      23.129     .2535    .4018
       9.7536    .6345    .4012
       3.4545    .2714    .2222
0  1  4  8. 1.
      38.389     .0157   -.0311
      15.4367   -.2535   -.0969
       6.1781   -.8648    .2563
       2.8235    .9337   1.6552
0  1  1  0. 1.
      1.2086    1.       1.
0  1  1  0. 1.
      .4986     1.       1.
0  3  4  4. 1.
      22.5929    .0708
       6.167     .3044
       2.0638    .5469
        .7401    .5102
0  3  1  0. 1.
       0.259    1.000
```

Oxygen (O) - 8-411G

```
8  4
0  0  8  2. 1.
    8020.        .00108
    1338.        .00804
     255.4       .05324
      69.22      .1681
```

```
        23.90       .3581
         9.264      .3855
         3.851      .1468
         1.212      .0728
0  1  4  8. 1.
        49.43     -.00883   .00958
        10.47     -.0915    .0696
         3.235    -.0402    .2065
         1.217     .3790    .3470
0  1  1  0. 1.
          .4763  1.        1.
0  1  1  0. 1.
          .220   1.        1.
```

B. Reciprocal space grid

As anticipated in Chapter 3, a fundamental issue for reciprocal space integration is the selection of the set of k-vectors in which the integration will be carried out. CRYSTAL 98 makes use of a particular grid in the irriducible Brillouin zone (IBZ) called *Monkhorst net* [114].

The Monkhorst net is defined by the basis vectors $\mathbf{b}_1/s_1$, $\mathbf{b}_2/s_2$ and $\mathbf{b}_3/s_3$, where $\mathbf{b}_1$, $\mathbf{b}_2$ and $\mathbf{b}_3$ are the ordinary reciprocal lattice vectors and s_1, s_2, s_3 are integer shrinking factors, to be given as input. For 3D crystals $s_1 = s_2 = s_3 =$ IS (CRYSTAL notation) The number of points generated depends on the symmetry of the crystal (i.e. on the number of symmetry operators for the crystal [51]) and is given asymptotically by the product of the shrinking factors divided by the order of the point group; for the same shrinking factor, systems with higher symmetry will have less points in the mesh compared to

systems with lower symmetry. The case of conductors is more complicated. Two more parameters are needed in the CRYSTAL input file: ISHF, the number of symmetrised plane waves used for representing the **k** dependence of the eigenvalues, and ISP, which defines a denser net for the evaluation of the Fermi energy and of the density matrix called *Gilat net* [133]; a suitable value for ISP would be double the one for IS.

In the case of $CaMnO_3$, for example, the space group is the cubic *Pm3m* (n. 221 in the International Tables [48]) and possesses 48 symmetry operators [51]. In a calculation on the single unit cell, IS=8 generates a Monkhorst net with 35 k-points belonging to the IBZ. For a calculation on the A-AF spin ordered structure the cell has to be doubled along one direction (e. g. z) and the two resulting Mn ions must be made inequivalent in order to allow them to have opposite spins. These two operation reduce the number of symmetry operators from 48 to 8 and, as a consequence, the same IS= 8 as before results now in 75 k points. In the case of the G-AF structure, where doubling of the cell takes place along a diagonal, the symmetry operators become 24 and 29 point are generated. What follows is the output from CRYSTAL showing, for the ground state G-AF structure, the generated k-point; they are expressed, as already specified before, in oblique (or fractional) coordinates, i. e. in the basis of the reciprocal lattice vectors, and in unit of IS. This means, for example, that the k-point

```
27-C(  6  3  1)
```

in the list below has cartesian coordinates

$$(\frac{6}{8}\mathbf{b}_1, \frac{3}{8}\mathbf{b}_2, \frac{1}{8}\mathbf{b}_3) \quad .$$

Direct and reciprocal lattice vectors are shown as well (a = 3.73 Å).

```
*** K POINTS COORDINATES (OBLIQUE COORDINATES IN UNITS OF IS =  8)
 1-R(  0  0  0)   2-C(  1  0  0)   3-C(  2  0  0)   4-C(  3  0  0)
 5-R(  4  0  0)   6-C(  1  1  0)   7-C(  2  1  0)   8-C(  3  1  0)
 9-C(  4  1  0)  10-C(  5  1  0)  11-C(  6  1  0)  12-C(  7  1  0)
13-C(  2  2  0)  14-C(  3  2  0)  15-C(  4  2  0)  16-C(  5  2  0)
17-C(  6  2  0)  18-C(  3  3  0)  19-C(  4  3  0)  20-C(  5  3  0)
21-R(  4  4  0)  22-C(  3  2  1)  23-C(  4  2  1)  24-C(  5  2  1)
25-C(  4  3  1)  26-C(  5  3  1)  27-C(  6  3  1)  28-C(  5  4  1)
29-C(  6  4  2)
*************************************************************************
DIRECT LATTICE VECTORS COMPON.(A.U.)  RECIP. LATTICE VECTORS COMPON.(A.U.)
      X          Y          Z            X          Y          Z
    .00000    7.04868    7.04868      -.44570     .44570     .44570
   7.04868     .00000    7.04868       .44570    -.44570     .44570
   7.04868    7.04868     .00000       .44570     .44570    -.44570
```

The *Pnma* structure of $LaMnO_3$ is characterised by lower symmetry compared to *Pm3m*. The A-AF case only has 4 symmetry operators and a shrinking factor of 4 results in 30 k-points. They are reported below, together with the direct and reciprocal lattice vectors (lattice parameters from the optimised *Pnma* structure).

```
*** K POINTS COORDINATES (OBLIQUE COORDINATES IN UNITS OF IS =  4)
 1-R(  0  0  0)   2-C(  1  0  0)   3-R(  2  0  0)   4-C(  0  1  0)
 5-C(  1  1  0)   6-C(  2  1  0)   7-C(  3  1  0)   8-R(  0  2  0)
 9-C(  1  2  0)  10-R(  2  2  0)  11-C(  0  0  1)  12-C(  1  0  1)
13-C(  2  0  1)  14-C(  0  1  1)  15-C(  1  1  1)  16-C(  2  1  1)
17-C(  3  1  1)  18-C(  0  2  1)  19-C(  1  2  1)  20-C(  2  2  1)
21-R(  0  0  2)  22-C(  1  0  2)  23-R(  2  0  2)  24-C(  0  1  2)
```

```
25-C(  1  1  2)  26-C(  2  1  2)  27-C(  3  1  2)  28-R(  0  2  2)
29-C(  1  2  2)  30-R(  2  2  2)
*************************************************************************
DIRECT LATTICE VECTORS COMPON.(A.U.)  RECIP. LATTICE VECTORS COMPON.(A.U.)
      X          Y          Z              X          Y          Z
  10.84703    0.00000    0.00000        0.57925    0.00000    0.00000
   0.00000   14.65294    0.00000        0.00000    0.42880    0.00000
   0.00000    0.00000   10.62027        0.00000    0.00000    0.59162
```

Freyra-Fava *et al.* [46] and Su *et al.* carried out similar UHF calculations on $CaMnO_3$ and $LaMnO_3$ respectively and they have commented on how the k-grid size affects the total energy of the system. In [46] the authors used the same grid as in the present work (IS=8, 29 k-points) for the G-AF structure; they reported that increasing IS to 12 resulted in a difference in total energy of about 2 μeV per cell. Su and co-workers used IS=6 (80 k-point) for their UHF study of *Pnma* $LaMnO_3$; they noted that the total energy difference with a 30 k-points calculation (IS=4) was less than 0.003 meV/Mn.

C. UHF Mulliken population analysis

This section reports the detailed Mulliken population analysis from the UHF calculations performed using the CRYSTAL package. The population is given for each atomic orbital and then, summed, for each shell in the basis set used (see Section A of this Appendix). The output of the program also includes the overlap population condensed to the first four neighbouring atoms.

In order to identify the sequence of atomic orbitals, it is important to recall the order used by CRYSTAL for the internal storage of *sp* and *d* orbitals [112]:

sp s, x, y, z
d $3z^2 - r^2, xz, yz, x^2 - y^2, xy$

Atomic centers in the unit cell are labelled with a sequence number in CRYSTAL. Each of the following subsections also contains the coordinates of such centers; this is needed to distinguish, for example in the case of $LaMnO_3$, in-plane and vertical oxygens.

$CaMnO_3$

G-type AF supercell

```
**** ATOMS BELONGING TO THE SUPERCEL
 ATOM  X(AU)   Y(AU)   Z(AU)
    1 CA  0.000  0.000  0.000
    2 CA  0.000  0.000 -7.049
    3 MN -3.524 -3.524 -3.524
    4 MN  3.524  3.524  3.524
    5 O   0.000  3.524  3.524
    6 O   0.000  3.524 -3.524
    7 O   3.524  0.000  3.524
    8 O   3.524  0.000 -3.524
    9 O   3.524  3.524  0.000
   10 O  -3.524 -3.524 -7.049

     ALPHA+BETA ELECTRONS
 MULLIKEN POPULATION ANALYSIS - NO. OF ELECTRONS  138.000000


  ATOM     Z CHARGE  A.O. POPULATION


   1 CA  20 18.146  2.000  1.974  2.035  2.035  2.035   .916  1.213  1.213
```

			1.213	.961	.520	.520	.520	.171	.238	.238
			.238	.017	.025	.025	.017	.025		
2	CA	20	18.146	2.000	1.974	2.035	2.035	2.035	.916	1.213	1.213
				1.213	.961	.520	.520	.520	.171	.238	.238
				.238	.017	.025	.025	.017	.025		
3	MN	25	22.863	2.000	1.898	2.057	2.057	2.057	.382	.652	.652
				.652	1.356	1.026	1.026	1.026	.408	.305	.305
				.305	.367	.968	.968	.367	.968	.339	.128
				.128	.339	.128					
4	MN	25	22.863	2.000	1.898	2.057	2.057	2.057	.382	.652	.652
				.652	1.356	1.026	1.026	1.026	.408	.305	.305
				.305	.367	.968	.968	.367	.968	.339	.128
				.128	.339	.128					
5	O	8	9.330	1.997	.491	.628	.774	.774	.946	.579	.614
				.614	.463	.389	.531	.531			
6	O	8	9.330	1.997	.491	.628	.774	.774	.946	.579	.614
				.614	.463	.389	.531	.531			
7	O	8	9.330	1.997	.491	.774	.628	.774	.946	.614	.579
				.614	.463	.531	.389	.531			
8	O	8	9.330	1.997	.491	.774	.628	.774	.946	.614	.579
				.614	.463	.531	.389	.531			
9	O	8	9.330	1.997	.491	.774	.774	.628	.946	.614	.614
				.579	.463	.531	.531	.389			
10	O	8	9.330	1.997	.491	.774	.774	.628	.946	.614	.614
				.579	.463	.531	.531	.389			

ATOM Z CHARGE SHELL POPULATION

1	CA	20	18.146	2.000	8.079	4.557	2.519	.884	.108
2	CA	20	18.146	2.000	8.079	4.557	2.519	.884	.108
3	MN	25	22.863	2.000	8.069	2.337	4.433	1.324	3.637 1.062
4	MN	25	22.863	2.000	8.069	2.337	4.433	1.324	3.637 1.062
5	O	8	9.330	1.997	2.666	2.754	1.914		
6	O	8	9.330	1.997	2.666	2.754	1.914		
7	O	8	9.330	1.997	2.666	2.754	1.914		
8	O	8	9.330	1.997	2.666	2.754	1.914		
9	O	8	9.330	1.997	2.666	2.754	1.914		
10	O	8	9.330	1.997	2.666	2.754	1.914		

OVERLAP POPULATION CONDENSED TO ATOMS FOR FIRST 4 NEIGHBORS

ATOM A	1 CA	ATOM B	CELL	R(AB)/AU	R(AB)/ANG	OVPOP(AB)
		1 CA	(0 0 0)	.000	.000	18.157
		10 O	(1 0 0)	4.984	2.638	-.001
		4 MN	(0 0 0)	6.104	3.230	.000
		2 CA	(0 0 0)	7.049	3.730	.000

ATOM A	2 CA	ATOM B	CELL	R(AB)/AU	R(AB)/ANG	OVPOP(AB)
		2 CA	(0 0 0)	.000	.000	18.157
		7 O	(-1 -1 1)	4.984	2.638	-.001
		4 MN	(-1 0 0)	6.104	3.230	.000
		1 CA	(0 0 0)	7.049	3.730	.000

ATOM A	3 MN	ATOM B	CELL	R(AB)/AU	R(AB)/ANG	OVPOP(AB)

```
                     3 MN   (  0  0  0)      .000      .000    22.440
                    10 O    (  0  0  0)     3.524     1.865      .074
                     2 CA   (  0  0  0)     6.104     3.230      .000
                     4 MN   ( -1  0  0)     7.049     3.730     -.003

ATOM A   4 MN    ATOM B       CELL       R(AB)/AU R(AB)/ANG   OVPOP(AB)
                     4 MN   (  0  0  0)      .000      .000    22.440
                    10 O    (  1  1  0)     3.524     1.865      .074
                     2 CA   (  1  0  0)     6.104     3.230      .000
                     3 MN   (  1  0  0)     7.049     3.730     -.003

ATOM A   5 O     ATOM B       CELL       R(AB)/AU R(AB)/ANG   OVPOP(AB)
                     5 O    (  0  0  0)      .000      .000     9.332
                     4 MN   (  0  0  0)     3.524     1.865      .074
                    10 O    (  1  1  0)     4.984     2.638     -.016
                     1 CA   (  0  0  0)     4.984     2.638     -.001
MMMMMMMMMMMMMMMMMMMMMMMMMMMMMMMMMMMMMMMMMMMMMMMMMMMMMMMMMMMMMMMMMMMMMMMMMMMMMM
    ALPHA-BETA ELECTRONS
 MULLIKEN POPULATION ANALYSIS - NO. OF ELECTRONS      .000000


 ATOM    Z CHARGE  A.O. POPULATION

  1 CA  20   .000   .000   .000   .000   .000   .000   .000   .000   .000
                    .000   .000   .000   .000   .000   .000   .000   .000
                    .000   .000   .000   .000   .000   .000
  2 CA  20   .000   .000   .000   .000   .000   .000   .000   .000   .000
                    .000   .000   .000   .000   .000   .000   .000   .000
```

			.000	.000	.000	.000	.000	.000		
3	MN	25	3.230	.000	.002	-.002	-.002	-.002	.000	.008	.008
				.008	.010	.008	.008	.008	.000	-.006	-.006
				-.006	.154	.909	.909	.154	.909	.048	.022
				.022	.048	.022					
4	MN	25	-3.230	.000	-.002	.002	.002	.002	.000	-.008	-.008
				-.008	-.010	-.008	-.008	-.008	.000	.006	.006
				.006	-.154	-.909	-.909	-.154	-.909	-.048	-.022
				-.022	-.048	-.022					
5	O	8	.000	.000	.000	.000	.000	.000	.000	.000	.000
				.000	.000	.000	.000	.000			
6	O	8	.000	.000	.000	.000	.000	.000	.000	.000	.000
				.000	.000	.000	.000	.000			
7	O	8	.000	.000	.000	.000	.000	.000	.000	.000	.000
				.000	.000	.000	.000	.000			
8	O	8	.000	.000	.000	.000	.000	.000	.000	.000	.000
				.000	.000	.000	.000	.000			
9	O	8	.000	.000	.000	.000	.000	.000	.000	.000	.000
				.000	.000	.000	.000	.000			
10	O	8	.000	.000	.000	.000	.000	.000	.000	.000	.000
				.000	.000	.000	.000	.000			

ATOM		Z	CHARGE	SHELL	POPULATION				
1	CA	20	.000	.000	.000	.000	.000	.000	.000
2	CA	20	.000	.000	.000	.000	.000	.000	.000
3	MN	25	3.230	.000	-.003	.023	.033	-.020	3.034	.162

4 MN	25	-3.230	.000	.003	-.023	-.033	.020	-3.034	-.162
5 O	8	.000	.000	.000	.000	.000			
6 O	8	.000	.000	.000	.000	.000			
7 O	8	.000	.000	.000	.000	.000			
8 O	8	.000	.000	.000	.000	.000			
9 O	8	.000	.000	.000	.000	.000			
10 O	8	.000	.000	.000	.000	.000			

OVERLAP POPULATION CONDENSED TO ATOMS FOR FIRST 4 NEIGHBORS

ATOM A	1 CA	ATOM B	CELL	R(AB)/AU	R(AB)/ANG	OVPOP(AB)
		1 CA	(0 0 0)	.000	.000	.000
		10 O	(1 0 0)	4.984	2.638	.000
		4 MN	(0 0 0)	6.104	3.230	.000
		2 CA	(0 0 0)	7.049	3.730	.000

ATOM A	2 CA	ATOM B	CELL	R(AB)/AU	R(AB)/ANG	OVPOP(AB)
		2 CA	(0 0 0)	.000	.000	.000
		7 O	(-1 -1 1)	4.984	2.638	.000
		4 MN	(-1 0 0)	6.104	3.230	.000
		1 CA	(0 0 0)	7.049	3.730	.000

ATOM A	3 MN	ATOM B	CELL	R(AB)/AU	R(AB)/ANG	OVPOP(AB)
		3 MN	(0 0 0)	.000	.000	3.374
		10 O	(0 0 0)	3.524	1.865	-.024
		2 CA	(0 0 0)	6.104	3.230	.000
		4 MN	(-1 0 0)	7.049	3.730	.000

ATOM A	4 MN	ATOM B	CELL	R(AB)/AU	R(AB)/ANG	OVPOP(AB)
		4 MN	(0 0 0)	.000	.000	-3.374
		10 O	(1 1 0)	3.524	1.865	.024
		2 CA	(1 0 0)	6.104	3.230	.000
		3 MN	(1 0 0)	7.049	3.730	.000

ATOM A	5 O	ATOM B	CELL	R(AB)/AU	R(AB)/ANG	OVPOP(AB)
		5 O	(0 0 0)	.000	.000	.000
		4 MN	(0 0 0)	3.524	1.865	.024
		10 O	(1 1 0)	4.984	2.638	-.005
		1 CA	(0 0 0)	4.984	2.638	.000

$LaMnO_3$

A-type AF supercell

ATOM	X(AU)	Y(AU)	Z(AU)
1 LA	-5.239	3.663	0.011
2 LA	-0.184	-3.663	-5.300
3 LA	0.184	3.663	5.300
4 LA	5.239	-3.663	-0.011
5 MN	0.000	0.000	0.000
6 MN	-5.424	0.000	-5.310
7 MN	-5.424	-7.326	-5.310
8 MN	0.000	-7.326	0.000
9 O	-0.022	3.663	-0.287
10 O	-5.402	-3.663	5.023
11 O	5.402	3.663	-5.023

12	O	0.022	-3.663	0.287
13	O	3.146	0.205	2.517
14	O	2.278	-0.205	-2.793
15	O	-2.278	7.121	2.793
16	O	-3.146	-7.121	-2.517
17	O	-3.146	-0.205	-2.517
18	O	-2.278	0.205	2.793
19	O	2.278	-7.121	-2.793
20	O	3.146	7.121	2.517

ALPHA+BETA ELECTRONS

MULLIKEN POPULATION ANALYSIS - NO. OF ELECTRONS 424.000000

ATOM	Z	CHARGE	A.O. POPULATION							
1 LA	57	53.851	1.999	2.052	1.999	1.999	1.999	1.752	1.998	1.998
			1.998	2.000	2.000	2.000	2.000	2.000	0.063	0.891
			0.892	0.892	1.999	1.999	1.999	1.999	1.999	2.137
			1.170	1.170	1.170	1.964	1.904	1.902	1.904	
2 LA	57	53.851	1.999	2.052	1.999	1.999	1.999	1.752	1.998	1.998
			1.998	2.000	2.000	2.000	2.000	2.000	0.063	0.891
			0.892	0.892	1.999	1.999	1.999	1.999	1.999	2.137
			1.170	1.170	1.170	1.964	1.904	1.902	1.904	
3 LA	57	53.851	1.999	2.052	1.999	1.999	1.999	1.752	1.998	1.998
			1.998	2.000	2.000	2.000	2.000	2.000	0.063	0.891
			0.892	0.892	1.999	1.999	1.999	1.999	1.999	2.137
			1.170	1.170	1.170	1.964	1.904	1.902	1.904	
4 LA	57	53.851	1.999	2.052	1.999	1.999	1.999	1.752	1.998	1.998

			1.998	2.000	2.000	2.000	2.000	2.000	0.063	0.891
			0.892	0.892	1.999	1.999	1.999	1.999	1.999	2.137
			1.170	1.170	1.170	1.964	1.904	1.902	1.904	
5	MN	25 22.749	2.000	1.899	2.059	2.058	2.059	0.375	0.628	0.633
			0.631	1.330	1.016	1.019	1.017	0.426	0.315	0.311
			0.314	0.762	0.719	0.931	0.677	0.935	0.129	0.151
			0.102	0.155	0.100					
6	MN	25 22.749	2.000	1.899	2.059	2.058	2.059	0.375	0.628	0.633
			0.631	1.330	1.016	1.019	1.017	0.426	0.315	0.311
			0.314	0.762	0.719	0.931	0.677	0.935	0.129	0.151
			0.102	0.155	0.100					
7	MN	25 22.749	2.000	1.899	2.059	2.058	2.059	0.375	0.628	0.633
			0.631	1.330	1.016	1.019	1.017	0.426	0.315	0.311
			0.314	0.762	0.719	0.931	0.677	0.935	0.129	0.151
			0.102	0.155	0.100					
8	MN	25 22.749	2.000	1.899	2.059	2.058	2.059	0.375	0.628	0.633
			0.631	1.330	1.016	1.019	1.017	0.426	0.315	0.311
			0.314	0.762	0.719	0.931	0.677	0.935	0.129	0.151
			0.102	0.155	0.100					
9	O	8 9.762	1.997	0.504	0.758	0.689	0.762	0.785	0.457	0.525
			0.461	0.692	0.774	0.593	0.766			
10	O	8 9.762	1.997	0.504	0.758	0.689	0.762	0.785	0.457	0.525
			0.461	0.692	0.774	0.593	0.766			
11	O	8 9.762	1.997	0.504	0.758	0.689	0.762	0.785	0.457	0.525
			0.461	0.692	0.774	0.593	0.766			
12	O	8 9.762	1.997	0.504	0.758	0.689	0.762	0.785	0.457	0.525
			0.461	0.692	0.774	0.593	0.766			

13 O	8	9.818	1.997	0.508	0.726	0.760	0.721	0.766	0.470	0.453
			0.475	0.726	0.731	0.783	0.703			
14 O	8	9.818	1.997	0.508	0.726	0.760	0.721	0.766	0.470	0.453
			0.475	0.726	0.731	0.783	0.703			
15 O	8	9.818	1.997	0.508	0.726	0.760	0.721	0.766	0.470	0.453
			0.475	0.726	0.731	0.783	0.703			
16 O	8	9.818	1.997	0.508	0.726	0.760	0.721	0.766	0.470	0.453
			0.475	0.726	0.731	0.783	0.703			
17 O	8	9.818	1.997	0.508	0.726	0.760	0.721	0.766	0.470	0.453
			0.475	0.726	0.731	0.783	0.703			
18 O	8	9.818	1.997	0.508	0.726	0.760	0.721	0.766	0.470	0.453
			0.475	0.726	0.731	0.783	0.703			
19 O	8	9.818	1.997	0.508	0.726	0.760	0.721	0.766	0.470	0.453
			0.475	0.726	0.731	0.783	0.703			
20 O	8	9.818	1.997	0.508	0.726	0.760	0.721	0.766	0.470	0.453
			0.475	0.726	0.731	0.783	0.703			

ATOM	Z	CHARGE	SHELL POPULATION							
1 LA	57	53.851	1.999	8.050	7.747	10.000	2.739	9.996	5.646	7.674
2 LA	57	53.851	1.999	8.050	7.747	10.000	2.739	9.996	5.646	7.674
3 LA	57	53.851	1.999	8.050	7.747	10.000	2.739	9.996	5.646	7.674
4 LA	57	53.851	1.999	8.050	7.747	10.000	2.739	9.996	5.646	7.674
5 MN	25	22.749	2.000	8.074	2.267	4.382	1.366	4.024	0.636	
6 MN	25	22.749	2.000	8.074	2.267	4.382	1.366	4.024	0.636	
7 MN	25	22.749	2.000	8.074	2.267	4.382	1.366	4.024	0.636	
8 MN	25	22.749	2.000	8.074	2.267	4.382	1.366	4.024	0.636	

9	O	8	9.762	1.997	2.712	2.228	2.825
10	O	8	9.762	1.997	2.712	2.228	2.825
11	O	8	9.762	1.997	2.712	2.228	2.825
12	O	8	9.762	1.997	2.712	2.228	2.825
13	O	8	9.818	1.997	2.716	2.163	2.943
14	O	8	9.818	1.997	2.716	2.163	2.943
15	O	8	9.818	1.997	2.716	2.163	2.943
16	O	8	9.818	1.997	2.716	2.163	2.943
17	O	8	9.818	1.997	2.716	2.163	2.943
18	O	8	9.818	1.997	2.716	2.163	2.943
19	O	8	9.818	1.997	2.716	2.163	2.943
20	O	8	9.818	1.997	2.716	2.163	2.943

OVERLAP POPULATION CONDENSED TO ATOMS FOR FIRST 4 NEIGHBORS

ATOM A	1 LA	ATOM B	CELL	R(AB)/AU	R(AB)/ANG	OVPOP(AB)
		1 LA	(0 0 0)	0.000	0.000	53.901
		13 O	(-1 0 0)	4.930	2.609	-0.015
		11 O	(-1 0 0)	5.038	2.666	-0.008
		16 O	(0 1 0)	5.073	2.685	-0.007

ATOM A	5 MN	ATOM B	CELL	R(AB)/AU	R(AB)/ANG	OVPOP(AB)
		5 MN	(0 0 0)	0.000	0.000	22.685
		18 O	(0 0 0)	3.610	1.910	0.030
		12 O	(0 0 0)	3.675	1.944	0.016
		13 O	(0 0 0)	4.034	2.135	-0.011

ATOM A 7 MN	ATOM B	CELL	R(AB)/AU	R(AB)/ANG	OVPOP(AB)
	7 MN	(0 0 0)	0.000	0.000	22.685
	16 O	(0 0 0)	3.610	1.910	0.030
	11 O	(-1 -1 0)	3.675	1.944	0.016
	19 O	(-1 0 0)	4.034	2.135	-0.011

ATOM A 9 O	ATOM B	CELL	R(AB)/AU	R(AB)/ANG	OVPOP(AB)
	9 O	(0 0 0)	0.000	0.000	9.757
	8 MN	(0 1 0)	3.675	1.944	0.016
	3 LA	(0 0 -1)	5.038	2.666	-0.008
	19 O	(0 1 0)	5.151	2.726	0.000

ATOM A 13 O	ATOM B	CELL	R(AB)/AU	R(AB)/ANG	OVPOP(AB)
	13 O	(0 0 0)	0.000	0.000	9.850
	6 MN	(1 0 1)	3.610	1.910	0.030
	5 MN	(0 0 0)	4.034	2.135	-0.011
	1 LA	(1 0 0)	4.930	2.609	-0.015

ATOM A 15 O	ATOM B	CELL	R(AB)/AU	R(AB)/ANG	OVPOP(AB)
	15 O	(0 0 0)	0.000	0.000	9.850
	8 MN	(0 1 0)	3.610	1.910	0.030
	7 MN	(0 1 1)	4.034	2.135	-0.011
	3 LA	(0 0 0)	4.930	2.609	-0.015

MMMMMMMMMMMMMMMMMMMMMMMMMMMMMMMMMMMMMMMMMMMMMMMMMMMMMMMMMMMMMMMMMMMMMMMMMMMMMMMM

ALPHA-BETA ELECTRONS

MULLIKEN POPULATION ANALYSIS - NO. OF ELECTRONS 0.000000

ATOM	Z	CHARGE	A.O. POPULATION							
1 LA	57	0.000	0.000	0.000	0.000	0.000	0.000	0.000	0.000	0.000
			0.000	0.000	0.000	0.000	0.000	0.000	0.000	0.000
			0.000	0.000	0.000	0.000	0.000	0.000	0.000	0.000
			0.000	0.000	0.000	0.000	0.000	0.000	0.000	
2 LA	57	0.000	0.000	0.000	0.000	0.000	0.000	0.000	0.000	0.000
			0.000	0.000	0.000	0.000	0.000	0.000	0.000	0.000
			0.000	0.000	0.000	0.000	0.000	0.000	0.000	0.000
			0.000	0.000	0.000	0.000	0.000	0.000	0.000	
3 LA	57	0.000	0.000	0.000	0.000	0.000	0.000	0.000	0.000	0.000
			0.000	0.000	0.000	0.000	0.000	0.000	0.000	0.000
			0.000	0.000	0.000	0.000	0.000	0.000	0.000	0.000
			0.000	0.000	0.000	0.000	0.000	0.000	0.000	
4 LA	57	0.000	0.000	0.000	0.000	0.000	0.000	0.000	0.000	0.000
			0.000	0.000	0.000	0.000	0.000	0.000	0.000	0.000
			0.000	0.000	0.000	0.000	0.000	0.000	0.000	0.000
			0.000	0.000	0.000	0.000	0.000	0.000	0.000	
5 MN	25	3.958	0.000	0.002	-0.002	-0.002	-0.002	-0.001	0.006	0.007
			0.006	0.010	0.012	0.011	0.011	-0.003	-0.013	-0.012
			-0.011	0.706	0.621	0.902	0.586	0.909	0.053	0.019
			0.053	0.030	0.056					
6 MN	25	3.958	0.000	0.002	-0.002	-0.002	-0.002	-0.001	0.006	0.007
			0.006	0.010	0.012	0.011	0.011	-0.003	-0.013	-0.012
			-0.011	0.706	0.621	0.902	0.586	0.909	0.053	0.019
			0.053	0.030	0.056					
7 MN	25	-3.958	0.000	-0.002	0.002	0.002	0.002	0.001	-0.006	-0.007

			-0.006	-0.010	-0.012	-0.011	-0.011	0.003	0.013	0.012
			0.011	-0.706	-0.621	-0.902	-0.586	-0.909	-0.053	-0.019
			-0.053	-0.030	-0.056					
8	MN	25 -3.958	0.000	-0.002	0.002	0.002	0.002	0.001	-0.006	-0.007
			-0.006	-0.010	-0.012	-0.011	-0.011	0.003	0.013	0.012
			0.011	-0.706	-0.621	-0.902	-0.586	-0.909	-0.053	-0.019
			-0.053	-0.030	-0.056					
9	0	8 0.000	0.000	0.000	0.000	0.000	0.000	0.000	0.000	0.000
			0.000	0.000	0.000	0.000	0.000			
10	0	8 0.000	0.000	0.000	0.000	0.000	0.000	0.000	0.000	0.000
			0.000	0.000	0.000	0.000	0.000			
11	0	8 0.000	0.000	0.000	0.000	0.000	0.000	0.000	0.000	0.000
			0.000	0.000	0.000	0.000	0.000			
12	0	8 0.000	0.000	0.000	0.000	0.000	0.000	0.000	0.000	0.000
			0.000	0.000	0.000	0.000	0.000			
13	0	8 0.017	0.000	0.003	0.010	0.015	-0.002	0.004	0.002	0.008
			-0.005	-0.004	-0.004	-0.008	-0.001			
14	0	8 0.017	0.000	0.003	0.010	0.015	-0.002	0.004	0.002	0.008
			-0.005	-0.004	-0.004	-0.008	-0.001			
15	0	8 -0.017	0.000	-0.003	-0.010	-0.015	0.002	-0.004	-0.002	-0.008
			0.005	0.004	0.004	0.008	0.001			
16	0	8 -0.017	0.000	-0.003	-0.010	-0.015	0.002	-0.004	-0.002	-0.008
			0.005	0.004	0.004	0.008	0.001			
17	0	8 0.017	0.000	0.003	0.010	0.015	-0.002	0.004	0.002	0.008
			-0.005	-0.004	-0.004	-0.008	-0.001			
18	0	8 0.017	0.000	0.003	0.010	0.015	-0.002	0.004	0.002	0.008
			-0.005	-0.004	-0.004	-0.008	-0.001			

19 O	8	-0.017	0.000	-0.003	-0.010	-0.015	0.002	-0.004	-0.002	-0.008
			0.005	0.004	0.004	0.008	0.001			
20 O	8	-0.017	0.000	-0.003	-0.010	-0.015	0.002	-0.004	-0.002	-0.008
			0.005	0.004	0.004	0.008	0.001			

ATOM	Z	CHARGE	SHELL POPULATION							
1 LA	57	0.000	0.000	0.000	0.000	0.000	0.000	0.000	0.000	0.000
2 LA	57	0.000	0.000	0.000	0.000	0.000	0.000	0.000	0.000	0.000
3 LA	57	0.000	0.000	0.000	0.000	0.000	0.000	0.000	0.000	0.000
4 LA	57	0.000	0.000	0.000	0.000	0.000	0.000	0.000	0.000	0.000
5 MN	25	3.958	0.000	-0.003	0.018	0.045	-0.039	3.724	0.212	
6 MN	25	3.958	0.000	-0.003	0.018	0.045	-0.039	3.724	0.212	
7 MN	25	-3.958	0.000	0.003	-0.018	-0.045	0.039	-3.724	-0.212	
8 MN	25	-3.958	0.000	0.003	-0.018	-0.045	0.039	-3.724	-0.212	
9 O	8	0.000	0.000	0.000	0.000	0.000				
10 O	8	0.000	0.000	0.000	0.000	0.000				
11 O	8	0.000	0.000	0.000	0.000	0.000				
12 O	8	0.000	0.000	0.000	0.000	0.000				
13 O	8	0.017	0.000	0.025	0.009	-0.018				
14 O	8	0.017	0.000	0.025	0.009	-0.018				
15 O	8	-0.017	0.000	-0.025	-0.009	0.018				
16 O	8	-0.017	0.000	-0.025	-0.009	0.018				
17 O	8	0.017	0.000	0.025	0.009	-0.018				
18 O	8	0.017	0.000	0.025	0.009	-0.018				
19 O	8	-0.017	0.000	-0.025	-0.009	0.018				
20 O	8	-0.017	0.000	-0.025	-0.009	0.018				

OVERLAP POPULATION CONDENSED TO ATOMS FOR FIRST 4 NEIGHBORS

ATOM A		ATOM B	CELL	R(AB)/AU	R(AB)/ANG	OVPOP(AB)
1 LA		1 LA	(0 0 0)	0.000	0.000	0.000
		13 O	(-1 0 0)	4.930	2.609	0.000
		11 O	(-1 0 0)	5.038	2.666	0.000
		16 O	(0 1 0)	5.073	2.685	0.000
ATOM A		ATOM B	CELL	R(AB)/AU	R(AB)/ANG	OVPOP(AB)
5 MN		5 MN	(0 0 0)	0.000	0.000	4.146
		18 O	(0 0 0)	3.610	1.910	-0.026
		12 O	(0 0 0)	3.675	1.944	-0.032
		13 O	(0 0 0)	4.034	2.135	-0.038
ATOM A		ATOM B	CELL	R(AB)/AU	R(AB)/ANG	OVPOP(AB)
7 MN		7 MN	(0 0 0)	0.000	0.000	-4.146
		16 O	(0 0 0)	3.610	1.910	0.026
		11 O	(-1 -1 0)	3.675	1.944	0.032
		19 O	(-1 0 0)	4.034	2.135	0.038
ATOM A		ATOM B	CELL	R(AB)/AU	R(AB)/ANG	OVPOP(AB)
9 O		9 O	(0 0 0)	0.000	0.000	0.000
		8 MN	(0 1 0)	3.675	1.944	0.032
		3 LA	(0 0 -1)	5.038	2.666	0.000
		19 O	(0 1 0)	5.151	2.726	-0.006

ATOM A	13 O	ATOM B	CELL	R(AB)/AU	R(AB)/ANG	OVPOP(AB)
		13 O	(0 0 0)	0.000	0.000	0.079
		6 MN	(1 0 1)	3.610	1.910	-0.026
		5 MN	(0 0 0)	4.034	2.135	-0.038
		1 LA	(1 0 0)	4.930	2.609	0.000

ATOM A	15 O	ATOM B	CELL	R(AB)/AU	R(AB)/ANG	OVPOP(AB)
		15 O	(0 0 0)	0.000	0.000	-0.079
		8 MN	(0 1 0)	3.610	1.910	0.026
		7 MN	(0 1 1)	4.034	2.135	0.038
		3 LA	(0 0 0)	4.930	2.609	0.000

Bibliography

[1] G. H. Jonker and K. H. van Santen, *Physica* (Amsterdam) **16**, 337 (1950)

[2] K. H. van Santen and G. H. Jonker, *Physica* (Amsterdam) **16**, 599 (1950)

[3] J. M. D. Coey, M. Viret and S. von Molnár, *Adv. Phys.*, **48**, 167 (1999)

[4] M. B. Salamon and M. Jaime, *Rev. Mod. Phys.*, **73**, 583 (2001)

[5] A. P. Ramirez, *J. Phys. Cond. Mat.*, **9**, 8171 (1997)

[6] M. Imada, A. Fujimori, Y. Tokura, *Rev. Mod. Phys.*, **70**, 1039 (1998)

[7] Y. Tokura, Y. Tomioka, *J. Magn. Magn. Mat.*, **200**, 1 (1999)

[8] R.W.G. Wyckoff, *Crystal Structures*, 2nd ed. (Interscience, New York, 1963)

[9] V. Goldsmith, *Geochemistry*, Oxford University Press (1958)

[10] C. W. Searle and S. T. Wang, *Can. J. Phys.*, **48**, 2023 (1970)

[11] S. Jin et al., *J. Appl. Phys.*, **76** (1994)

[12] A.J. Millis, P. B. littlewood and B. I. Shraiman, *Phys. Rev. Lett.*, **74** 5144 (1995)

[13] Uehara, Kim and Cheong, Rutgers University (http://www.physics.rutgers.edu/~gersh/cmr.htm)

[14] C. H. Chen and S. W. Cheong, *Phys. Rev. B*, **76**, 4042 (1996)

[15] H.A Jahn and E. Teller, *Proc. Roy. Soc.* **A161**, 220 (1937)

[16] H.A Jahn, *Proc. Roy. Soc.* **A164**, 117 (1937)

[17] D. I. Khomskii, *Electronic Structure, Exchange and Magnetism in Oxides* in "Spin Electronics" M. Ziese, M. J. Thornton eds., *Lecture Notes in Physics*, Springer-Verlag (2001)

[18] J. Volger, *Physica* (Amsterdam) **20**, 49 (1954)

[19] G. H Jonker, *Physica* (Amsterdam) **20**, 1118 (1954)

[20] E.O. Wollan and W.C. Koehler, *Phys. Rev.*, **100** 545 (1955)

[21] P. Shiffer et al., *Phys. Rev. Lett.*, **75**, 3336 (1995)

[22] P.W. Anderson, *Phys. Rev.*, **79**, 350 (1950)

[23] H.A. Kramers, *Physica* **1**, 182 (1934)

[24] Zener C., *Phys. Rev.*, **81** 440 (1951)

[25] P.W. Anderson and H. Hasegawa, *Phys. Rev.*, **100**, 675 (1955)

[26] P. G. DeGennes, *Phys. Rev.*, **118**, 141, (1960)

[27] K. Kubo and N. Ohata, *J. Phys. Soc. Jpn.*, **33**, 21 (1972)

[28] R. M. Kusters et al., *Physica* (Amsterdam), **155B**, 362 (1989)

[29] J. H. de Boer and A. J. W. Verway, *Proc. Phys. Soc. London* Ser. A, **49**, 59 (1937)

[30] R. Peierls, *Proc. Phys. Soc. London* Ser. A, **49**, 72 (1937)

[31] N. F. Mott, *Proc. Phys. Soc. London* Ser. A, **49**, 72 (1937)

[32] N. F. Mott, *Proc. Phys. Soc. London* Ser. A, **62**, 416 (1949)

[33] N. F. Mott, *Can. J. Phys.*, **34**, 1356 (1956)

[34] N. F. Mott, *Phylos. Mag.*, **6**, 287 (1961)

[35] N. F. Mott, *Metal-Insulator Transitions*, Tailor and Francis, London-Philadelphia (1990)

[36] P.W. Anderson, *Phys. Rev.*, **115**, 2 (1959)

[37] J. Hubbard, *Proc. R. Soc. London, Ser. A*, **276**, 238 (1963);

[38] J. Hubbard, *Proc. R. Soc. London, Ser. A*, **277**, 237 (1964);

[39] J. Hubbard, *Proc. R. Soc. London, Ser. A*, **281**, 401 (1964);

[40] J. Kanamori, *Prog. Theor. Phys.*, **30**, 275 (1963)

[41] D. I. Khomskii, *The Phys. of Metals and Metallography*, **29**, 31 (1970)

[42] J. B. MacChesney *et al.*, *Phys. Rev.*, **164**, 779 (1967)

[43] K. R. Poppelmeier *et al.*, *J. Solid State Chem.*, **45**, 71 (1982)

[44] W.E. Pickett and D.J. Singh, *Phys. Rev. B*, **53**, 1146 (1996)

[45] S. Satpathy et al., *Phys. Rev. Lett.*, **76**, 960 (1996)

[46] F. Freyria-Fava, Ph. D'Arco, R. Orlando and R. Dovesi, *J. Phys. Cond. Matt.*, **9**, 489 (1997)

[47] J.B.A.A. Elemans et al., *J. Solid State Chem.*, **3**, 238 (1971)

[48] *International Tables for Crystallography*, Vol. **A**, T. Hahn Ed., D. Reidel Pub. Co., Boston (1983, 1987)

[49] S. Geller, *J. Chem. Phys.*, **24**, 1236 (1956); *Acta Crystallogr.*, **10**, 248 (1957)

[50] T. Mizokawa and A. Fujimori, *Phys. Rev. B*, **54**, 5368 (1996)

[51] C. J. Bradley and A. P. Cracknell, *The Mathematical Theory of Symmetry in Solids*, Clarendon Press, Oxford (1972)

[52] S. Sasaki et al., *Acta Crystallogr.*, **43**, 1668 (1987)

[53] Murakami et al, *Phys. Rev. Lett.*, **81**, 582 (1998)

[54] J. Rodriguez-Carvajal et al., *Phys. Rev. B*, **57**, R3189 (1998)

[55] D.D. Sarma et al., *Phys. Rev. Lett.*, **75**, 1126 (1995)

[56] R. Mahendiran et al., *Appl. Phys. Lett.*, **66**, 233 (1995)

[57] A. Chainani et al., *Phys. Rev. B*, **47**, 15397 (1993)

[58] Yen-Sheng Su et al, *Phys. Rev. B*, **61**, 1324 (2000)

[59] T. Saitoh et al., *Phys. Rev. B*, **51**, 13942 (1995)

[60] J. Z. Liu et al., *Appl. Phys. Lett.*, **66**, 3218 (1995)

[61] J. F. Lawler, J. G. Lunney and J. M. D. Coey, *Appl. Phys. Lett.*, **65**, 3017 (1994)

[62] J. F. Lawler and J. M. D. Coey, *J. Magn. Magn. Mat.*, **140-144**, 2049 (1995)

[63] L. Sheng et al., *Phys. Rev. B*, **56**, R7053 (1997)

[64] P. G. Radaelli et al., *Phys. Rev. B*, **55**, 3015 (1997)

[65] S. Mori et al., *Phys. Rev. Lett.*, **81**, 3972 (1998)

[66] K.H.Ahn and A.J. Millis, *Phys. Rev. B*, **58**, 3697 (1998)

[67] J.B. Goodenough, *Phys. Rev.*, **100**, 564 (1955)

[68] G.S. Rushbrook, G.A. Baker and P.J. Wood, in *Phase Transitions and Citical Phenomena* Vol. 3, edited by C. Domb and M.S. Green (Academic, New York, 1974)

[69] F. Moussa et al., *Phys. Rev. B*, **54**, 15149 (1996)

[70] F. Moussa et al., *Phys. Rev. B*, **60**, 1 (1999)

[71] K. Hirota, N. Kaneko, A. Nishizawa and Y. Endoh, *J. Phys. Soc. Jpn.*, **65**, 3736 (1996)

[72] I. Solovyev, N. Hamada and K. Terakura, *Phys. Rev. Lett.*, **76**, 4825 (1996)

[73] A.J. Millis, *Phys. Rev. B*, **55**, 6405 (1997)

[74] Feiner and Oleś, *Phys. Rev. B*, **59**,

[75] H. Meskine, H. König and S. Satpathy, *Phys. Rev. B*, **64**, 94433 (2001) 3295 (1999)

[76] C. Pisani, *Ab-Initio Approaches to the Quantum-Mechanical Treatment of Periodic Systems* in "Quantum-Mechanical Ab-initio Calculation of the Properties of Crystalline Materials" C. Pisani ed., *Lecture Notes in Chemistry*, vol. **67**, Springer-Verlag (1996)

[77] A. Szabo, N. S. Ostlund, *Moderm Quantum Chemistry: Introduction to Advanced Electronic Structure Theory*, McMillan, New York (1982)

[78] N.M. Harrison, V.R. Saunders, R.Dovesi, W.C. Mackrodt, *Philosophical Transactions of the Royal Society of London, Series A: Mathematical, Physical and Engeneering Sciences*, n. 1735, vol. **356**, 75 (1998)

[79] C. Pisani, R. Dovesi, C. Roetti, *Hartree-Fock Ab Initio Treatment of Crystalline Systems*, Lecture Notes in Chemistry, Vol. **48**, Springer Verlag, Heidelberg (1988)

[80] http://www.chimifm.unito.it/teorica/crystal/crystal.html; http://www.cse.dl.ac.uk/Activity/CRYSTAL/

[81] R. G. Parr and W. Yang, *Density Functional Theory of Atoms and Molecules*, Oxford University Press, Oxford (1989)

[82] J. P. Perdew and S. Kurth in *Density Functionals: Theory and Applications*, D. Joubert Ed., Springer, Berlin (1998)

[83] M. L. Cohen in *Structure and Bonding in Crystals*, Vol. I (M. O'Keeffe and A. Navrotsky eds.), Academic, New York, p. 25 (1981)

[84] W. C. Mackrodt et al., *Phil. Magazine A*, **68**, 653 (1993)

[85] M. D. Towler et al., *Phys. Rev. B*, **50**, 5041 (1994)

[86] D. R. Hartree, *Proc. Camb. Philos. Soc.*, **24**, 89 (1928)

[87] D. R. Hartree, *The Calculation of Atomic Structures*, Wiley Interscience, New York (1957)

[88] V. A. Fock, *Z. Phys.*, **61**, 126 (1930); V. A. Fock, *Z. Phys.*, **62**, 795 (1930)

[89] N. W. Ashcroft and N. D. Mermin, *Solid State Physics*, Saunders College Publishing (1976)

[90] P. Fulde, *Electron Correlations in Molecules and Solids*, Solid State Sciences, Vol. 100, Springer, Berlin (1993)

[91] L. Hedin, *Phys. Rev*, **139**, A796 (1965)

[92] H.J Monkhorst, *Phys. Rev. B*, **20**, 1504 (1979); J. Delhalle and J. L. Calais, *J. Chem. Phys.*, **45**, 5286 (1986)

[93] E. Aprà, *Hartree-Fock Treatment of Spin-Polarized Crystals* in "Quantum-Mechanical Ab-initio Calculation of the Properties of Crystalline Materials" C. Pisani ed., *Lecture Notes in Chemistry*, vol. **67**, Springer-Verlag (1996)

[94] P. Hohenberg and W. Kohn, *Phys. Rev.*, **136**, B864 (1964)

[95] W. Kohn and L.J. Sham, *Phys. Rev.*, **140**, A1133 (1965)

[96] B. G. Johnson et al., *Chem. Phys. Lett.*, **221**, 100 (1994); M. Biagini, *Phys. Rev. B*, **49** 2156 (1994)

[97] D. M. Ceperley, *Phys. Rev. B*, **18**, 3126 (1978)

[98] D. M. Ceperley and B. J. Alder, *Phys. Rev. Lett.*, **45**, 566 (1980)

[99] W.E. Pickett, *Rev. Mod. Phys.*, **61**, 433 (1989)

[100] K.T.Terakura et al., *Phys. Rev. B*, **30**, 4734 (1984)

[101] D.J. Singh and W.E. Pickett, *Phys. Rev. B*, **44**, 7715 (1991)

[102] U. von Bart and L. Hedin, *J. Phys. C*, **5**, 1629 (1972)

[103] J.P. Perdew and A. Zunger, *Phys. Rev. B*, **23**, 5048 (1981)

[104] D.C. Langreth and M.J. Mehl, *Phys. Rev. B*, **28**, 1809 (1983)

[105] J.P. Perdew and Y. Wang, *Phys. Rev. B*, **33**, 8800 (1986)

[106] J.P Perdew, *Phys. Rev. B*, **33**, 8822 (1986)

[107] A. D. Becke, *Phys. Rev. A*, **38**, 3098 (1988)

[108] P.G. Bagno et al., *Phys. Rev. B*, **40**, 1997 (1989)

[109] H. Sawada et al., *Phys. Rev. B*, **53**, 12742 (1996)

[110] M. Nicastro, M. Kuzmin and C.H. Patterson, *Comp. Mater. Sci.*, **17**, 445 (2000)

[111] M. Nicastro and C.H. Patterson, *Phys. Rev. B*, **65**, 205111 (2002)

[112] V.R. Saunders, R. Dovesi, C. Roetti, M. Causà, N.M. Harrison, R. Orlando, C.M. Zicovich-Wilson **CRYSTAL 98 User's Manual**, Uninersity of Torino, Torino, 1988

[113] C. Roetti, *The CRYSTAL code* in "Quantum-Mechanical Ab-initio Calculation of the Properties of Crystalline Materials" C. Pisani ed., *Lecture Notes in Chemistry*, vol. **67**, Springer-Verlag (1996)

[114] H. J. Monkhorst and J. D. Pack, *Phys. Rev. B*, **13**, 5188 (1976)

[115] R. L. Martin, P. J. Hay, *J. Chem. Phys.* **98**, 8680 (1993)

[116] R. L. Martin, F. Illas, *Phys. Rev. Lett.* **79**, 1539 (1997)

[117] P. Butera and M. Comi, *Phys. Rev. B* **65**, 144431 (2002)

[118] I. de P. R. Moreira, F. Illas, *Phys. Rev. B* **55**, 4129 (1997)

[119] R. Pauncz, *Spin Eigenfunctions: Construction and use*, Plenum Press, New York (1982)

[120] L. Brillouin, *J. Phys. Radium*, **3**, 373 1932; L. Brillouin, *Les champs 'self-consistents' de Hartree et de Fock*, Hermann and Cie, Paris (1934)

[121] R. J. Buenker, *Studies in Physical and Theoretical chemistry*, **21**, 17 (1982)

[122] GAMESS-UK is a package of ab initio programs written by M.F. Guest, J.H. van Lenthe, J. Kendrick, K. Schoeffel, P. Sherwood, and R.J. Harrison, with contributions from R.D. Amos, R.J. Buenker, M. Dupuis, N.C. Handy, I.H. Hillier, P.J. Knowles, V. Bonacic-Koutecky, W. von Niessen, A.P. Rendell, V.R. Saunders, and A. Stone. The package is derived from the original GAMESS code due to M. Dupuis, D. Spangler and J. Wendoloski, NRCC Software Catalog, Vol. 1, Program No. QG01 (GAMESS), 1980; http://www.dl.ac.uk/CCP/CCP1/gamess.html

[123] S. Foster, S. F. Boys, *Rev. Mod. Phys.* **32**, 296 (1960)

[124] R. J. Buenker, *Studies in Physical and Theoretical Chemistry*, **21**, 17 (1982); R. J. Buenker and R. A. Phillips, *J. Mol. Struc. (Theochem)*, **123**, 291 (1985); S. Krebs and R. J. Buenker, *J. Chem. Phys.*, **103**, 5613 (1995)

[125] B. Roos, *Chem. Phys. Lett.*, **15**, 153 (1972)

[126] V.R. Saunders and J. H. van Lenthe, *Mol. Phys.*, **48**, 923 (1983)

[127] T. Yamanouchi, *Proc. Phys. Math. Soc. Jpn.*, **18**, 623 (1936); M. Kotani, A. Amemiya, E. Ishiguro and T. Kimura, *Tables of Molecular Integrals*, 2nd edition, Maruzen, Tokio (1963)

[128] P. A. M. Dirac, *Proc. Cambridge Phil. Soc.*, **26**, 376 (1930)

[129] S. H. Vosko, L. Wilk and M. Nusair, "Accurate spin-dependent electron liquid correlation energies for local spin density calculations: a critical analysis" *Can. J. Phys.*, **58**, 1200 (1980)

[130] R. D. Shannon and C. T Prewitt, *Acta crystallog. A*, **32**, 785 (1976)

[131] P. J. Hay and W. R. Wadt, *J. Chem. Phys.* **82**, 270 (1989)

[132] M. Catti et al., *J. Phys. Cond. Matt.*, **3**, 4151 (1991)

[133] G. Gilat and L. J. Raubenheimer, *Phys. Rev.*, **144**, 390 (1966); G. Gilat, *J. Comp. Phys.*, **10**, 432 (1972)

[134] C. Patterson and G. Zheng (in preparation)

[135] T.F.A Müller and T.M. Rice, *Phys. Rev. B*, **58**, 3425 (1998)

[136] N. P. Konstantinidis and C. H. Patterson (in preparation)